

**TRIBOLOGICAL AND STRUCTURAL PROPERTIES OF TITANIUM
NITRIDE AND TITANIUM ALUMINUM NITRIDE COATINGS
DEPOSITED WITH MODULATED PULSED POWER
MAGNETRON SPUTTERING**

by
Logan Ward

A thesis submitted to the Faculty and Board of Trustees of the Colorado School of Mines in partial fulfillment of the requirements for the degree of Master of Science (Metallurgical & Materials Engineering).

Golden, Colorado

Date _____

Signed: _____

Logan Ward
Masters Student

Signed: _____

Dr. Michael Kaufman
Thesis Advisor

\

Golden, Colorado

Date _____

Signed: _____

Dr. Van Tyne
Professor and Acting Head
Department of Metallurgy & Materials Engineering

ABSTRACT

The demand for economical high-performance materials has brought attention to the development of advanced coatings. Recent advances in high power magnetron sputtering (HPPMS) have shown to improve tribological properties of coatings. These coatings offer increased wear and oxidation resistance, which may facilitate the use of more economical materials in harsh applications.

This study demonstrates the use of novel forms of HPPMS, namely modulated pulsed-power magnetron sputtering (MPPMS) and deep oscillation magnetron sputtering (DOMS), for depositing TiN and $Ti_{1-x}Al_xN$ tribological coatings on commonly used alloys, such as Ti-6Al-4V and Inconel 718. Both technologies have been shown to offer unique plasma characteristics in the physical vapor deposition (PVD) process. High power pulses lead to a high degree of ionization compared to traditional direct-current magnetron sputtering (DCMS) and pulsed magnetron sputtering (PMS). Such a high degree of ionization was previously only achievable by cathodic arc deposition (CAD); however, CAD can lead to increased macroparticles that are unfavorable in high friction and corrosive environments. MPPMS, DOMS, and other HPPMS techniques offer unique plasma characteristics and have been shown to produce coatings with refined grain structure, improved density, hardness, adhesion, and wear resistance.

Using DOMS and MPPMS, TiN and $Ti_{1-x}Al_xN$ coatings were deposited using PMS to compare microstructures and tribological performance. For $Ti_{1-x}Al_xN$, two sputtering target compositions, 50Ti-50Al and 30Ti-70Al, were used to evaluate the effects of MPPMS on the coating's composition and tribological properties. Scanning electron microscopy (SEM), transmission electron microscopy (TEM), and X-ray diffraction (XRD) were used to characterize microstructure and crystallographic texture. Several tribological properties were evaluated including: wear rate, coefficient of friction, adhesion, and nanohardness. Results show that substrate material can have a significant effect on adhesion and the mechanical response between the coating and substrate. Depending on deposition parameters and the selected material MPPMS and DOMS are promising alternatives to DCMS, PMS, and CAD.

ACKNOWLEDGEMENTS

All the work embodied by this thesis was performed through the Advanced Coatings and Surface Engineering Laboratory (ACSEL) and the Center for Advanced Non-Ferrous Alloys (CANFSA) in the Metallurgical and Materials Engineering (MME) Department at Colorado School of Mines (CSM). Thanks to all the people who helped me get to where I am today and supported me in times of need and times of celebration.

I'd like to express my deep appreciation for the invitation offered by Dr. Ivar Reimanis to come to CSM and for his encouragement to apply for graduate school at CSM. During the time I worked in the Colorado Center for Advanced Ceramics (CCAC) I gained valuable knowledge prior to working in ACSEL. I am eternally grateful the generosity, acceptance, and helpful guidance offered by Dr. Reimanis and others in CACC throughout my first year at CSM.

During the first portion of my thesis, I heavily depended on the abundant knowledge and skills provided by Dr. Jianliang Lin and the colleagues of ACSEL. Without their guidance and advice I would not have gained the understanding and knowledge of coatings and materials that I now possess.

My sincere gratitude goes to my advisor, Dr. Michael Kaufman, who never failed to provide questions that carried inspiration and motivation to strive for the fundamental understanding of materials. As a professor, his patience and persistence to provide students with a sound understanding of materials science is invaluable. I'd also like to take this opportunity to thank the talented MME faculty who contributed to the abundance of knowledge I gained through classes while at CSM.

Thank you CANFSA, for providing funding in addition to the helpful feedback and advice brought by Doug Konitzer (GE Aviation) and Paul Rudnik (Plansee) who helped mentor me during the project. I'd also like to thank GE and Plansee for providing substrate materials and sputtering targets.

Finally, I want to say thank you to my loving family and wife, who have shown nothing but patience and support beyond what I could ask. And thanks to all the friends I've gained during my time at CSM for all the long scientific debates, social outings, rounds of golf, trips to the mountains, and all other precious memories I will forever treasure.

LIST OF FIGURES

Figure 2.1	Gas discharge modes for sputtering PVD methods organized into three key regions. Reprinted from [1].	4
Figure 2.2	Diagram of a typical magnetron sputtering apparatus showing Ar^+ ions colliding with the metal target and ejecting metal ions. Magnetic fields created by magnets modify electron and ion trajectories accelerating the sputtering process. Reprinted from [2].	5
Figure 2.3	Simulated curves predicting compound formation at the substrate (top) and target (middle). Simulation of flow curve for reactive O_2 gas overlapped with actual collected data. Reprinted from [1].	6
Figure 2.4	Diagram showing sheathes that form between the target cathode, anode chamber wall, and a floating metal substrate immersed in plasma (adapted from [1]).	9
Figure 2.5	Diagram showing typical cathode voltage profiles for DCMS and PMS deposition methods.	10
Figure 2.6	Ion mass distributions for plasmas generated using (a) DCMS and (b) MPPMS with a Cr target at several average target powers. Reprinted from [12].	11
Figure 2.7	Ion energy distributions for Ar^+ within plasmas produced with DCMS, PMS, and MPPMS. Reprinted from [14].	12
Figure 2.8	Diagram of a modeled 2-step MPPMS voltage profile that would be applied to a sputtering target.	13
Figure 2.9	Diagram of a typical HPPMS pulse adopted from [5] (top) and a 2-step MPPMS macropulse adopted from [14] (bottom).	14
Figure 2.10	Diagram of a typical DOMS voltage profile applied to a sputtering target.	15
Figure 2.11	Two diagrams showing a) Thornton's SZM [31] and b) the SMZ developed by Kelly and Arnell [32].	17
Figure 2.12	Schematic describing characteristics and mechanisms proposed for Zone I-II [33].	18
Figure 2.13	Schematic of (a) δ -(Ti,Al)N FCC rock-salt structure and (b) ω -(Ti,Al)N wurtzite structure.	20
Figure 2.14	Hardness values for deposited TiN and $\text{Ti}_{0.33}\text{Al}_{0.67}\text{N}$ coatings annealed at several temperatures. Adopted from [44].	21

Figure 2.15	Hardness values for CAE deposited $Ti_{1-x}Al_xN$ coatings with varying Al compositions [47].	21
Figure 3.1	Drawing of CFUBMS chamber with labeled components and front view of metal target (Ti, 50Ti-50Al, or 30Ti-70Al). The power source can be detached and reattached to any cathode/target. The sample can be rotated remotely toward the active target. A separate power supply was attached to sample holder and grounded outside the chamber for coatings deposited with substrate bias.	26
Figure 3.2	Diagram of the coating configuration used for this study.	27
Figure 3.3	Measured voltage and current waveforms for a TiN coating deposited with MPPMS.	27
Figure 3.4	Measured voltage and current waveforms for a TiN coating deposited with DOMS. (top) An entire macropulse cycle and (bottom) a high resolution graph of the individual micropulses.	28
Figure 3.5	Rockwell-C adhesion test ranking scale, known as the HF scale adopted from [66].	33
Figure 3.6	Fraction of peak intensity from incident x-rays with incident angles (ϕ), calculated using Equation (3.6). Included are calculated values of penetration depths. Glancing angles used in this study are 6° , 10° , and 14° .	34
Figure 3.7	$\sin^2\psi$ plot of TiN deposited with DOMS using -90 V bias onto a Ti-6Al-4V substrate. The residual stress using the linear fit is shown.	35
Figure 4.1	Backscattered SEM image of etched (left) Ti-6Al-4V and (right) IN718.	36
Figure 4.2	X-ray diffraction patterns for (left) Ti-6Al-4V and (right) IN718 using 2θ scan mode.	37
Figure 4.3	X-ray diffraction pattern for SS304 using 2θ scan mode.	38
Figure 4.3	Topographical 3-dimensional rendering of uncoated substrates collected with an optical profilometer. Also shown are the calculated R_a values for uncoated and coated substrates with TiN deposited with DOMS. An R_a measurement for coated SS304 was not available due to delamination of the coating.	39
Figure 4.4	SEM images of fractured cross sections of TiN coatings deposited on Ti-6Al-4V using DOMS with different substrate biases indicated by voltage.	40
Figure 4.5	TEM micrograph (left) of the overall coating structure of TiN deposited with floating bias onto IN718. A higher magnification image (right) from halfway through the thickness with a SADP in the upper right corner.	41

Figure 4.6	TEM micrograph (left) of the overall coating structure of TiN deposited with a -90 V substrate bias onto IN718. A high magnification image (right) from the top portion of the coating with a diffraction pattern in the upper right corner. Note this sample sustained a substantial amount of curtaining (V-shaped pores) during FIB sample preparation.	42
Figure 4.7	TEM micrographs of the coating interface between TiN, Ti, and IN718 deposited without bias (left) and with -90 V bias (right).	42
Figure 4.8	XRD patterns for TiN coatings with Ti adhesion layers deposited on IN718 (top) and Ti-6Al-4V (bottom). Variation in peak intensities for labeled planes is shown with respect to substrate bias.....	43
Figure 4.9	XRD grain size measurements of TiN coatings deposited with (top) DOMS and PMS using several negative substrate bias voltages and (bottom) DOMS-deposited coatings using varyious working pressures and a constant -60 V bias.	44
Figure 4.10	XRD patterns for DOMS-deposited TiN coatings with Ti adhesion layers onto IN718 (top) and Ti-6Al-4V (bottom). Variation in peak intensities for crystal planes is shown with respect to working pressure.	45
Figure 4.11	SEM images of fractured cross sections of TiN deposited at different substrate biases onto Ti-6Al-4V using PMS.....	46
Figure 4.12	Fractured cross sections of TiN coatings deposited on Ti-6Al-4V using DOMS (left) and PMS (right) with similar deposition conditions (-60 V bias, 7 mTorr, 2.5 hrs).	47
Figure 4.13	XRD patterns for TiN coatings deposited on IN718 (top) and Ti-6Al-4V (bottom) using PMS with -90 V applied substrate bias and without bias. Variations in peak intensities for labeled planes are shown with respect to working pressure.....	47
Figure 4.14	Effect of apply negative substrate bias on the residual stress in DOMS-deposited TiN films. Values were calculated from the linear fits of $\sin^2\psi$ graphs produced using measured peak shifts attained from GAXRD at several glancing angles (6° , 10° , and 14°).....	48
Figure 4.15	Nanoindentation results showing hardness and effective modulus of TiN coatings deposited on Ti-6Al-4V and IN718 (top) and calculated H/E^* and H^3/E^2 ratios (bottom) for several negative substrate biases. The dashed line indicates the desired H/E^* ratio for ultra-high performance coatings.	50

Figure 4.16	Nanohardness of TiN coatings deposited with DOMS on different substrates with various working pressures and using a -60 V substrate bias for all samples.	51
Figure 4.17	Scratch tests of PMS and DOMS-deposited TiN coatings on IN718 with several substrate biases. Examples of three critical loads are shown for the -90 V biased PMS coating	52
Figure 4.18	Scratch tests of DOMS-deposited TiN coatings showing the effects of substrate on adhesion.	53
Figure 4.19	SEM images of Rockwell-C adhesion tests of TiN coatings deposited with several deposition methods using floating bias. HF adhesion grade indicated in each image.	54
Figure 4.20	Rockwell-C indentation tests for TiN coatings deposited with DOMS and PMS with varying substrate biases (labeled on top) and substrates (labeled on leftside).	54
Figure 4.21	Calculated wear rate and COF for TiN coatings deposited on IN718 at several substrate biases with DOMS and PMS (left). Wear rate graphed as a function of H^3/E^2 from hardness results, showing a decreasing trend in wear rate with increasing resistance to plastic deformation.	55
Figure 4.22	SEM images of $Ti_{1-x}Al_xN$ coatings deposited with MPPMS and PMS using 50Ti-50Al (top) and 30Ti-70Al targets (bottom) onto Ti-6Al-4V. Fracture surfaces reveal the 50-100 nm Ti adhesion layer below the $Ti_{1-x}Al_xN$ coating.	56
Figure 4.23	BF TEM micrographs showing a cross-section of $Ti_{0.45}Al_{0.55}N$ deposited with MPPMS onto IN718 using floating bias (left). An SADP for the coating is also shown with labeled diffraction rings in regard to the cubic phase. On the right is a high magnification image from the middle portion of the coating.....	57
Figure 4.24	BF TEM micrographs showing a cross-section of $Ti_{0.45}Al_{0.55}N$ deposited with MPPMS onto IN718 using floating bias (left). An SADP for the coating is also shown with labeled diffraction rings for the cubic phase. On the right is a high magnification image from the top of the coating.	58
Figure 4.25	BF TEM image of Ti adhesion layer at the coating-substrate interface for MPPMS-deposited coatings using targets with compositions (a) 50Ti-50Al and (b) 30Ti-70Al.	58
Figure 4.26	XRD patterns for $Ti_{1-x}Al_xN$ coatings deposited with MPPMS and PMS on SS304 using a 50Ti-50Al target (left) and a 30Ti-70Al target (right). Also included is the	

	spectrum gathered for a pure Ti coating deposited with PMS for identifying the adhesion layer.	59
Figure 4.27	Calculated GS from XRD patterns of MPPMS and PMS-deposited $Ti_{1-x}Al_xN$ coatings.	60
Figure 4.28	Compositional measurements using EDS for $Ti_{1-x}Al_xN$ coatings deposited with MPPMS and PMS using 50Ti-50Al and 30Ti-70Al targets. Nitrogen has been excluded due to limitations of EDS for accurately measuring light elements. A dashed line represents equal target/coating Al ratios.	60
Figure 4.29	Hardness and thickness of $Ti_{1-x}Al_xN$ coatings deposited with MPPMS and PMS on SS304 using the 50Ti-50Al target with several different nitrogen flow rates. Coatings were deposited for 30 minutes.	61
Figure 4.30	Hardness and modulus of $Ti_{1-x}Al_xN$ coatings deposited with MPPMS and PMS on Ti-6Al-4V using 50Ti-50Al and 30Ti-70Al targets.	62
Figure 4.31	Hardness and effective modulus ratios of $Ti_{1-x}Al_xN$ coatings deposited with MPPMS and PMS onto Ti-6Al-4V using 50Ti-50Al and 30Ti-70Al targets.....	62
Figure 4.32	Scratch tests of MPPMS and PMS-deposited $Ti_{1-x}Al_xN$ coatings using two target compositions with floating bias.	64
Figure 4.33	Scratch tests comparing substrate effects on MPPMS-deposited coatings using a 50Ti-50Al target with floating bias.....	65
Figure 4.34	SEM images of Rockwell C indents performed on $Ti_{1-x}Al_xN$ coatings deposited on IN718. The deposition technique indicated on top and approximate coating composition indicated on the left. The HF grade is indicated in the corner of each image.....	65
Figure 4.35	Wear rates and COF's for $Ti_{1-x}Al_xN$ coatings deposited with MPPMS and PMS using different target compositions.....	66
Figure 5.1	Diagram showing (100), (110), and (111) single atomic layers of TiN oriented parallel to the substrate surface with low index directions that lie within each plane labeled and indicated by arrows.	68

Figure 5.2 Al/(Al+Ti) ratios derived from electron probe micro-analysis (EPMA) measurements for $Ti_{1-x}Al_xN$ coatings deposited with several target compositions using MPPMS. Adapted from [81]..... 72

LIST OF TABLES

Table 2.1	Electron-atom ionization reactions and their respective ionization energies [1].....	8
Table 2.2	ASM standard composition for Ti 6Al-4V [53] with EDS measurements.....	23
Table 2.3	ASM standard composition for IN718 [55] and measured composition using EDS.....	23
Table 3.1	Pulse parameters used for depositing TiN coatings.....	26
Table 3.2	Pulse parameters used for depositing TiAlN coatings.....	26
Table 3.3	Experimental matrix representing TiN coatings with different substrate biases and working pressures. DOMS coatings are indicated by X, PMS coatings are indicated by X*.....	29
Table 4.1	Thermal residual stresses calculated using the CTE* for the substrates and TiN.....	49
Table 4.2	Critical loads for scratch tested TiN coatings deposited with DOMS and PMS. Tests were conducted using a IN718 substrate for those deposited with different substrate biases.....	52
Table 4.3	Critical loads for scratch tested $Ti_{1-x}Al_xN$ coatings deposited with MPPMS and PMS using different target compositions and floating bias.....	64
Table 5.1	Simulated elastic moduli for TiN thin films (GPa) [72].....	69
Table 5.2	Calculated sputter yields using TRIM with 500 eV incident ions [82].....	72

TABLE OF CONTENTS

ABSTRACT.....	iii
ACKNOWLEDGEMENTS.....	iv
LIST OF FIGURES	v
LIST OF TABLES.....	xi
TABLE OF CONTENTS.....	xii
CHAPTER 1: INTRODUCTION	1
1.1 Motivation.....	1
1.2 Objectives and Approach.....	1
CHAPTER 2: BACKGROUND & LITERATURE REVIEW	3
2.1 Physical Vapor Deposition (PVD).....	3
2.2 Magnetron Sputtering	4
2.2.1 Plasma Fundamentals.....	6
2.2.2 Magnetron Sputtering Methods	9
2.2.3 Direct Current Magnetron Sputtering (DCMS) and Pulsed Magnetron Sputtering (PMS)	10
2.2.4 High Power Pulsed Magnetron Sputtering (HPPMS) and Modulated Pulsed Power	
Magnetron Sputtering (MPPMS).....	10
2.2.5 Deep Oscillation Magnetron Sputtering (DOMS)	14
2.3 Growth and Microstructure of Magnetron Sputtered Coatings.....	15
2.4 Structure and Properties of TiN Coatings	18
2.5 Structure and Properties of Ti _{1-x} Al _x N Coatings	19
2.6 Substrate Effects	22
2.6.1 Ti-6Al-4V	22
2.6.2 Inconel 718.....	22
2.7 Surface Roughness.....	24
CHAPTER 3: EXPERIMENTAL PROCEDURES	25
3.1 Substrate Preparation	25
3.2 Deposition Process.....	25
3.3 Characterization of Microstructure and Composition.....	29
3.3.1 Scanning Electron Microscopy (SEM)	29
3.3.2 Transmission Electron Microscopy (TEM)	30
3.3.3 X-Ray Diffraction (XRD)	30
3.4 Measurement of Coating Properties.....	31

3.4.1	Nanoindentation	31
3.4.2	Wear and Adhesion	32
3.4.3	Residual Stress	33
CHAPTER 4: RESULTS		36
4.1	Substrate Characterization	36
4.1.1	Microstructure	36
4.1.2	X-ray Diffraction	37
4.1.3	Surface Roughness	38
4.2	TiN	39
4.2.1	Microstructure and Crystallographic Texture	39
4.2.2	Residual Stress	48
4.2.3	Hardness and Elastic Modulus	49
4.2.4	Adhesion and Wear	51
4.3	Ti _{1-x} Al _x N	55
4.3.1	Microstructure and Crystallographic Texture	55
4.3.2	Hardness and Composition	60
4.3.3	Wear and Adhesion	63
CHAPTER 5: DISCUSSION		67
5.1	TiN	67
5.2	Ti _{1-x} Al _x N	71
CHAPTER 6: CONCLUSIONS		75
6.1	TiN coatings	75
6.2	Ti _{1-x} Al _x N	76
REFERENCES		77

CHAPTER 1: INTRODUCTION

1.1 Motivation

The aerospace industry has been at the forefront of producing high-performance, light-weight materials. Increasing the longevity of these materials is important for not only reducing the cost of replacement parts, but also improving safety and cutting down on material waste. The harsh applications frequently require high wear, oxidation, and corrosion resistance in order to improve longevity. Coatings can enhance many of these desired properties without having to modify the underlying alloy composition or structure. Although coatings have already been incorporated into many applications, there is demand for improvement of tribological properties and more efficient failure detection.

New high-power magnetron sputtering (HPPMS) techniques, such as modulated pulsed-power magnetron sputtering (MPPMS) and deep oscillation magnetron sputtering (DOMS) have been shown to offer improved coating densities and coating properties. This study investigates the advantages of using MPPMS and DOMS for producing TiN and TiAlN coatings used to extend the use of more economical alloys in harsh environments.

1.2 Objectives and Approach

This study is focused on determining whether novel magnetron sputtering techniques may offer improved properties for tribological coatings deposited on advanced non-ferrous alloys. The novel deposition techniques studied are MPPMS and DOMS, both are modified forms of HPPMS (a.k.a. high-power impulse magnetron sputtering, HiPIMS). These technologies have the potential to produce coatings with increased densities, improved properties as well as increased adhesion, and ability to grow thicker coatings all of which help provide better performance in harsh applications.

The approach taken in this study includes the production, optimization, and characterization of coatings using MPPMS and DOMS. The immediate goal is to correlate plasma characteristics of several deposition methods and deposition parameters with coating properties and growth behavior. Additionally, this study investigates how substrate material may influence adhesion, growth, and properties of such coatings. Several tribological properties that will be tested include: hardness, modulus, wear rate, coefficient of friction (COF), and adhesion.

To quantify the success of MPPMS and DOMS, structure and tribological properties will be compared with coatings deposited with more traditional techniques, such as direct current magnetron sputtering (DCMS), pulsed magnetron sputtering (PMS), and cathodic arc evaporation (CAE, a.k.a.

CAD). The coating systems of interest are TiN and TiAlN, which offer excellent hardness, wear resistance, and corrosion resistance. Both coatings have had extensive research making them more easily comparable to other deposition methods. The particular applications of interest are related to the aerospace industry where Ti-6Al-4V and Inconel 718 (IN718) alloys are often used as bulk materials.

The following chapters will provide background on magnetron sputtering and properties of TiN and $Ti_{1-x}Al_xN$ coatings, along with a presentation of the results gained through this study and discussion of their significance. Mechanisms of magnetron sputtering and characteristics for several deposition techniques will be included. Details on deposition conditions and experimental procedures for preparing and testing samples have been provided.

CHAPTER 2: BACKGROUND & LITERATURE REVIEW

The following chapter provides background on the basic principles of magnetron sputtering and several deposition methods. The structures and properties of TiN and $Ti_{1-x}Al_xN$ coatings deposited through these methods are reviewed. Property values from literature are discussed and will be compared to the results in this study later in the thesis.

2.1 Physical Vapor Deposition (PVD)

Depositing coatings through physical vapor deposition (PVD) involves evaporating or sputtering solid or liquid material onto a substrate. Sufficient kinetic or thermal energy must be supplied to atoms for them to be ejected from the target material. These atoms are then transported in a controlled low pressure atmosphere containing non-reactive and/or reactive gases to form a desired coating configuration. Unlike chemical vapor deposition (CVD), PVD allows for coatings to be deposited at relatively low temperatures, which often produces metastable phase materials that provide unique and desirable properties.

Two of the most popular PVD methods used in industry are CAE and magnetron sputtering. CAE utilizes arcs produced between a high electric field anode arm and a planar cathode target. The arcs create concentrated intense plasmas with a high degree of ionization. CAE is capable of high deposition rates, but suffers the incorporation of macroparticles, which are neutrally charged particles ejected from the target onto the substrate and have roughly the same composition as the target material. These defects can reduce wear properties and can be detrimental to corrosion resistance through galvanic coupling or creation of pinholes. Unlike CAE which works in the arc discharge region, magnetron sputtering uses high voltages and relatively low currents to achieve glow discharge. The highest ionization by magnetron sputtering is often achieved in the upper limits of the abnormal glow discharge region. The described gas discharge regions and other regions, including arc discharge for CAE, can be seen in Figure 2.1. Magnetron sputtered coatings tend to have denser structures with less macroparticles; however, deposition rates are typically lower than that of CAE.

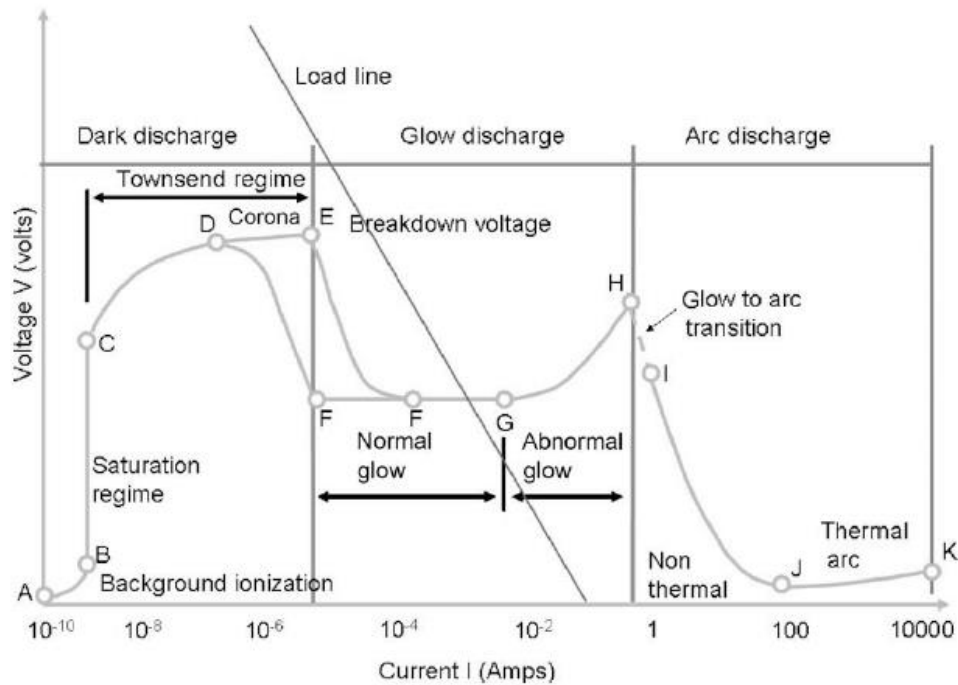


Figure 2.1 Gas discharge modes for sputtering PVD methods organized into three key regions. Reprinted from [1].

2.2 Magnetron Sputtering

Magnetron sputtering is a type of PVD process that utilizes gas and metal ions in a plasma discharge state to form coatings on a chosen substrate. A simplified magnetron configuration, similar to the one used in this study, can be seen in Figure 2.2. In conventional DCMS a negative voltage is applied to the cathode/target. Positive gas ions generated in the plasma are attracted to the target by the high electric field. These ions sputter atoms and molecules in the process. A magnetic field generated by either permanent magnets, electromagnets, or both help confine electrons close to the target surface. This keeps the plasma dense near the target surface, which increases the likelihood for gas ionization through high energy electron collisions. In effect, more ions are made available for the sputtering process, making it more efficient. The ions generated are hardly affected by the magnetic field due to their relatively high mass. The electric field has a major influence on the ion density, degree of ionization, and ion energies, all of which have a strong effect on coating growth and properties.

There are two main types of gas sputtering modes, reactive and non-reactive. In non-reactive sputtering, ionized non-reactive gas atoms, such as Ar, are used to sputter target atoms. Some ejected metal atoms and/or molecules find the substrate surface creating a coating similar in composition to the target material. In reactive sputtering, reactive gases, such as N₂ or O₂, are injected with non-reactive

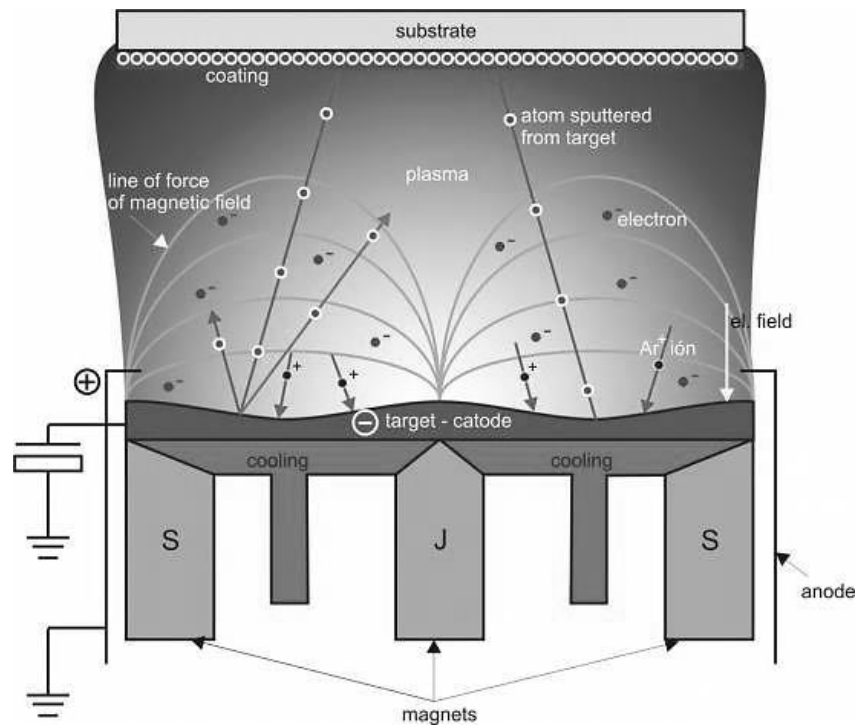


Figure 2.2 Diagram of a typical magnetron sputtering apparatus showing Ar^+ ions colliding with the metal target and ejecting metal ions. Magnetic fields created by magnets modify electron and ion trajectories accelerating the sputtering process. Reprinted from [2].

gases into the sputter chamber. Sputtered metal ions may combine with reactive ionized gas atoms to form molecules like TiN or TiO_2 . Reactive sputtering presents new obstacles to overcome including control over coating stoichiometry and target poisoning effects. The coating properties and deposition rates are quite sensitive to gas partial pressures. These can be controlled either by percent flow control or partial pressure control, the latter being more accurate as partial pressure can change with constant flow percentages depending on how stable the consumption of ions are at the anode, cathode, and substrate. If the flow rate for the reactive gas is too high, the ionized gas may react with the target and form a compound layer on the surface. As for the case of TiN and many other systems, the sputtering yield of TiN molecule is much lower than that of Ti , thus the deposition rate drastically decreases along with the consumption of the reactive gas. This creates a poisoning effect which requires sputtering off the poisoning layer on the target by lowering the reactive gas partial pressure. The result is a hysteresis curve in the flow percentage vs. partial pressure of reactive gas as shown in Figure 2.3.

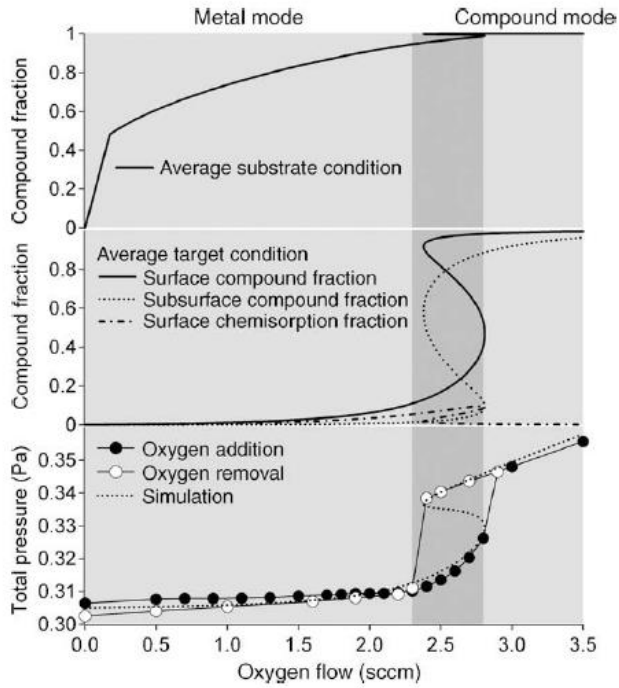
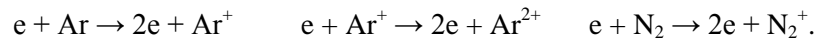


Figure 2.3 Simulated curves predicting compound formation at the substrate (top) and target (middle). Simulation of flow curve for reactive O₂ gas overlapped with actual collected data. Reprinted from [1].

2.2.1 Plasma Fundamentals

Plasmas can be described as partially ionized gases composed of negatively and positively charged free-flowing particles, which collectively make a neutral net charge. In the case of magnetron sputtering, the negatively charged particles are primarily electrons and the positively-charged particles are metal ions. Additionally, sputtered neutral atoms may also be contained within the plasma. The proportion of ionized atoms is what determines the degree of ionization, whereas the plasma density is determined by the number of free electrons per unit volume.

The sputtering and ionization process begins with negatively charging the cathode/target. Free electrons near the target surface are consequently accelerated away from the negatively charged target and toward the gases present within the chamber. The high energy electrons collide with the initially neutral gas atoms or molecules. Both elastic and inelastic collisions occur. In the case of inelastic collisions, some may cause a reaction that ejects an electron from a gas atom, e.g.



This occurrence is known as ionization, where an exchange of kinetic energy from the electron results in a gas ion and one additional free electron. Positively charged gas ions are attracted back toward the negatively charged target and collide with metal atoms on the target surface; the impacted metal atoms are provided with sufficient kinetic energy to be sputtered away from the target. Ionization of metal atoms can be caused by either energy transfer from the bombarding ion or accelerated electrons within the plasma. The multiplication of “free electrons” in ionization, as seen in the reactions above, is what maintains the glow discharge process while electrons and ions are consumed by recombination. During recombination, free electrons combine with ions, and due to the law of energy conservation, the atom must emit a photon. This is what gives the plasma its glowing color, which its patterns can be useful for monitoring partial pressures.

Sufficient energy and probability for collision by an incident electron is required for ionization to occur. Due to the relatively small mass of electrons (~ 0.00055 amu) compared to gas atoms (N ~ 14 amu; Ar ~ 40 amu), in addition to their negative charge, electrons are more quickly accelerated when an electric field is applied. The energy transferred from a moving electron to an atom/ion at rest, ΔE , is given by Equation (2.1). The terms E_{ei} and E_{ef} represent the electron energy before and after the collision, whereas m_e and m_a are the masses for the colliding electron and atom respectfully.

$$\Delta E = E_{ei} - E_{ef} = \frac{4m_e m_a E_{ei}}{(m_e + m_a)^2} \cos^2 \theta \quad (2.1)$$

Assuming head-on collisions, where $\theta=0$, and since $m_e \ll m_a$ Equation (2.1) can be simplified to Equation (2.2).

$$\Delta E = \frac{4m_e}{m_a} E_{ei} \quad (2.2)$$

This shows that the energy transferred is proportional to the ratio of the electron mass, m_e , and atom/ion mass, m_a . Since the mass of an electron is relatively low, substantial electron energy/temperature is required for ionization to occur. Now consider an electron within a magnetic field, E , which applies a force equal to $F=eE$, where e is the charge of the electron. The work done by the electric field can then be calculated by multiplying the force by the distance the electron travels, or the mean free path, giving $W_E=eE\lambda$. The mean free path can be approximated by $1/N\sigma$, where N is the number of particles and σ is the collision cross-section ($\sim 10^{-15}$ to 10^{-16} cm²) [1]. In order to maintain equilibrium in the plasma the energy lost in collisions must equal that of W_E , so by substituting W_E for ΔE in Equation (2.2) we find a new relationship for E_{ei} in Equation (2.3).

$$E_{ei} = \frac{m_a}{4m_e} \left(\frac{eE}{N\sigma} \right) \quad (2.3)$$

Now it can be seen that energy supplied by electrons for ionization is dependent on two key factors, E and N . The potentials applied to the target and/or the substrate are what influence E , whereas N is controlled by the working pressure. Low gas pressures, where electron/ion collisions are less frequent and λ is larger, along with high voltages, give way to higher energy particles and higher degrees of ionization. At low electron energies (<10 eV) collisions are primarily elastic, but at electron energies >10 eV inelastic mechanisms, like ionization, become more dominant and limit electrons from reaching higher energies. Typical average electron energies/temperatures within a low pressure discharge plasma between 2 to 8 eV [3], which is much higher when compared to gas atoms at room temperature ($300\text{ K} = 0.025\text{ eV}$). Some relevant ionization energies can be seen in Table 2.1 [1]. One important ionization energy is that of Ar^+ (15.76 eV), which explains why ionization is not observed until electron energies exceed 10 eV in Ar environments.

Table 2.1 Electron-atom ionization reactions and their respective ionization energies [1].

Ionization Reaction	Ionization Energy (eV)
$e^- + \text{Ar} \rightarrow \text{Ar}^+ + 2e^-$	15.76
$e^- + \text{Ar} \rightarrow \text{Ar}^{2+} + 3e^-$	27.53
$e^- + \text{N}_2 \rightarrow \text{N}_2^+ + 2e^-$	15.5
$e^- + \text{N}_2 \rightarrow \text{N}^+ + \text{N} + 2e^-$	24.4
$e^- + \text{Ti} \rightarrow \text{Ti}^+ + 2e^-$	6.83
$e^- + \text{Ti} \rightarrow \text{Ti}^{2+} + 3e^-$	13.58
$e^- + \text{Al} \rightarrow \text{Al}^+ + 2e^-$	5.99
$e^- + \text{Al} \rightarrow \text{Al}^{2+} + 3e^-$	18.83

As mentioned previously, electrons are accelerated away from the target more quickly than sputtered metal ions due to their small mass and negative charge. This can create an imbalance in the plasma potential. When an electronically insulated (floating) substrate is immersed in the plasma, electrons initially reach the substrate surface, effectively creating a negative charge with respect to the plasma potential (V_p). Positively charged ions are immediately attracted to the substrate, while electrons are repulsed at a rate that balances the charge flux from incoming ions. The result is the collection of ions around the substrate as a positive space charge known as a “sheath” [3]. A similar occurrence happens at the anode walls as seen in Figure 2.4 [1]. A schematic showing the change in plasma potential within a sputter chamber can be seen in Figure 2.4. The voltage to the substrate, i.e., the substrate potential (V_s),

can be subtracted from V_p to find the floating potential (V_f). Using a Maxwellian energy distribution, V_f can be approximated using Equation (2.4) [3], where k is Boltzmann's constant.

$$V_f = V_p - V_s = \frac{kT_e}{2e} \ln \left[\frac{m_a}{2.3 m_e} \right] \quad (2.4)$$

By using the mass of a neutral argon atom (40amu) and assuming that the electron temperature, T_e , ranges between 2 to 8 eV, V_f can be expected to be around -10 to -40 V. It is then reasonable to predict that incident ions/molecules may bombard the surface with energies up to $-qV_f$, where q is the charge of the ion or ionized molecule. The energy of incident ions has a significant impact on the growth, microstructure, and performance of sputtered coatings, which is why the value of V_f is important to keep in mind when analyzing coatings deposited with different substrate biases.

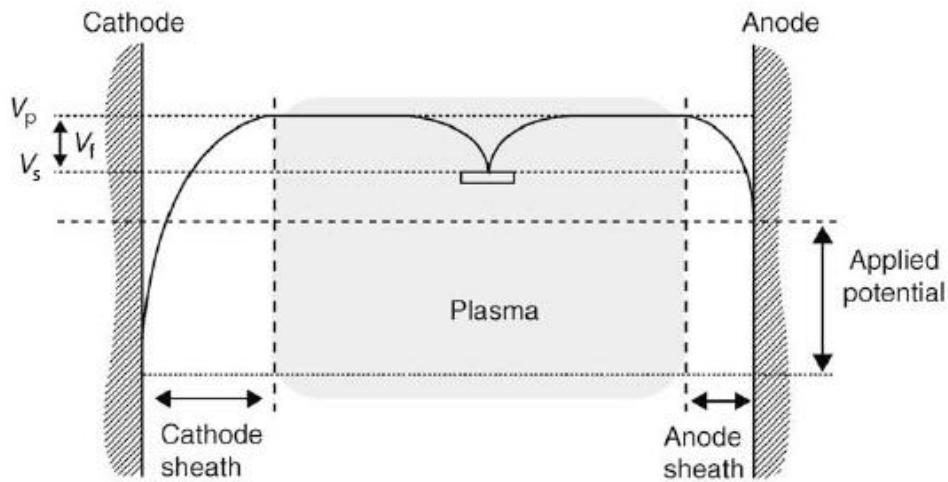


Figure 2.4 Diagram showing sheathes that form between the target cathode, anode chamber wall, and a floating metal substrate immersed in plasma (adapted from [1]).

2.2.2 Magnetron Sputtering Methods

Magnetron sputtered coatings consisting of nitrides and carbides (TiN, TiAlN, CrN, TiC, etc.) are commonly used as protective coatings. Recent developments in deposition methods have led to increased coating performance compared to traditionally used deposition methods, such as DCMS, PMS, and CAE. Deposition conditions such as power, pulse patterns, working pressure, and substrate bias can have a significant effect on coating structure and properties. Variables related to the power supply and how it is applied to the target vary from one technique to the next. The following subsections give a brief description of several sputtering techniques. Additional information will be provided on the theory behind HPPMS methods and the development of MPPMS and DOMS.

2.2.3 Direct Current Magnetron Sputtering (DCMS) and Pulsed Magnetron Sputtering (PMS)

The simplest form of magnetron sputtering is DCMS, which supplies continuous current and voltage to the target. Because of its simple nature, it is relatively predictable, but doesn't have a very high rate of ionization which is unfavorable for fast deposition rates and dense coatings. Additionally, DCMS has inherent problems with arcing, caused by charge build-up on dielectric coatings created by reactive sputtering. Such arcing is undesirable because it leads to uneven removal of target material leading to the creation of macroparticles and varying composition in the coating can lead to mechanical, corrosive, and/or electrical failures.

Pulsed magnetron sputtering was created to reduce arcing through the use of discharge pulses. Discharge pulses are short positive voltage pulses approximately 10% of the applied negative voltage pulse length and 10% of the magnitude. By varying the frequency and length of the on time and discharge time, stable plasmas with little to no arcing can be achieved. Typical pulse patterns for DCMS and PMS can be seen in Figure 2.5.

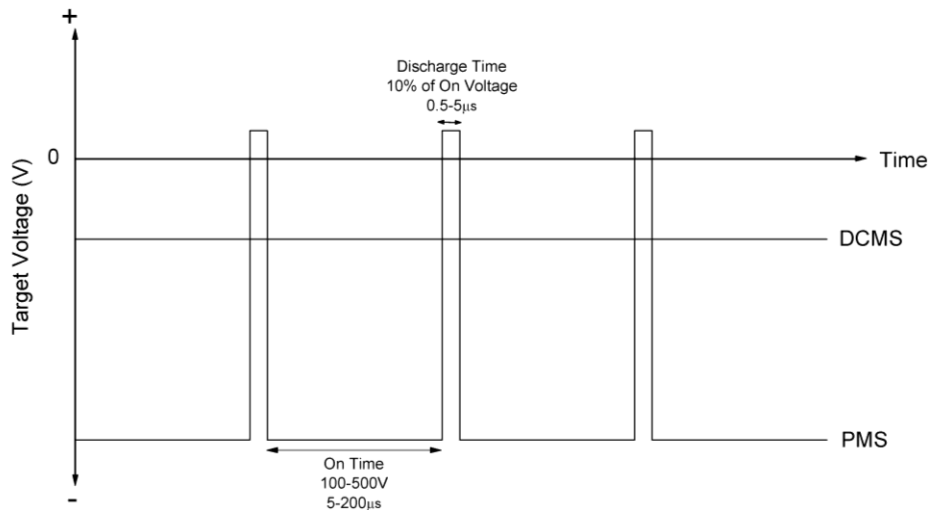


Figure 2.5 Diagram showing typical cathode voltage profiles for DCMS and PMS deposition methods.

2.2.4 High Power Pulsed Magnetron Sputtering (HPPMS) and Modulated Pulsed Power Magnetron Sputtering (MPPMS)

The theory behind MPPMS was originally derived through the deposition method called HPPMS, also known as High Power Impulse Magnetron Sputtering (HiPIMS). Developed in 1999 by Kouznetsov and co-workers, HPPMS utilizes relatively short (50-200 µs) pulses at very high voltages (1000-2000 V)

leading to peak power densities on the order of 0.3-3 kW/cm² [4]. Peak power densities achievable by DCMS and PMS are on the order of 0.01-0.1 kW/cm². The high target currents created by the high voltage pulses lead to relatively high electron densities ($\sim 10^{19}$ m⁻³) compared to those produced by DCMS (10^{14} - 10^{16} m⁻³) [5]. Dense concentrations of electrons near the target surface increase the chance for collisions with metallic atoms causing ionization [6, 7]. Consequently, ion densities and the ratio of ionized atoms to neutral atoms increase. In some cases, secondary ions or even higher orders, where more than one electron is ejected from an atom, can be produced as reported in some studies [6, 8–11]. A study done by Lin *et al.* compared the mass distributions within plasmas produced using MPPMS and DCMS [12] (see Figure 2.6). It was found that MPPMS produced a high number of ions, especially metallic ions, for the same average power used with DCMS. Additionally, MPPMS was able to produce more secondary ion species. This characteristic of HPPMS and other forms of HPPMS allows for denser coatings, enhanced part coverage, and the ability to have more control of ions with the magnetic and electric fields.

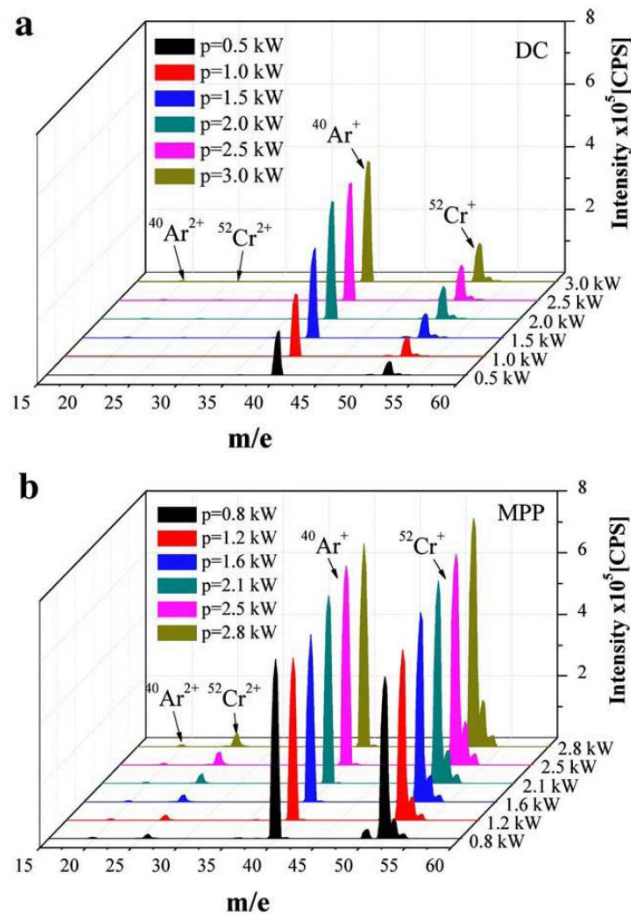


Figure 2.6 Ion mass distributions for plasmas generated using (a) DCMS and (b) MPPMS with a Cr target at several average target powers. Reprinted from [12].

While HPPMS and PMS may be able produce comparable degrees of ionization to MPPMS, it is often at the cost of producing high energy ions. When ion energies exceed 30 eV, excessive ion bombardment can lead to undesirable defects in the coating, which can also result in residual stresses [13]. In a study by Lin *et al.* [14] ion energies within plasmas produced by DCMS, PMS, and MPP were compared. Figure 2.7 shows that MPPMS produced the highest peak intensity while maintaining an energy tail below 25 eV. DCMS suffers from low overall intensity, while PMS produced a very long energy tail with ions up to 100 eV.

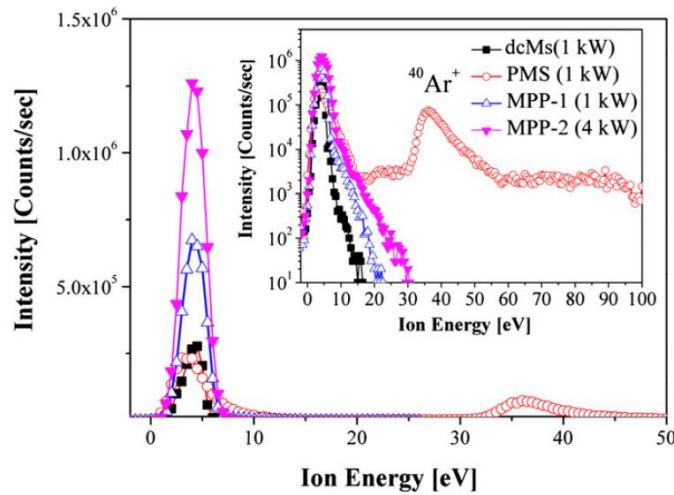


Figure 2.7 Ion energy distributions for Ar^+ within plasmas produced with DCMS, PMS, and MPPMS. Reprinted from [14].

The unique plasma properties of HPPMS have been shown to be advantageous for several coating applications. Many investigations have found that HPPMS can produce coatings with increased densities and enhanced mechanical, optical, and electrical properties for several systems [6, 15–18], including TiN [19–23] and $\text{Ti}_{1-x}\text{Al}_x\text{N}$ [24]. Though HPPMS has been shown to improve coating properties, it commonly suffers lower deposition rates compared to DCMS and PMS. A review of HPPMS research by Sarakinos found that the ratio of deposition rates of HPPMS to DCMS for coating systems deposited with the same average powers varied from 15% to 120%, although in most cases it was below 80% [5, 25]. The deposition rate for a given system can also vary depending on the target material, pulse parameters, gases used and how they are regulated. In Sarakinos' review, several authors were cited who theorized that the lower deposition rates are largely influenced by the high metallic ionization and re-direction of sputtered metal ions back toward the target [5]. Lower self-sputtering yield for M^+ ions vs. Ar^+ may compound this issue by further decreasing deposition rate. Factors that have been shown to increase ionization and

decrease deposition rate include: high target voltage, higher peak power/current, and long pulse lengths [5].

Limitations of HPPMS led to the development of MPPMS by Chistyakov *et. al.* [26]. For this method, the applied target voltage consists of 1000 μs single pulses that are divided into two main zones, a moderately high voltage ignition/weakly ionized zone and high voltage strongly ionized zone (see Figure 2.8). The weakly ionized stage is meant to produce a stable discharge before applying the high voltage for strong ionization to reduce the probability for arcing during high power. The effect of the two-stage process on the discharge current can be seen when comparing two recorded pulse curves for HPPMS and MPPMS. Figure 2.9 shows that the discharge current reaches a steady state quickly after the weakly ionized zone for MPPMS, whereas in HPPMS, the discharge current may never reach a steady state during the high power pulse. Anders has also shown that HPPMS can often suffer instabilities in current due to Ar^+ rarefaction and self-sputtering [10], both of which are unfavorable for deposition rate.

In addition to off times, helpful for reducing arcing, arc suppression (brief termination in the pulse when an arc is detected) is built into the power supply for both HPPMS and MPPMS. For a given macropulse, each zone is comprised of short 3-10 μs micropulses that vary slightly in voltage. Micropulses can be used in different configurations to help control discharge stability and arc suppression. Furthermore, gradual ramping can be implemented in the ignition stage and in the transition between weakly ionized and strongly ionized zones. These variables are what give flexibility and control over pulses to help create stable plasmas. The peak power density for MPPMS is slightly lower than HPPMS at 0.1-0.5 kW/cm^2 . However, the longer pulse lengths used in MPPMS allow for similarly high degrees of ionization compared with HPPMS.

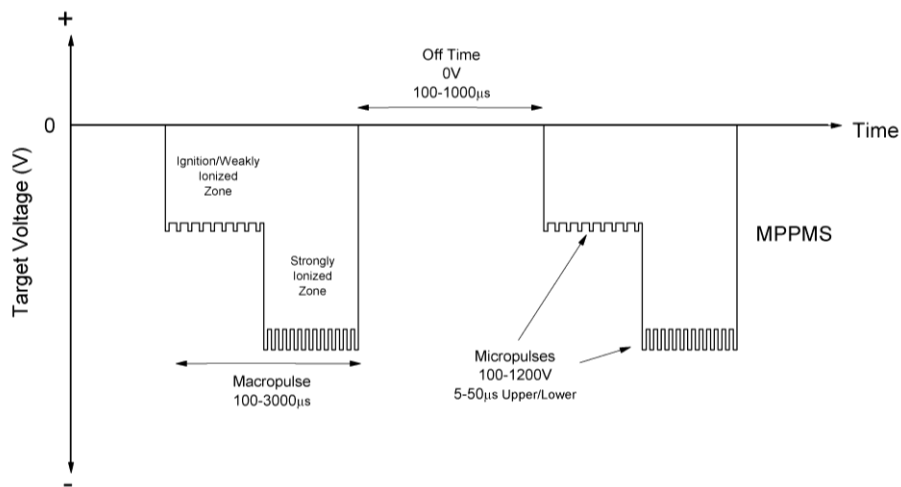


Figure 2.8 Diagram of a modeled 2-step MPPMS voltage profile that would be applied to a sputtering target.

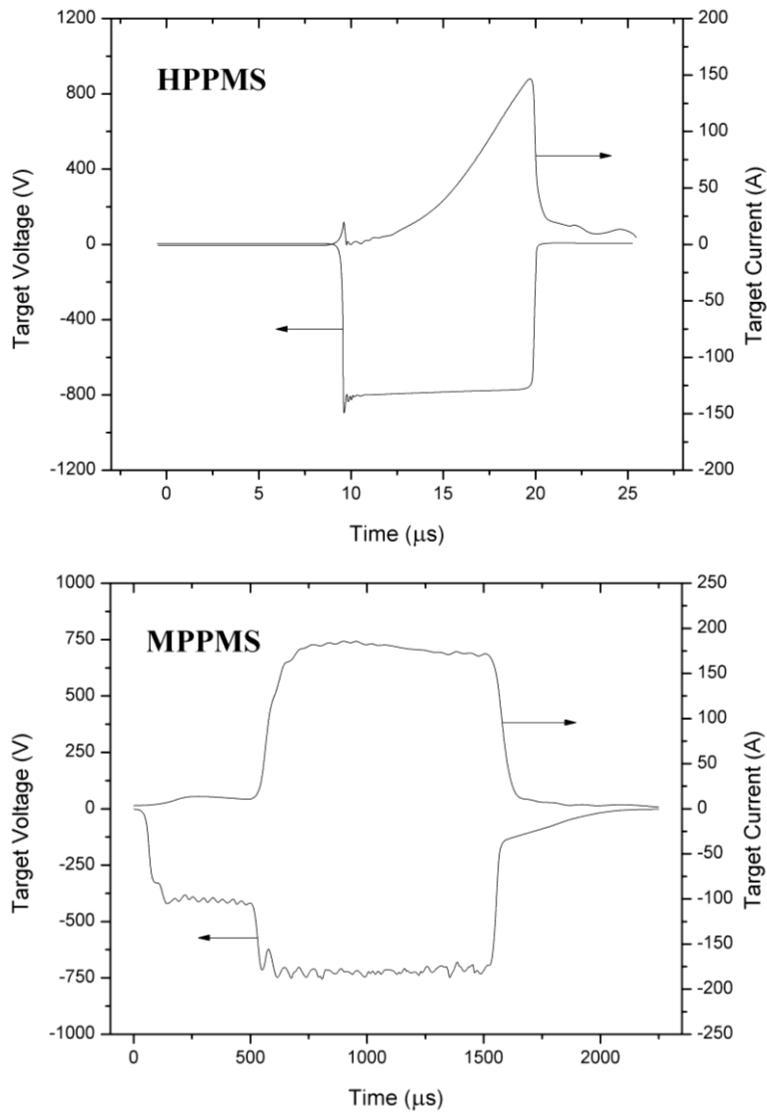


Figure 2.9 Diagram of a typical HPPMS pulse adopted from [5] (top) and a 2-step MPPMS macropulse adopted from [14] (bottom).

2.2.5 Deep Oscillation Magnetron Sputtering (DOMS)

The most recent form of high power sputtering is DOMS, which consists of micropulses modulated into macropulses, similar to MPPMS. A diagram showing a typical pulse pattern and pulse parameters can be seen in Figure 2.10. Very little literature can be found on DOMS deposited coatings, however, recent findings show promise for enhanced ionization, arc reduction, and increased coating density [13, 27]. Thus far, DOMS has proven to be particularly useful for depositing insulating coatings,

such as oxides, with higher ionization and reduced arcing compared to MPPMS or other traditional sputtering techniques.

Several forms of HPPMS have been shown to increase the coating densities and improve mechanical, optical, and electrical properties. The unique pulse profiles have a profound effect on the plasma characteristics which gives the coatings their enhanced properties. The degree of ionization is increased while maintaining the same average power used by DCMS and PMS. The new plasma dynamics have been shown to have different effects on ion energy distributions, HPPMS having high energy tails [11], whereas MPPMS has been shown to reduce high energy ions while maintaining higher ionization [14]. The result is increased ion adatom mobility through increased average ion energy and ion flux at the substrate, which is beneficial for depositing dense coatings with unique properties. Increased adatom mobility without the use of substrate heating is also useful for producing coatings on thermally sensitive materials, which are becoming ever more popular in industrial applications.

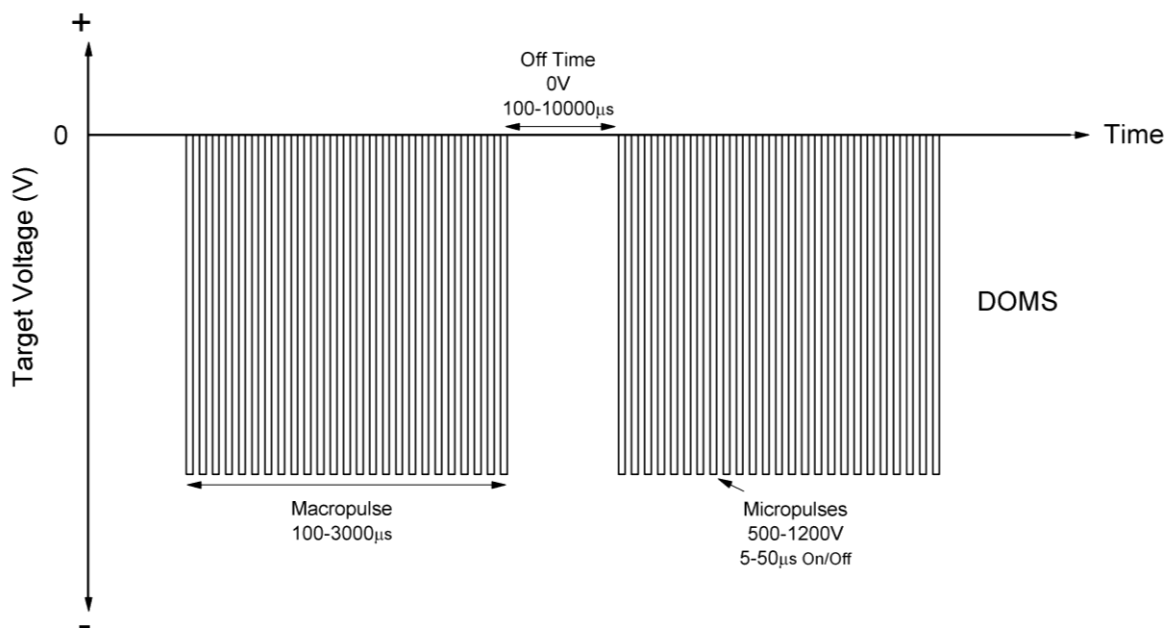


Figure 2.10 Diagram of a typical DOMS voltage profile applied to a sputtering target.

2.3 Growth and Microstructure of Magnetron Sputtered Coatings

The study of nucleation and growth on the atomic scale is becoming increasingly important for progression of coating technology. Further understanding of these fundamentals enables fine control over the structure, chemistry and, in turn, the physical and mechanical properties. Acquiring this ability is necessary for satisfying the rigid and demanding requirements set by new coating applications. Nucleation and growth of magnetron sputtered coatings are dependent on several variables controlled by

the material system and deposition process including: the coating material, substrate material, flux (J) and energy (E_p) of the incident particles on the substrate, substrate temperature (T_{sub}), and the cleanliness, crystallinity, and orientation of the substrate [1].

Choosing an appropriate coating material for a given application is important; equally important is the composition and structure of the coating. Composition and temperature are controlling factors determining what phase(s) develop during growth. Studies have shown that the incorporation of an adhesion layer or piezoelectric layer may help or hinder adhesion depending on deposition conditions and the coating/substrate materials [4, 28]. Substrate characteristics such as coefficient of thermal expansion (CTE), surface roughness, surface oxides, grain size, crystal structure, orientation to the target, and grain size have also been found to influence coating growth [29]. All these factors are carefully considered for all experiments described herein, though the primary interest in this study is concentrated on the influence of MPP and DOMS on the growth and properties of tribological coatings.

Although microstructural evolution of magnetron sputtered coatings has been extensively researched, the fundamental driving forces and mechanisms are still discussed. The mobility of adsorbed atoms, also known as adatoms, is a common attribute used to describe why certain growth mechanisms and microstructures occur. Several models and explanations have been developed to describe the general growth behavior of PVD coatings.

Movchan and Demchishin designed one of the first structural zone models (SZM), using empirical data, to correlate deposition parameters with observed microstructures [30]. It was later modified by Thornton to the SZM shown in Figure 2.11a [31]. Further efforts have been made to extend this model using additional empirical data and/or computer models to show the effects of ion energy and ion flux. The SZM in Figure 2.11b is one example developed by Kelly and Arnell [32]. Both models classify different coating microstructures into zones.

Each zone depicted in Figure 2.11a can be defined by grain features which form by different growth mechanisms. Adatom mobility and ion flux are what provide energy for certain mechanisms to occur. A schematic made by Mahieu in Figure 2.12 describes zones I-II in detail [33]. In Zone I, we find that, at low adatom mobilities/flux, there is less surface diffusion occurring. Adatoms tend to hit and stick where they land, thus forming narrow, porous, columnar structures. During growth, small voids can form within the grains due to the limited mobility of adatoms. Additionally, a shadowing effect from neighboring grains causes voids to accumulate near grain boundaries. In Zone T, enough energy is provided, either through ion bombardment or T_{sub} , to supply adatoms with sufficient mobility to diffuse on the surface. Surface diffusion allows for competitive grain growth, thus forming preferred orientations determined by kinetics or surface/strain energy reduction. Zone II and Zone III occur at even higher

mobilities/fluxes where recrystallization, driven by growth defects and residual strains, can lead to large columnar grains and in some cases equiaxed grains.

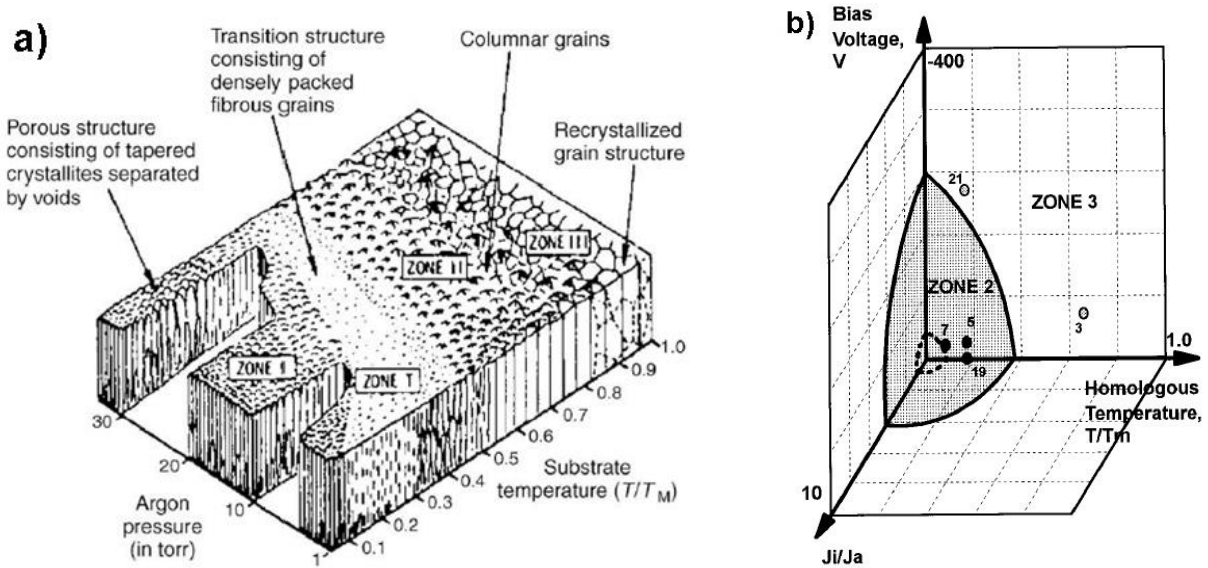


Figure 2.11 Two diagrams showing a) Thornton's SZM [31] and b) the SMZ developed by Kelly and Arnell [32].

Adatom mobility not only has an effect on structure, but also the crystallographic orientation of the coatings; such texture can cause anisotropic effects in mechanical behavior. For rock-salt crystal systems, (200) and (220) textured coatings tend to have high hardnesses, whereas (111) textured coatings provide greater toughness and wear resistance. Cheng and Tay studied the effects of temperature and substrate bias on the texture of TiN coatings using hollow cathode discharge ion plating [34] and found that (200) textures are preferred at high temperatures ($\approx 580^\circ\text{C}$) and low substrate biases. A (220) texture was more common at high substrate biases and lower temperatures ($\approx 40^\circ\text{C}$). Intermediate conditions usually resulted in a (111) texture. This behavior was explained in terms of minimizing the total overall energy. Two of the main contributors are surface energy (S) and strain energy (u). S increases with the number of dangling bonds on the surface of a single crystal plane, where u increases with increasing modulus in the direction of the plane normal. The resulting S and u relationships between planes are $S_{200} < S_{220} < S_{111}$ and $u_{111} < u_{220} < u_{200}$. Thus, when adatom mobility is sufficient for surface diffusion and strains produced by defects or thermal expansion mismatches are low, then S is dominant and (200) textures tend to form. Conversely, when there are lattice strains from growth defects, which are typically associated with high energy ions assisted by high substrate bias, (220) and (111) textures tend to form [35]. Zhao explains that ion channeling can also influence coating texture when substrate bias exceeds 100 V [36].

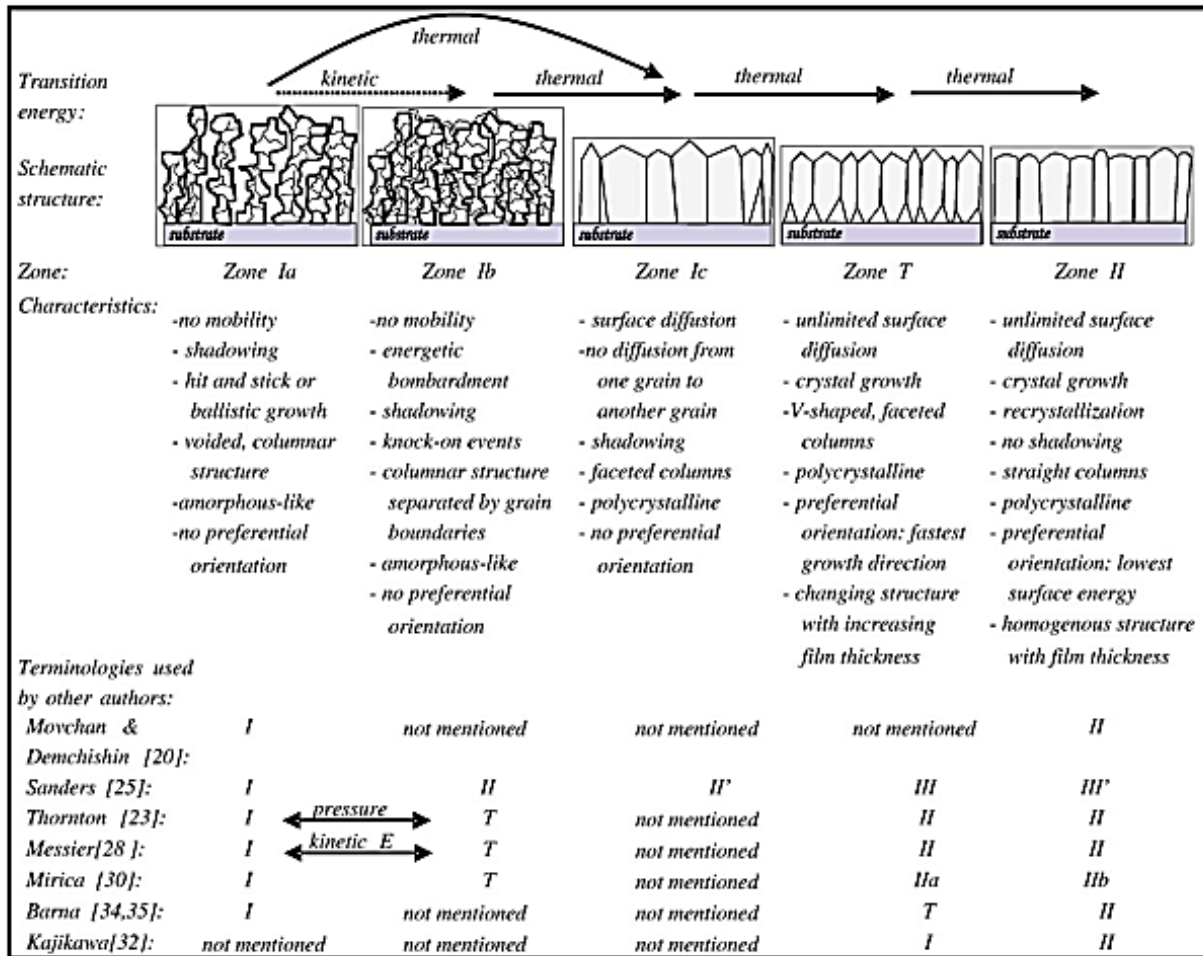


Figure 2.12 Schematic describing characteristics and mechanisms proposed for Zone I-II [33].

2.4 Structure and Properties of TiN Coatings

TiN is a highly studied system that has been well known and tested throughout the scientific coating community. Sputtered TiN coatings are attractive in applications requiring high hardness and wear resistance at relatively low temperatures (<500°C) where oxidation resistance is not as important. However, the strength and wear resistance of TiN coatings can vary greatly depending on the microstructure, density, crystal orientation, and adhesion.

For stoichiometric TiN coatings the equilibrium phase has the rock-salt FCC crystal structure with the Fm3m space group. This phase is known as δ -TiN. It has a room temperature lattice parameter of 4.240 Å and is gold-colored in appearance [37]. The rock-salt structure is stable for TiN_x, where

$x=0.6-1.1$. At $x<0.6$, the Ti-rich phase, ϵ -Ti₂N, may also be present. For ϵ -Ti₂N, the crystal structure is tetragonal, resembling an anti-rutile unit cell of space group P4₂/mnm. Both phases are known for possessing high hardness. While Ti₂N is favored for its superior corrosion resistance, TiN is more widely used due to its wear properties and compositional stability.

The tribological properties of TiN vary depending on the sputtering method and deposition parameters used. CAE is one of the most competitive techniques in industry, due to its high deposition rates and respectable performance. Typical hardness values reported for TiN using CAE range from 10 to 30 GPa [34, 38, 39]. Typical coefficients of friction (COF) for CAE range from 0.4 to 0.6 [38]. For PMS, typical hardness values are 18 to 39 GPa [40–42] while for dcMS, the hardness values are lower, ranging from 15 to 25 GPa [42]. Variance in hardness and modulus are largely attributed to deposition conditions, especially working pressure, substrate bias, and substrate temperature.

2.5 Structure and Properties of Ti_{1-x}Al_xN Coatings

Like TiN, Ti_{1-x}Al_xN is well studied and is still widely used by many industries; thus, it is ideal for comparing material properties gained by new deposition methods over traditional methods. Well known for its oxidation and corrosion resistance, TiAlN makes as an ideal coating for harsher applications where a part may be exposed to high temperatures (up to 800°C) and/or more corrosive and abrasive environments.

For Ti_{1-x}Al_xN, the composition can be varied for the desired applications where oxidation resistance or a certain phase is more favorable. Typical values of x used in industry vary between 0.5 and 0.7. The Al component is what gives Ti_{1-x}Al_xN a protective native oxide layer. Additionally, when the coating undergoes damage, Al atoms may diffuse toward the surface and re-passivate, thus creating a new protective layer. The mechanical properties may also be affected by the Al concentration, x . Different phases may form depending on the value of x and if the coating is exposed to higher temperatures. Assuming a proper %N is used to form a 50(Ti,Al):50(N) composition of the film, when $x\leq 0.6$, Ti_{1-x}Al_xN coatings have the tendency to form an FCC crystal structure like δ -TiN. For compositions where $x\geq 0.6$ the hexagonal ω -(Ti,Al)N, or wurtzite, phase is more prevalent [43]. This structure is similar to a zinc-blende hexagonal structure. Formation of complete δ -(Ti,Al)N is considered to be thermodynamically unstable; thus, phase separation may occur given sufficient thermal energy and Al content. This decomposition is said to occur by separation of Ti and Al into ω -AlN and δ -TiN or Ti-rich δ -Ti_{1-x}Al_xN regions [44]. However, there has been evidence to show that coherent nano-grains of cubic AlN may form as an intermediate phase before ω -AlN, which may largely influence hardness due to age-hardening [44–46]. High temperature aging treatments have been shown to initiate this process and substantially increase

hardness [44]. Figure 2.14 shows the aforementioned age hardening for $\text{Ti}_{0.33}\text{Al}_{0.67}\text{N}$ coatings, in addition to the degradation of hardness in TiN with increasing annealing temperature. The apparent over-aging, or decrease in hardness with increased annealing temperature, is said to be caused by formation and growth of ω -AlN. Hardness likely decreases due to the fact that ω -AlN has a lower hardness of around 18-20 GPa, while coarsening may also play a role. The concentration of Al in the coating or target may also have an effect on the phases present and hardness as shown in Figure 2.15 [47]. As the Al concentration is increased, the probability of forming ω -AlN increases, resulting in relatively low hardnesses. The variation in hardness between deposition techniques is difficult to discern due to the increased number of variables that affect hardness compared to TiN. Nevertheless, some reported hardness values for $\text{Ti}_{1-x}\text{Al}_x\text{N}$, having $0.5 \leq x \leq 0.7$, are in the range of 26- 45 CAE [48][49], 22-29 GPa for DCMS [50] [51], and 24-35 GPa for PMS [52].

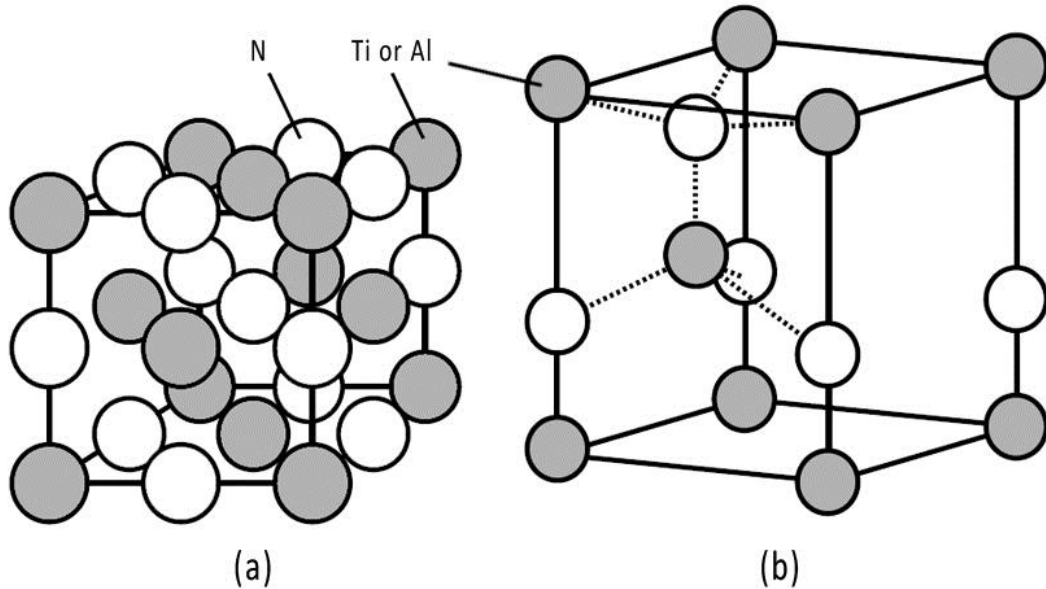


Figure 2.13 Schematic of (a) δ -(Ti,Al)N FCC rock-salt structure and (b) ω -(Ti,Al)N wurtzite structure.

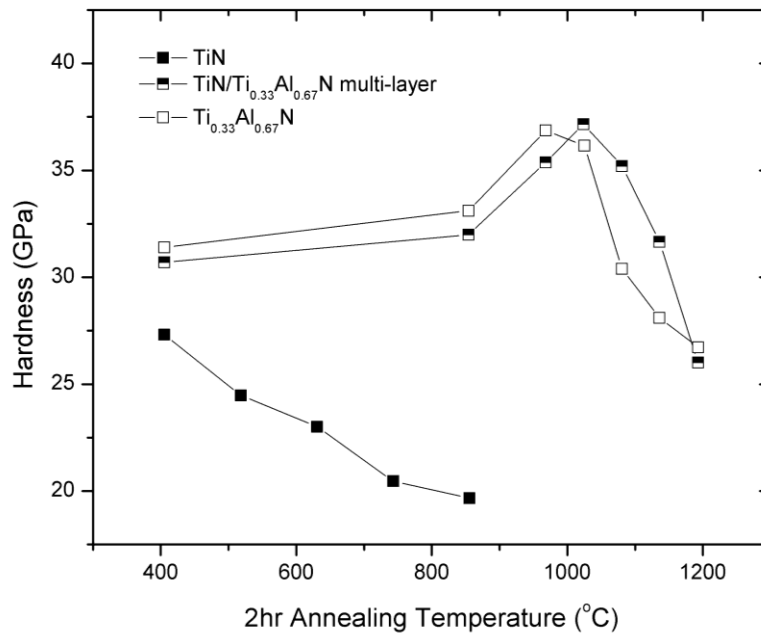


Figure 2.14 Hardness values for deposited TiN and Ti_{0.33}Al_{0.67}N coatings annealed at several temperatures. Adopted from [44].

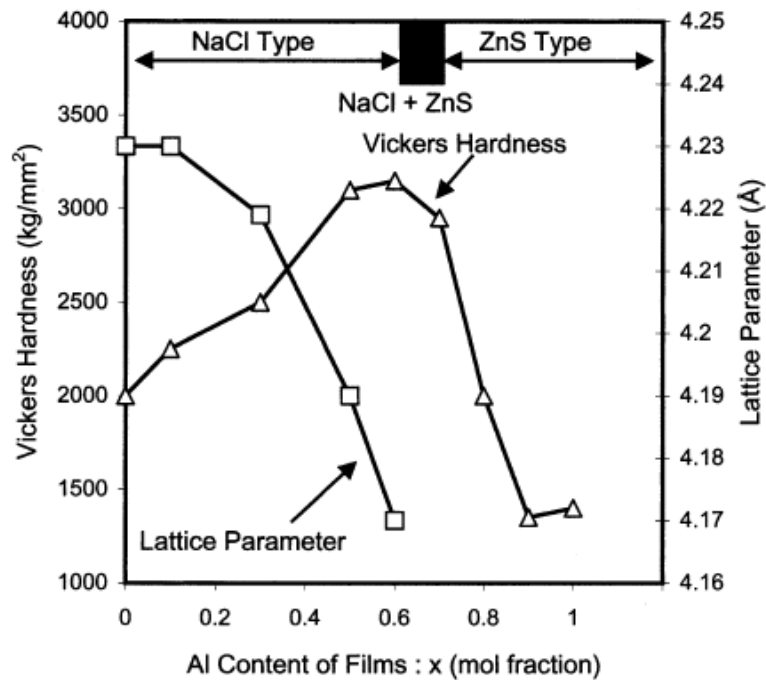


Figure 2.15 Hardness values for CAE deposited Ti_{1-x}Al_xN coatings with varying Al compositions [47].

2.6 Substrate Effects

Optimal performance for PVD coatings is heavily dependent on the substrate material. Conditions at the coating-substrate interface such as roughness, microstructure, texture, and difference in thermal expansion will impact how the coating adheres and grows. This study investigates the properties of several substrate materials (Ti-6Al-4V, IN718, SS304, Si (100)) to determine their suitability for coating with TiN and TiAlN in addition to discovering any obstacles that may come up in future work.

2.6.1 Ti-6Al-4V

When heated, pure Ti undergoes a phase transformation at 882.5°C from α to β phase [53]. Additional elements such as Al, O, C, or N may be added to stabilize the lower temperature α phase. Likewise, elements such as V and Mo are used as β stabilizers. Due to the stabilizing elements in Ti-6Al-4V, it is common to have both phases in the final microstructure, although the majority will be the α phase. The alloy's strength is derived from solid solution strengthening, grain refinement, and precipitate strengthening attainable through thermomechanical treatments. The elements used for creating this alloy along with its common impurities are provided in Table 2.2.

Ti-6Al-4V is the most widely used titanium alloy in both the aerospace and medical industries. It accounts for over 50% of all titanium alloys used due to its high strength-to-weight ratio, excellent formability, and corrosion resistance [53]. One of the disadvantages of Ti-6Al-4V is its poor wear resistance. Most Ti alloys are vulnerable to galling, a type of adhesive wear. The mechanical shear response, strong attraction to oxide surfaces, and relatively low tensile strength are characteristics that contribute to high coefficients of friction and high wear rates. When the c/a ratio in a hexagonal crystal is low (<1.63), such as in α Ti-6Al-4V (~ 1.58), non-basal slip planes are more active during wear resulting in intersecting dislocations on multiple slip planes, increased work hardening, increased resistance to shear, increased true area of contact, and higher COF [54]. Due to these properties, in friction applications, Ti-6Al-4V will tend to bind, seize, or smear [53]. By adding hard, wear resistant coatings like TiN and TiAlN, the use of Ti-6Al-4V in applications that require high strength to weight ratio and are subject to abrasion or wear might be extended.

2.6.2 Inconel 718

Nickel-base superalloys have always played an important role in high temperature turbine engines. Developed in the 1960's, IN718 is the most commonly used superalloy for aircraft engine components where service temperatures are below 700°C [55, 56]. The majority of its applications are in turbine engines, but it is also used in applications that require high strength, thermal stability, and

weldability. Although IN718 exhibits good mechanical properties and corrosion resistance, IN718 can often seize in contact wear situations due to its low wear resistance [57]. PVD coatings could provide improved wear resistance and increased part longevity.

IN718 utilizes both solid solution and precipitate strengthening similar to Ti-6Al-4V, but is slightly more complex. The austenitic matrix of IN718 is strengthened by several different phases. The matrix phase is referred to as γ and is composed of mainly Ni, Fe, Cr and other substitutional and interstitial elements. The main strengthening phase, γ'' , made of body-centered tetragonal Ni_3Nb precipitates within face-centered cubic γ grains. Meanwhile, some γ' - $\text{Ni}_3(\text{Al,Ti})$ may also form. The composition contains at least 15 elements, 10 more than Ti-6Al-4V (See Table 2.2 and Table 2.3). The primary strengthening phase is γ'' , while Nb and Mo-based carbides also provide strengthening of grain boundaries. The crystallographic mismatch between the matrix, γ , and γ'' produces strains up to 2.9%, which contribute to IN718's high strength [56]. Coherency between the γ matrix and γ'' precipitates help give IN718 excellent thermal stability. Additionally, slow diffusing elements help prevent overaging. Carbides also provide thermal stability by reducing creep via grain boundary sliding.

Table 2.2 ASM standard composition for Ti 6Al-4V [53] with EDS measurements.

Alloying Element	Standard wt.%	Measured wt.%	Alloying Element	Standard wt.%	Measured wt.%	Alloying Element	Standard wt.%	Measured wt.%
Ti	Balance	86.42*	V	4	4.44*	O	≤ 0.20	2.13*
Al	6	6.04	Fe	≤ 0.25	0.97*			

*This value is inaccurate due to the limitations of EDS. Overlapping peaks and light elements make concentrations for these elements difficult to determine accurately.

Table 2.3 ASM standard composition for IN718 [55] and measured composition using EDS.

Alloying Element	Standard wt.%	Measured wt.%	Alloying Element	Standard wt.%	Measured wt.%	Alloying Element	Standard wt.%	Measured wt.%
Ni	50-55	49.81*	Ti	0.65-1.15	1.41*	Cu	≤ 0.3	1.27*
Cr	17-21	19.89	Co	≤ 1.0	1.03	C	≤ 0.08	0.00*
Fe	17	17.48*	Al	0.2-0.8	0.75	P	≤ 0.015	0.09
Nb	4.75-5.5	5.86	Si	≤ 0.35	0.26	S	≤ 0.015	1.53*
Mo	2.8-3.3	NA	Mn	≤ 0.35	0.62	B	≤ 0.006	0.00*

*This value is inaccurate due to the limitations of EDS. Overlapping peaks and light elements make concentrations for these elements difficult to determine accurately.

2.7 Surface Roughness

Substrate roughness is an important factor to consider when examining adhesion and wear in PVD coatings. In general, PVD coatings tend to show better adhesion strength, lower residual stress, lower coefficients of friction, and even increased corrosion and oxidation resistance when deposited on substrates with lower roughness [58]. A study done by Lee [59], showed that roughness of the substrate was transferred to the roughness of 2.36 μm thick CrN coatings deposited with CAE. The roughnesses, R_a , for the substrates were $R_a=100, 200, \text{ and } 310 \text{ nm}$ before the coating was applied. After the CrN coating the recorded roughnesses were $R_a=130, 220, \text{ and } 330 \text{ nm}$. The slight 20-30 nm increase may be attributed to roughness gained during coating growth. Several factors may contribute to the gained roughness. One possibility is that roughness is increased on the substrate from pre-etching with Ar, which is then transferred to the coating roughness. Coating grain size and adatom mobility may also contribute. With limited adatom mobility, surface atoms are not able to remove asperities produced during growth [60]. Tall macroparticles can create high localized electric fields, which can lead to preferred growth and increased roughness.

Bull and Rickerby found that critical failure loads for scratch testing were strongly influenced by substrate roughness for $R_a > 50 \text{ nm}$, and for $R_a < 50 \text{ nm}$ the critical loads were virtually unaffected. However, Li *et. al.* [60] showed that other properties including scratch critical loads were affected by substrate R_a values between 4 and 18 nm. Therefore, since the measured substrate R_a values lie within this range, roughness was considered when discussing results.

CHAPTER 3: EXPERIMENTAL PROCEDURES

3.1 Substrate Preparation

The substrate materials, Ti-6Al-4V and IN718, were provided by GE Aviation while AISI 304 stainless steel (304SS) and (100) Si substrates were provided by Penn Stainless Products, Inc. and University Wafer, respectively. The additional 304SS and (100) Si wafer substrates were added for comparison to literature and for ease of characterization. Samples were sectioned into approximately 1×1×0.375 inch coupons using an oil-cooled high speed ceramic saw. The Ti-6Al-4V and IN718 coupons then underwent heat treatment by GE Aviation. Silicon and SS304 samples were as-received with mirror finishes, while IN718 and Ti-6Al-4V coupons were polished to a mirror finish. The roughness, R_a , was kept to $R_a \leq 25$ nm and verified using an optical profilometer (Veeco, Inc.). To reduce the formation of oxides and contaminants as much as possible samples were polished with the final polishing step then ultrasonically cleaned in acetone followed by alcohol and blow dried with helium gas immediately before each deposition.

3.2 Deposition Process

A four-cathode closed-field unbalanced magnetron sputter (CFUBMS) system was used for all depositions. A drawing of the top view of the chamber is shown in Figure 3.1. The four substrates, Si, SS304, IN718, and Ti-6Al-4V were mounted on the substrate holder 70 mm away from the target surface. For some depositions a thermocouple mounted to the back of the substrate holder was used to measure temperature at different stages of the deposition process. Before each deposition, a base pressure $< 6.0 \times 10^{-6}$ Torr was achieved. New targets underwent a 45 min break-in period using PMS with an average power of 2 kW in pure Ar. Substrates were sputter etched using Ar bombardment with the PMS system (Advanced Energy, Inc. Pinnacle+) prior to each deposition to remove any remaining oxides. Pulse parameters were as follows: -500 V peak voltage, 100 kHz, 1 μ s reverse voltage of 50 V, average power of ~110 W, and etch time of 30 minutes. The targets were sputter etched to remove any poisoning compounds from previous depositions. The power supply used for depositing the new coating was also the one used for etching the target. Both sample and target etching was done at a constant pressure of 8 mTorr. Depositions were conducted using three different power supplies: DOMS prototype system (ZPulsar, LLC), MPPMS (ZPulsar SOLOTM), and PMS. Three sputter targets, supplied by Plansee Inc., were used for depositing TiN and $Ti_{1-x}Al_xN$ coatings with compositions: 99.6+ wt.% Ti, 50Ti-50Al, and 30Ti-70Al. Pulse parameters used for all three power supplies are contained in Table 3.1 and Table 3.2.

Table 3.1 Pulse parameters used for depositing TiN coatings.

Deposition Parameters												
Power Supply	τ_{macro} (μs)	$\tau_{\text{weak}}/\tau_{\text{strong}}$ (μs)	$\tau_{\text{on}}/\tau_{\text{off}}$ (μs)	f (kHz)	P_{avg} (kW)	P_p (kW)	P_d (kW/cm ²)	V_p (V)	I_p (A)	Pressure (mTorr)	Substrate Bias (V)	
PMS	-	-	10/1	100	2.0	≈ 2.3	≈ 0.015	-310 (avg.)	6.5 (avg.)	5	floating & -90	
DOMS	950	-	2/40	0.78	2.0	90	0.61	-750	120	3, 5, 7, 9	floating, -30, -60, -90	
MPPMS	1250	500/750	10/8	0.23	2.0	12	0.083	-330	37	5	floating	

Note: The term τ_{macro} refers to the length of the macropulse. The terms τ_{weak} and τ_{strong} are the pulse lengths for the weak and strong ionization stages in MPPMS. The micropulse on and off times are τ_{on} and τ_{off} . The macropulse frequency is labeled f . For average power, peak power, peak power density, peak voltage, and peak current the labels are P_{avg} , P_p , P_d , V_p , and I_p , respectively.

Table 3.2 Pulse parameters used for depositing TiAlN coatings.

Deposition Parameters												
Power Supply	τ_{macro} (μs)	$\tau_{\text{weak}}/\tau_{\text{strong}}$ (μs)	$\tau_{\text{on}}/\tau_{\text{off}}$ (μs)	f (kHz)	P_{avg} (kW)	P_p (kW)	P_d (kW/cm ²)	V_p (V)	I_p (A)	Pressure (mTorr)	Substrate Bias (V)	
PMS	-	-	10/1	100	2.0	≈ 2.3	≈ 0.015	-325 (avg.)	6.5 (avg.)	5	floating	
MPPMS	1250	500/750	10/8	0.23	2.0	10	0.068	-400	25	5	floating	

Note: See Table 3.1 for definitions of terms.

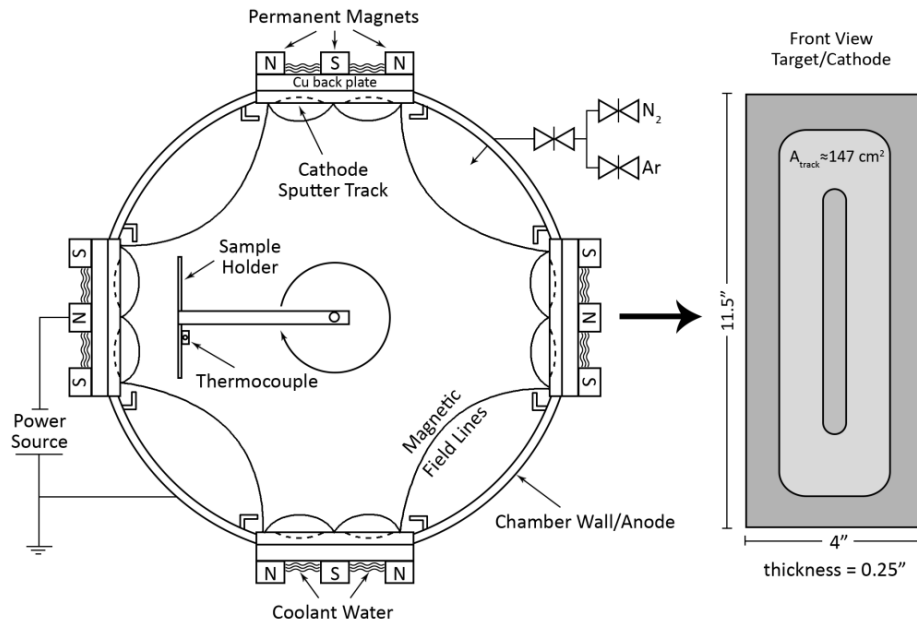


Figure 3.1 Drawing of CFUBMS chamber with labeled components and front view of metal target (Ti, 50Ti-50Al, or 30Ti-70Al). The power source can be detached and reattached to any cathode/target. The sample can be rotated remotely toward the active target. A separate power supply was attached to sample holder and grounded outside the chamber for coatings deposited with substrate bias.

A Ti adhesion layer, approximately 100 nm thick, was deposited prior to the TiN or Ti_{1-x}Al_xN depositions. A diagram showing a typical coating configuration in this study can be seen in Figure 3.2. Deposition times were varied between 30 and 45 min to achieve coating thicknesses around 2 μm. An average target power of 2 kW was used for all depositions. A built-in oscilloscope in the MPPMS system was used to measure the pulse profiles for MPPMS (Figure 3.3). A Tektronix TDS2014 oscilloscope was used to record the applied pulse profile and generated substrate ion current for the DOMS-deposited coatings. A typical pulse profile for a TiN coating deposited with DOMS can be seen in Figure 3.4.

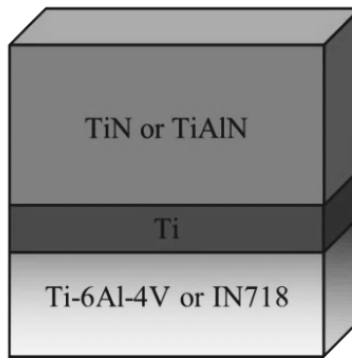


Figure 3.2 Diagram of the coating configuration used for this study.

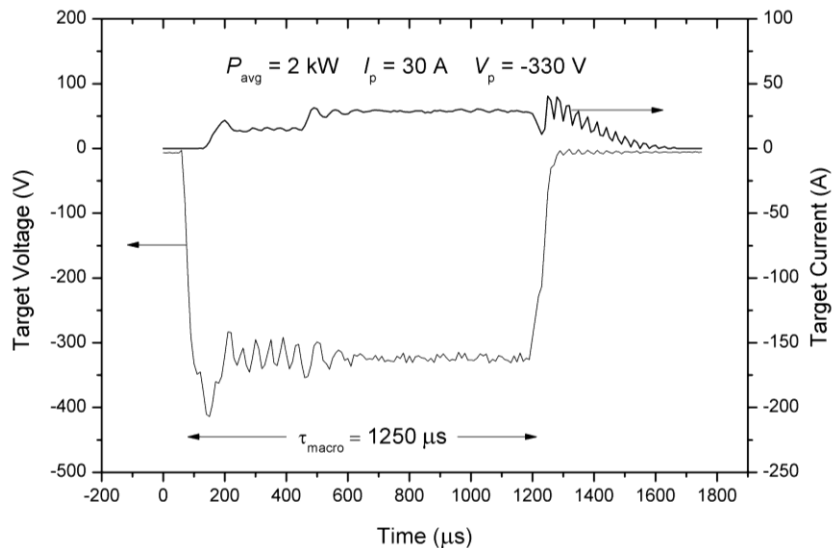


Figure 3.3 Measured voltage and current waveforms for a TiN coating deposited with MPPMS.

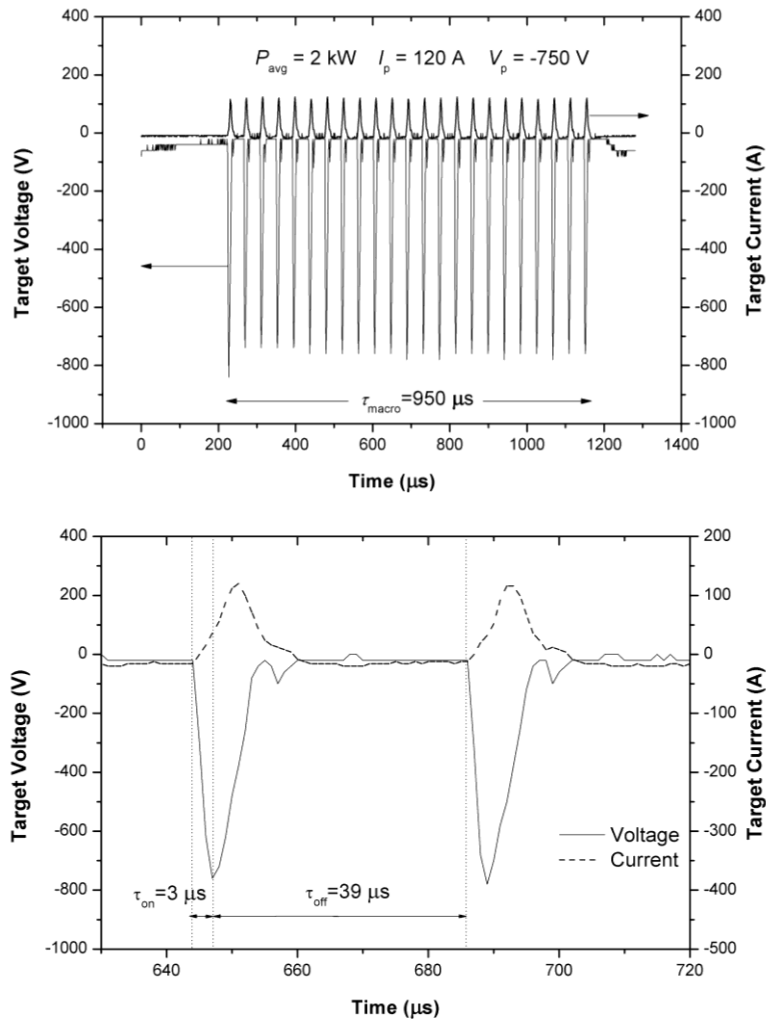


Figure 3.4 Measured voltage and current waveforms for a TiN coating deposited with DOMS. (top) An entire macropulse cycle and (bottom) a high resolution graph of the individual micropulses.

Several preliminary depositions were necessary for optimizing the N_2 flow rate and coating composition before any studies were conducted. These preliminary depositions were necessary for each power supply and coating system. For TiN coatings, the optimal composition was determined based on the final coating color, which is very sensitive ($\approx 1\%$ N_2 tolerance) to N_2 content. A gold appearance was considered to have the ideal composition, whereas silver or brown tints indicated that the N content was deficient or excessive, respectively. For $Ti_{1-x}Al_xN$ ($0.5 \leq x \leq 0.7$), the ideal color is grey eggplant purple as suggested by an industry mentor, which indicates a proper 50 at.% N concentration. However, determining the N concentration solely on color was inaccurate, due to the alternative lighter purple or

darker grey that indicated deficient or excess N. Therefore, N₂ flow percentage was optimized based on hardness and deposition rate.

A study of how working pressure and substrate bias affect microstructure and properties was performed for TiN coatings. Several coatings were produced using DOMS following the experimental matrix of bias voltages and working pressures in Table 3.3. No depositions were made with substrate bias for MPPMS-deposited coatings although all three methods (DOMS, MPPMS, and PMS) were used for depositing coatings with floating bias using a 5 mTorr working pressure.

Table 3.3 Experimental matrix representing TiN coatings with different substrate biases and working pressures. DOMS coatings are indicated by X, PMS coatings are indicated by X*.

Working Pressure (mTorr)	Substrate Bias (V)			
	Floating	-30	-60	-90
3	-	-	X	-
5	X,X*	X	X	X,X*
7	-	-	X	-
9	-	-	X	-

3.3 Characterization of Microstructure and Composition

The following sections describe the characterization techniques and methods used to analyze the substrate and coating structures. Several components, such as morphology, grain size, and crystallography/texture were studied.

3.3.1 Scanning Electron Microscopy (SEM)

Substrate alloys, IN718 and Ti-6Al-4V, were polished and etched to reveal their microstructure, which was inspected using an FEI Quanta 600i Environmental SEM and a JEOL JSM-7000 FESEM. A backscatter detector and EDS were utilized to distinguish and identify different phases within the microstructure.

To analyze the coating cross-section microstructure and thickness, a thin section of coated Ti-6Al-4V was cut using a high speed saw. The section was cut from the bottom of the substrate toward the coating to create a small cross-sectional area. The cut sample was submerged in liquid nitrogen for 5 min prior to fracturing it with pliers. Cooling the sample was meant to encourage brittle cleavage or

intergranular fracture to help reveal the grain structures of the TiN and Ti_{1-x}Al_xN coatings. The FESEM was used for analyzing the coating thicknesses and microstructures of the fracture surfaces.

Depositions of Ti_{1-x}Al_xN were conducted using alloyed Ti_{1-x}Al_x targets of compositions x=0.7 and x=0.5. Compositional analysis of Ti_{1-x}Al_xN coatings was performed with energy-dispersive X-ray spectrometry (EDS, a.k.a. EDX). Compositions of N were ignored due to the limitation of EDS for quantifying light elements. The software TRIM was used for investigating the Ar⁺, N⁺ and self-sputtering yields of Ti and Al to help explain the EDS results.

3.3.2 Transmission Electron Microscopy (TEM)

Initially, a sandwich and dimple grinding method was attempted for preparing TEM cross-sectional samples. Due to the residual stresses and ductile nature of the IN718 substrates, efforts were unsuccessful in producing a sample revealing the entire cross-sectional area of the coating. Subsequently, a focused ion beam (FIB) was used to prepare all TEM samples presented in this study. Lift-out samples of TiN deposited with DOMS using floating and -90 V bias onto IN718 were made. Other samples included Ti_{1-x}Al_xN samples deposited with MPPMS onto IN718 using floating bias and target compositions 50Ti-50Al and 30Ti-70Al. To minimize any coating/substrate curvature caused by residual stresses, a specific lift-out geometry was selected, namely, 15 μm wide, 2 μm thick, and 5 μm tall. A 1-3 μm thick Pt layer was deposited onto the top of the coating surfaces. Two 4 μm wide windows (<100 nm) thick were then prepared for final thinning. In some cases, a final wedge cutting step was used to produce a very thin area toward the center of each window for minimal grain overlap through thickness. All bright field (BF), dark field (DF), and selected area diffraction pattern (SADP) images were captured using a Philips CM200 TEM operated at 200 kV and a Philips CM12 TEM operated at 120 kV.

3.3.3 X-Ray Diffraction (XRD)

Characterization of the crystallographic texture, grain size, and phases present for the coatings and substrates was performed using XRD (PANalytical X'Pert PRO with variable divergence slits) operating in θ -2 θ mode with Cu K _{α 1} ($\lambda = 1.5406 \text{ \AA}$). In this mode, only information regarding crystallographic plane reflections oriented parallel to the coating/substrate surface may be obtained. The scan range and time used were 20-150° for 15 min. Data was processed in PANalytical X'Pert High Score Plus for stripping K _{α 2} and subtracting background. High Score Plus was also used for Rietveld analysis for quantifying phase volume fractions for the substrates.

Incoherent scattering caused by the edges of grains contribute the broadening of XRD peaks. Using the peak broadening effect measured by the full width at half-maximum (FWHM), grain size (GS) was calculated using the Scherrer formula in Equation (3.1).

$$GS = \frac{0.9\lambda}{FWHM \cos(\theta)} \quad (3.1)$$

Other terms in Equation (3.1) include the wavelength for Cu K_α X-rays (λ=0.15418 nm), the peak position of θ, and the commonly used shape factor of 0.9 [61]. Due to the sampling geometry in θ-2θ mode, this calculation is limited to broadening caused by planes oriented parallel to the substrate surface. This means that Equation (3.1) is only useful for estimating grain size through the thickness of the coating. Additionally, Scherrer's equation does not account for broadening caused by lattice distortions, which is common in coatings due to microstrains created by growth defects. One useful technique for separating GS and microstrain contributions to peak broadening is through the Williamson-Hall relationship in Equation (3.2), where ε is strain.

$$FWHM \cos(\theta) = \frac{0.9 \lambda}{GS} + 4\varepsilon \sin(\theta) \quad (3.2)$$

The intercept from the plot of $FWHM \cos(\theta)$ vs $\sin(\theta)$ could be used to calculate GS without strain contributions. Unfortunately, due to the limited number of peaks available, not enough data points could be used for a measurement. Therefore, GS discussed in the following sections should be treated as underestimates of actual GS, since microstrains are likely present. Peaks used for calculating the average grain size included the δ(111), δ(200), and δ(220) when available. Standard deviations were calculated when more than one peak was used for determining GS. It is important to note that different textures may form at different stages of coating growth and since GS tends to increase with increasing thickness this calculation should be treated as an approximation for the overall GS. Residual stress was also analyzed using glancing angle XRD (GAXRD). More on this analysis is presented in Section 3.4.3.

3.4 Measurement of Coating Properties

The next subsections describe the characterization methods used for describing the tribological properties of coatings deposited in this study.

3.4.1 Nanoindentation

The hardness (H) and modulus (E) for each coating was measured using nanoindentation (XPTM Nanoindenter by MTS Systems) equipped with a Berkovich diamond tip. The indentation depth was set for <10% of the total coating thickness to avoid any influence from the substrate. The indent depth (*h*) was

typically ~150 nm, which by using the area function for a sharp Berkovich tip in Equation (3.3), translates to ~553000 nm² or 0.553 μm².

$$A = 24.56h^2 \quad (3.3)$$

Grain diameters in coatings for this study varied from 10-60 nm, thus no anisotropic effects should occur from sampling a small number of grains. However, strong textures that are common PVD coatings may cause anisotropic effects. Poisson's ratio was estimated to be 0.25 for both TiN and Ti_{1-x}Al_xN. This approximation is reasonable since a variation of 0.25±0.1 results in about 5% error in measurements of elastic properties [13]. The H and E values were calculated based on the unloading curve. A total of 16 indents were made per sample with at least 10 successful indentation cycles used for calculating average H and E values.

Hardness and modulus can help predict the resistance to plastic deformation and wear resistance of a coating. Indentations studies done by Johnson [62] showed that the critical load needed to initiate plastic deformation (*P*), using an indenter with radius, *r*, was equal to the relationship found in Equation (3.4). Equation (3.4) assumes that the H is approximately three times the yield stress of the indented material [63].

$$P = 0.78 r^2 \frac{H^3}{E^2} \quad (3.4)$$

This shows that the resistance to plastic deformation is proportional to H³/E². Thus, high hardness and low modulus are desirable for enhanced fracture toughness and elastic strain to failure, properties which are difficult to measure directly for thin films. H³/E² values will be shown along with H/E values, also suggested by Musil [64] as valuable for predicting wear in coatings.

3.4.2 Wear and Adhesion

A microscratch tester (CSM instruments, LLC) was used in parallel with a Rockwell C hardness tester to evaluate the adherence of the coatings. The microscratch tester is equipped with a Rockwell C diamond indenter which was progressively loaded from 0.3 to 30 N at a rate of 1N/m over a length of 5 mm. The scratch tracks were examined and features were classified following the ASTM C1624-05 standard for scratch testing ceramic coatings [65].

The Rockwell C indentation test was utilized in addition to scratch testing for evaluating adhesion. The test was developed in Germany and is labeled as #3198 under VDI guidelines. The scale for ranking adhesion is known as the HF scale (see Figure 3.5) and ranges HF1-HF6, with HF1-HF4 usually designated as having "sufficient" adhesion [66]. Images of the indents and the surrounding damage were taken with an ESEM in mixed backscatter and secondary electron mode.

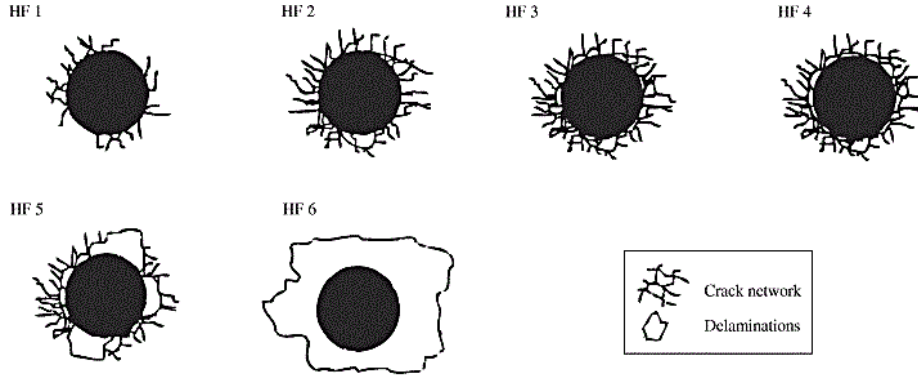


Figure 3.5 Rockwell-C adhesion test ranking scale, known as the HF scale adopted from [66].

Wear properties were examined using a ball-on-disk tribometer (Center for Tribology, Inc.). Tests were conducted with a 5 mm WC ball at 100 rpm with an applied load of 1 N normal to the surface for 60 min and a race track diameter of 14 mm. If during the test the ball broke through the coating and the substrate was exposed, an additional test was conducted using the same sliding velocity for a shorter time/distance. The wear track profile was recorded with an optical profilometer. Wear rates were calculated based on wear volume of the race track and total distance traveled by the ball.

3.4.3 Residual Stress

Residual stress was determined using a GAXRD (SIEMENS Kristalloflex-810, Bragg-Bentano beam) operating at 30 kV and 20 mA with Cu K_{α} ($\lambda=0.15418$ nm) radiation. The $\sin^2 \psi$ method was employed for determining the residual stress. This method requires operating in ϕ - 2θ mode, where the incident beam is held at a constant glancing angle, ϕ , and the detector is scanned through a desired 2θ range. When ϕ is changed, new planes at angle $\psi = \theta - \phi$ with respect to the substrate diffract toward the detector. Residual stresses can create biaxial strains parallel to the substrate, which in turn, can produce a strain normal to the substrate surface following Poisson's ratio (ν). When present, residual strains will cause the peak positions to shift along 2θ when ψ is changed. The lattice parameter can be plotted with respect to $\sin^2 \psi$ and then fit with a linear line. The slope, m , is then used to calculate the residual stress (σ_{residual}) with Equation (3.5) [67].

$$\sigma_{\text{residual}} = m \left(\frac{E}{1 - \nu} \right) \quad (3.5)$$

This assumes a biaxial stress state without shear components and the absence of significant stress gradients or anisotropic distortions in strain. Unfortunately, this is often not the case in TiN PVD coatings, but it may serve as a reasonable estimate for describing residual stresses present within the

coating. Nanoindentation results were used for respective values of E , while 0.25 was used as Poisson's ratio for all calculations.

The (111), (220), (311), and (222) peaks with enough intensity throughout all the $\sin^2 \psi$ values were used in calculating σ_{residual} . The glancing angles: 6° , 10° , and 14° , were chosen based on calculated X-ray penetration depths that were deep enough to penetrate the entire coating thickness. Penetration depths were calculated using an averaged absorption coefficient of 877 cm^{-1} for TiN [68], a minimum fraction of intensity of 0.05, and Equation (3.6) [69].

$$G_x = e^{-\mu x \left[\frac{1}{\sin \phi} + \frac{1}{\sin(2\theta - \phi)} \right]} \quad (3.6)$$

A plot showing the fraction of diffracted intensity, G_x , with respect to the depth of a TiN film along with calculated penetration depths can be seen in Figure 3.6. It shows that using different glancing angles results in sampling different depths of the coating. Therefore, if a stress gradient is present, then $\sin^2 \psi$ function will not be linear. Larger glancing angles were used in attempt to minimize any stress gradient effects.

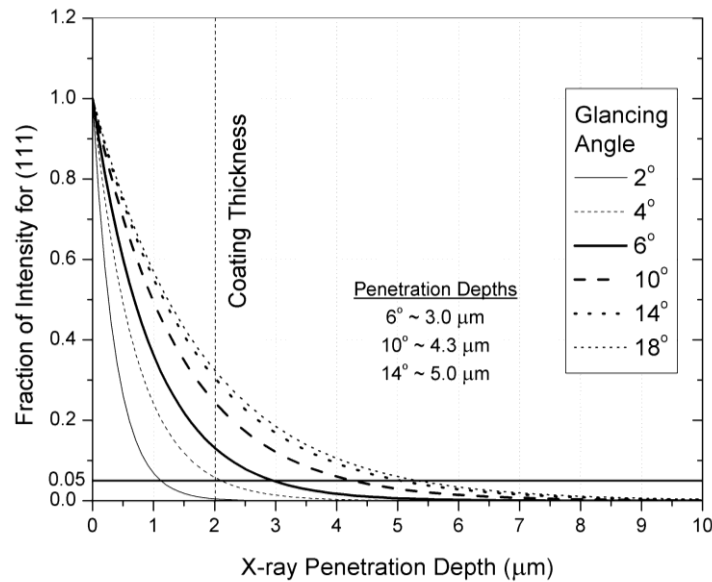


Figure 3.6 Fraction of peak intensity from incident x-rays with incident angles (ϕ), calculated using Equation (3.6). Included are calculated values of penetration depths. Glancing angles used in this study are 6° , 10° , and 14° .

All available XRD peaks were fitted using a Pearson VII fitting function in Origin Pro 8.5 graphing software, by which peak positions were derived for calculating lattice parameters. A $\sin^2 \psi$ plot of a DOMS-deposited TiN coating on Ti-6Al-4V using -90 V bias is shown in Figure 3.7. Note that a shift in lattice parameter was observed for the (200) peaks in all coatings where the (200) peak were

observed. The explanation for the shift is unclear, although the slope of the (200) data points usually followed the same slope as data point from other peaks. Thus, (200) was discarded for creating a linear fit. There error bars in residual stress calculations are based on the standard error of the slope of the linear regression fit in the $\sin^2\psi$ plots.

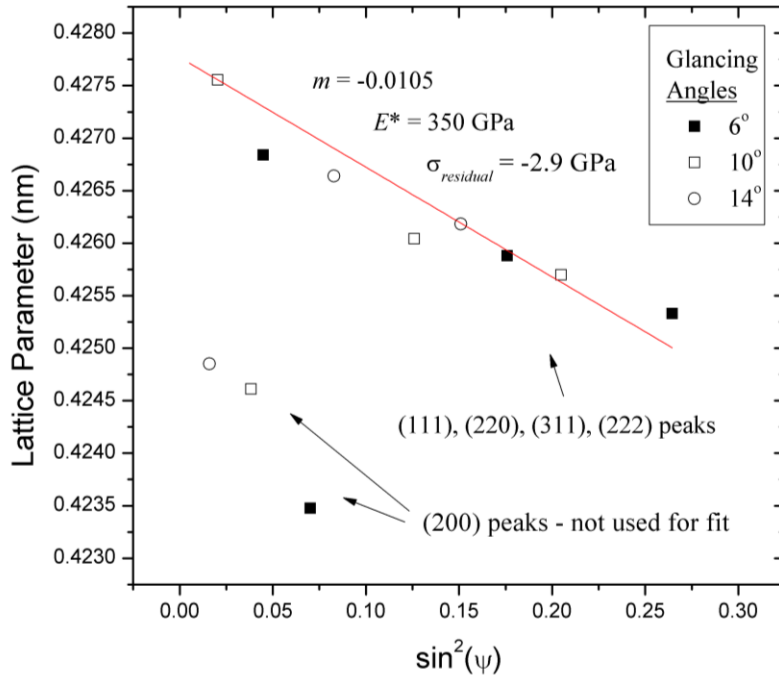


Figure 3.7 $\sin^2\psi$ plot of TiN deposited with DOMS using -90 V bias onto a Ti-6Al-4V substrate. The residual stress using the linear fit is shown.

CHAPTER 4: RESULTS

4.1 Substrate Characterization

The microstructure of the substrate can reveal important information about surface conditions onto which the coating will grow. Characteristics like grain size and volume fraction of phases can often give clues to how the coating will bond to the surface and what mechanical properties to expect. Hard phases like carbides can create uneven surface topography which may affect the surface roughness and wear properties.

4.1.1 Microstructure

The structure of Ti-6Al-4V alloy used in this study consisted of α grains with β located at α - α grain boundaries as shown in Figure 4.1. The image also reveals an average grain size of $\sim 3.5 \mu\text{m}$ using a line-intercept grain boundary counting technique. The lighter grains represent the β phase, where the darker grains are the α phase. The contrast between phases is a result of a higher average atomic number for β , which tends to generate more backscattered electrons. The micrograph in Figure 4.1 shows that there is a higher volume fraction of α compared to β .

A micrograph for a polished and etched sample of IN718 is shown in Figure 4.1; the small white precipitates are carbides. The average grain size was calculated to be $\sim 13.4 \mu\text{m}$. Closer inspection with EDS revealed that the carbides were high in Nb, Mo, and Ti. These are commonly found in MC, $M_{23}C$, and M_6C carbides, where M represents one of the carbide pairing elements. Formation of MC carbides often occurs during the ingot casting process and may later form $M_{23}C$ or M_6C carbides during heat treatments [3]. These heat treatments also lead to the formation of annealing twins, which may describe those seen in Figure 4.1. These carbides tend to have very high hardness relative to the matrix material. Due to differences in polishing rates, the carbides sometimes created high points on the surface.

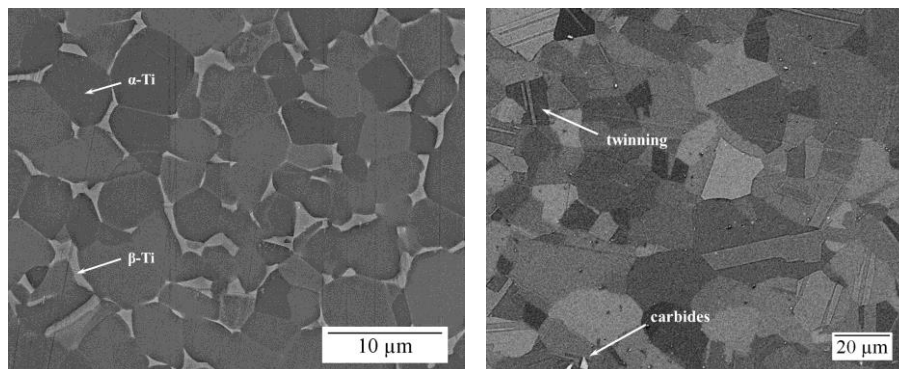


Figure 4.1 Backscattered SEM image of etched (left) Ti-6Al-4V and (right) IN718.

4.1.2 X-ray Diffraction

Rietveld analysis conducted on XRD patterns in **Error! Reference source not found.** revealed a concentration of $\sim 92\%$ α and $\sim 8\%$ β . The high volume fraction of α would indicate that this alloy is likely to suffer poor wear resistance as explained in Section 2.6.1. This behavior was confirmed through observed smearing and galling during polishing. This characteristic makes Ti-6Al-4V a favorable candidate for improving its tribological properties. Rietveld analysis for IN718 revealed that carbides represented approximately 1.00% of the total volume.

Texture is defined as the preference of certain crystal orientations in a polycrystalline material. Texture is often caused by processing steps such as solidification and rolling where highly directional thermal or stress gradients are present. The degree of texture depends on the fraction of grains that have the same preferred crystal orientation. The mechanical properties and adherence of PVD coatings are often influenced by the coating's texture, which, in some cases, can be influenced by the substrate texture.

Error! Reference source not found. and **Error! Reference source not found.** shows the patterns taken for Ti-6Al-4V, IN718, and SS304. Since Si (100) is a single crystal, characterizing its texture is unnecessary as the main orientation is the (100) plane parallel to the substrate surface. These patterns were important for separating substrate patterns from patterns belonging to the coating.

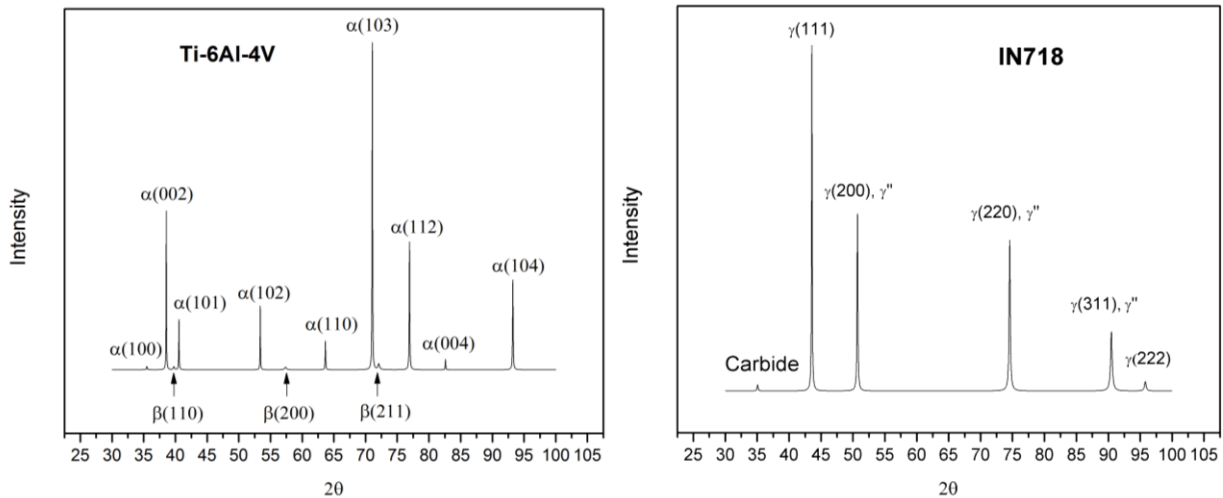


Figure 4.2 X-ray diffraction patterns for (left) Ti-6Al-4V and (right) IN718 using 2θ scan mode.

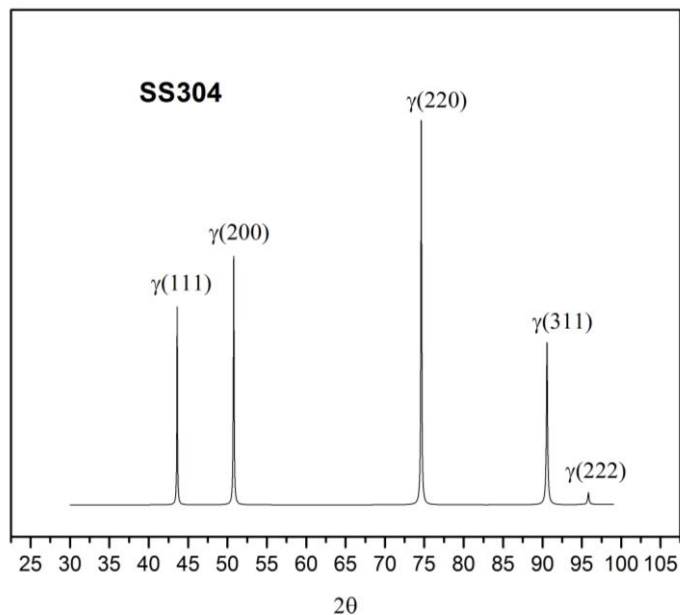


Figure 4.3 X-ray diffraction pattern for SS304 using 2θ scan mode.

4.1.3 Surface Roughness

Surface roughness was measured for Ti-6Al-4V, IN718, and SS304 before and after depositing a TiN coating with DOMS. The roughness, R_a , values and topographical renderings of the substrates before being coated are shown in Figure 4.4. Also included are R_a values recorded after the film was coated with TiN, except for SS304 which had delamination issues. IN718 had the lowest R_a , but often had tall features sometimes reaching 1 μm above the surface which has been attributed to the hard carbides. Minimizing time spent polishing with the diamond slurry was critical for reducing the size of the asperities. The second lowest R_a was seen for SS304; no interesting topographical features were noted. As expected, the highest R_a was produced by Ti-6Al-4V due to its unstable wear behavior. Smearing and galling were difficult to avoid and hydrogen peroxide (30% concentration) was sometimes sprayed while using fine grits to help remove deformed surface material. Generally a lower R_a is more desirable in PVD coatings, which depend on good atomic intermixing/bonding between the substrate for good adhesion strength. High R_a (>50 nm) can lead to shadowing effects at the beginning of the deposition, which leads to voids and improper bonding. There was little difference observed in R_a between the uncoated and coated substrates.

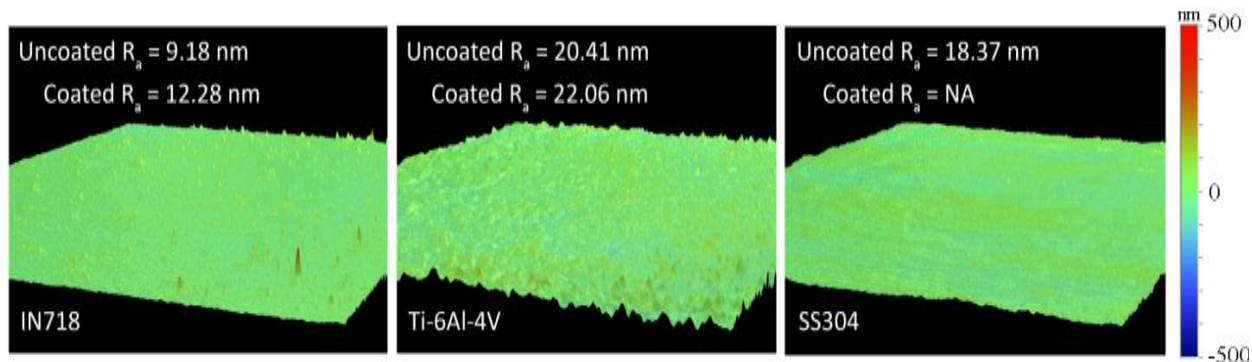


Figure 4.4 Topographical 3-dimensional rendering of uncoated substrates collected with an optical profilometer. Also shown are the calculated R_a values for uncoated and coated substrates with TiN deposited with DOMS. An R_a measurement for coated SS304 was not available due to delamination of the coating.

4.2 TiN

The following subsections describe the results found through the characterization of TiN coatings deposited with different deposition conditions such as: substrate bias, working pressure, and power supply.

4.2.1 Microstructure and Crystallographic Texture

Substrate Bias Effects

To study the effects of substrate bias on microstructure for DOMS-deposited TiN coatings, several coatings were deposited using biases ranging from floating to -90 V and a constant working pressure of 5 mTorr. A comparison of the microstructures can be seen in the micrographs in Figure 4.5. When deposited with a floating substrate bias the morphology possesses an upper Zone Ic structure with narrow columnar grains that extend from the surface to the substrate. At -30 V bias, the structure resembles a lower Zone T with slightly wider grains that are disrupted between the surface and substrate, possible evidence of renucleation. As the substrate bias is increased to -60 V, a mid-Zone T structure is observed with more V-shaped grains interrupted through the thickness of the coating. Finally, at -90 V bias, an upper Zone T microstructure is formed with similar V-shaped grains as in the -60 V sample.

Closer inspection of defects and grain structure was conducted with transmission electron microscopy (TEM). The TiN coating deposited with floating bias shows a narrow columnar grain structure with small grain widths parallel to the surface and longer grain lengths normal to the surface (see Figure 4.6). There was little evidence of voids, which are often observed along grain boundaries and sometimes within grains for fibrous Zone I structures. Though, underlying material and substantial

variations in contrast from other factors made them difficult to identify. From TEM images like in Figure 4.6, the grain width for grains halfway through the thickness varied between 10 to 20 nm. Grain length could not be easily assessed, but grain width and length appeared to increase from the bottom of the coating toward the surface.

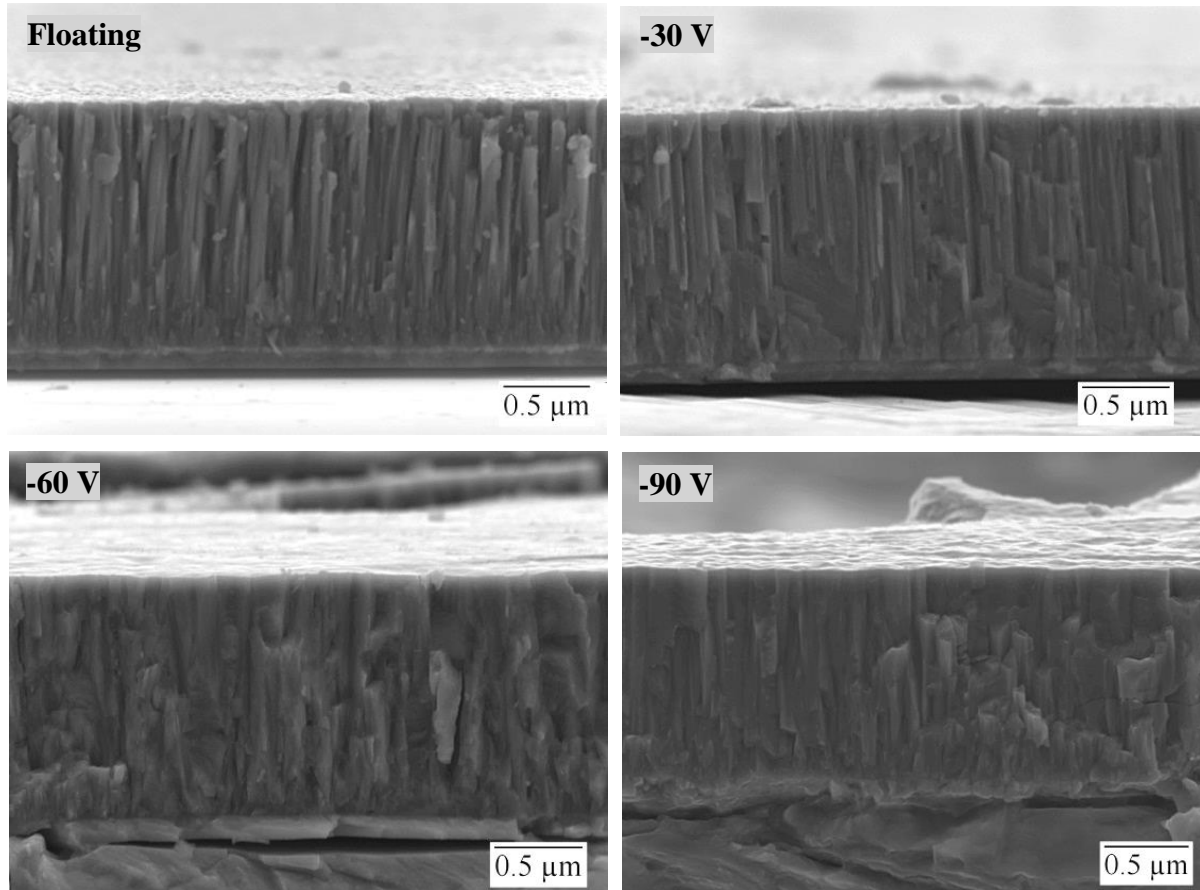


Figure 4.5 SEM images of fractured cross sections of TiN coatings deposited on Ti-6Al-4V using DOMS with different substrate biases indicated by voltage.

Coatings deposited with -90 V bias did not show any evidence of voids other than those created by FIB (Figure 4.7). The voids/artifacts created by FIB are likely a curtaining effect caused by preferential sputtering at grain boundaries oriented normal to the beam. The grains were wider, varying between 50 to 70 nm, but they also appeared more truncated, as observed in SEM. Substantially higher contrast was observed in the floating bias sample (Figure 4.6). The contrast is likely diffraction contrast caused both by the larger number of grains and possibly local bending within grains. Growth defects may be to blame for contrast seen within grains. Some of these defects include voids, entrapped sputter gases, stacking faults, and lattice distortions. Figure 4.8 shows the interface at the substrate of the floating and -90 V biased samples side-by-side. The Ti adhesion layer appears to have equiaxed grains for both

samples, with the -90 V sample having much less contrast and larger grains compared to the coating deposited with floating bias. The larger grains would indicate higher ion energies and adatom mobilities for the -90 V biased sample as compared to Thorton's SZM. Dark contrast, seen in the Ti layer near the substrate for the -90 V sample, may indicate interdiffusion, though it is more likely strain contrast caused by residual stress. Also noted was some dark contrast beneath the Ti layer in the substrate. It was insensitive to tilting the beam, unlike the bend contours seen in the rest of the substrate. It was also more pronounced in the -90 V sample. One possible explanation is strain contrast, like what was suggested for the contrast in the Ti-layer, although because of the soft nature of Ti compared to IN718, little strain would be expected. It may be possible that the contrast is caused by defects created by bombarding particles similar to a shot peening effect. The high energy particles are likely from the substrate cleaning step in which the surface is sputtered with Ar ions to remove oxides and contaminants. During etching, some of these ions may become imbedded in the substrate near the surface while also creating defects and strains in the surrounding material. Additional bombardment was supplied to the -90 V sample since bias was applied during the deposition of the Ti adhesion layer.

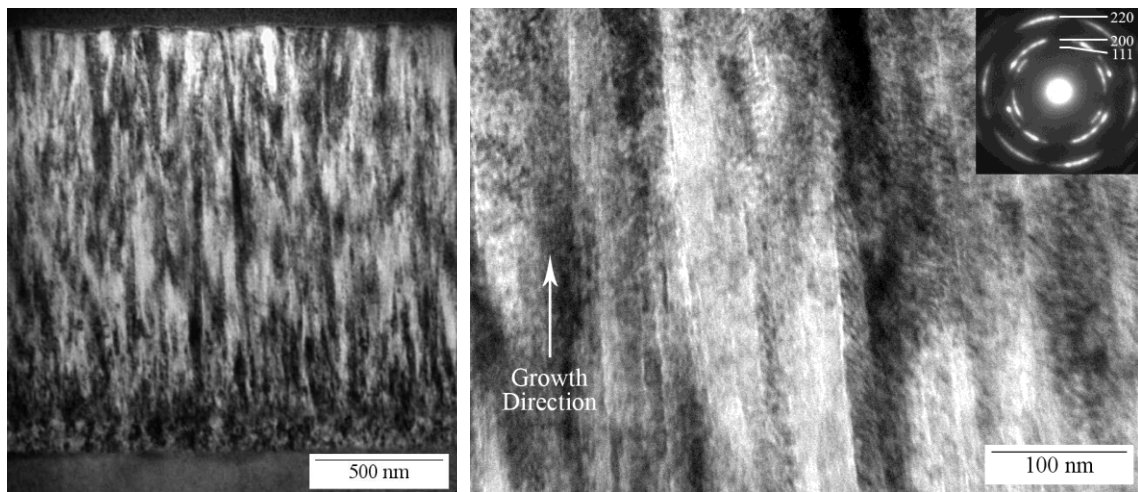


Figure 4.6 TEM micrograph (left) of the overall coating structure of TiN deposited with floating bias onto IN718. A higher magnification image (right) from halfway through the thickness with a SADP in the upper right corner.

The selective area diffraction patterns (SADP) in Figure 4.6 and Figure 4.7 reveal diffraction rings characteristic of polycrystalline materials. Both floating and -90 V biased samples appeared to have some texture development. TiN deposited with floating bias was slightly more random, whereas the -90 V sample had a clear (111) preferred orientation parallel with the substrate surface. It should be noted that the SADP taken for the floating biased coating was for a smaller area compared to the -90 V biased sample, so it may not fully describe overall texture of the coating.

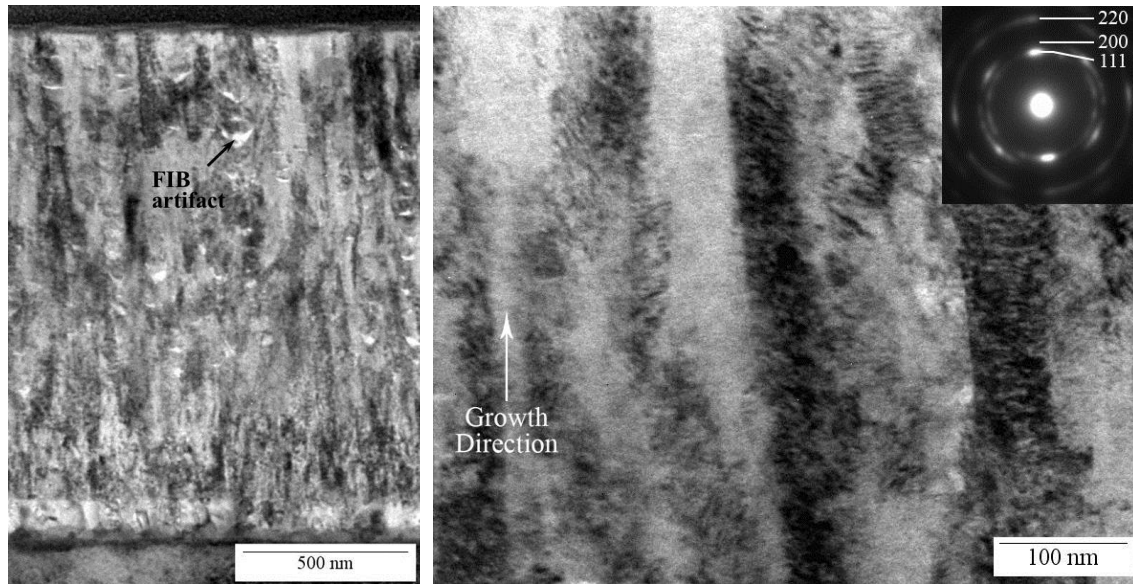


Figure 4.7 TEM micrograph (left) of the overall coating structure of TiN deposited with a -90 V substrate bias onto IN718. A high magnification image (right) from the top portion of the coating with a diffraction pattern in the upper right corner. Note this sample sustained a substantial amount of curtaining (V-shaped pores) during FIB sample preparation.

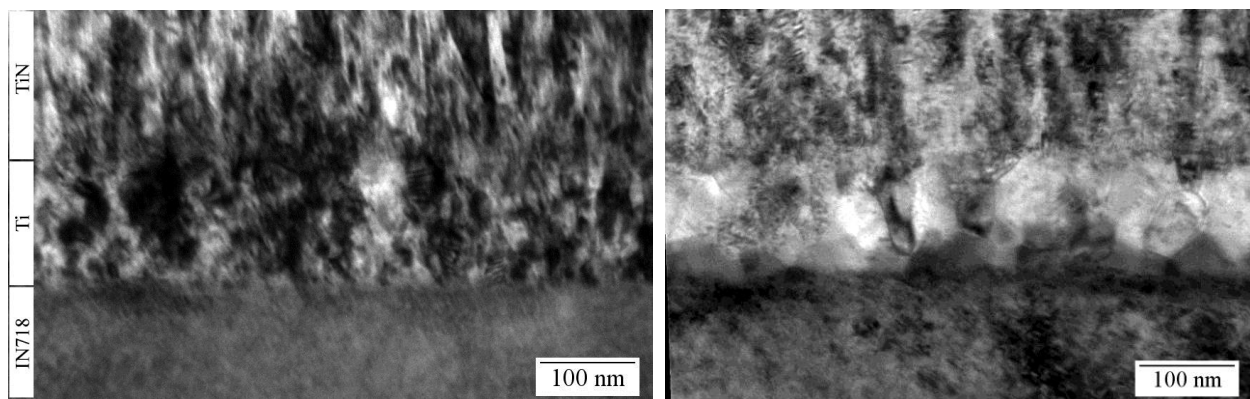


Figure 4.8 TEM micrographs of the coating interface between TiN, Ti, and IN718 deposited without bias (left) and with -90 V bias (right).

Some of the TEM observations are consistent with results found in XRD analysis. The XRD patterns attained for TiN deposited at several substrate biases on both IN718 and Ti-6Al-4V are shown in Figure 4.9. The preferred orientation at a floating bias is primarily (111) with some (200) planes, then at around -60 V bias, the preferred orientation is (220). At the maximum substrate bias of -90 V, the preferred orientation returns to (111) with some (220) orientation remaining, which agrees well with the diffraction patterns seen in TEM. Little difference was observed in crystallographic texture between the

two substrates other than the larger Ti peaks, presumably from the adhesion layer, observed for IN718. The position of the substrate on the sample holder relative to the sputter track may have led to different sputtering conditions resulting in a thicker adhesion layer, which could explain the differences in intensities. Figure 4.10 shows the calculated values of grain size (GS) with respect to substrate bias and working pressure. As observed in SEM and TEM, at low substrate biases the grains are quite long due to the fibrous structure making the GS appear larger in XRD. A minimum average GS of ~15 nm was calculated for -30 V biased coatings, while GS increased slightly with increasing substrate bias to ~23 nm for -90 V biased coatings. Again, the substrate had little effect on the results, although at floating bias Ti-6Al-4V seemed to have slightly larger GS for DOMS-deposited coatings, but the opposite was true for PMS-deposited coatings.

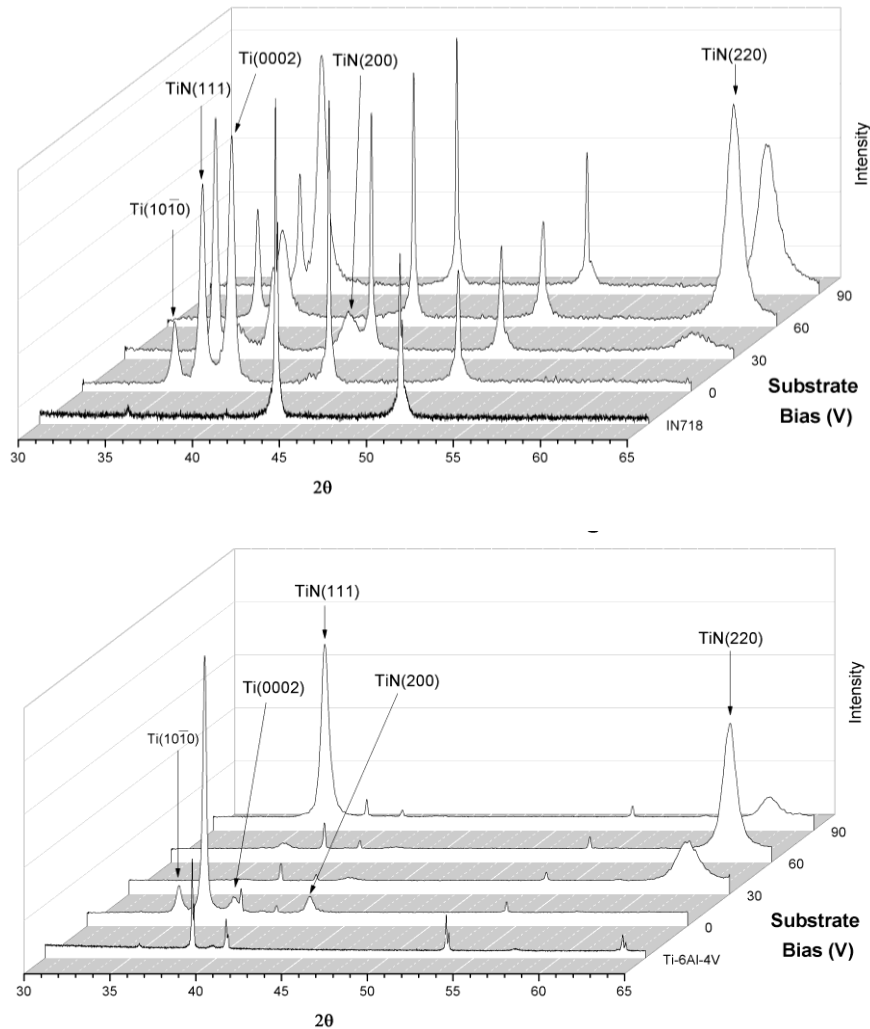


Figure 4.9 XRD patterns for TiN coatings with Ti adhesion layers deposited on IN718 (top) and Ti-6Al-4V (bottom). Variation in peak intensities for labeled planes is shown with respect to substrate bias.

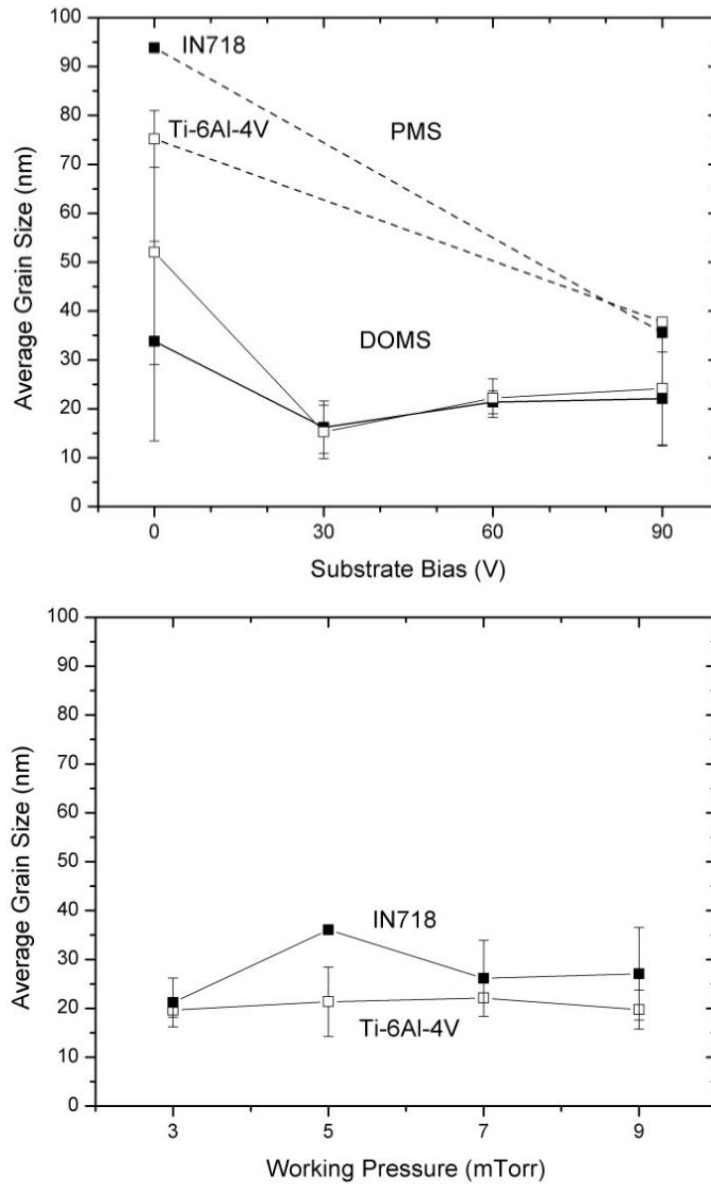


Figure 4.10 XRD grain size measurements of TiN coatings deposited with (top) DOMS and PMS using several negative substrate bias voltages and (bottom) DOMS-deposited coatings using various working pressures and a constant -60 V bias.

Working Pressure Effects

TiN coatings were deposited with DOMS using several working pressures to investigate working pressure effects on the structure and properties. XRD patterns in Figure 4.11 show a significant difference in texture between the two substrates, TiN deposited on IN718 having a predominantly (111) texture and

TiN deposited on Ti-6Al-4V having a (220) texture throughout all working pressures. This is opposite of what was seen in coatings deposited with varying substrate bias. It is suspected that a different sample configuration used may have caused a difference in plasma dynamics seen by the two substrates. This is also evident by the higher substrate peak intensities for the IN718 sample, suggesting that the thickness of the film was lower. Despite these differences, GS was virtually the same for all working pressures. TiN deposited onto IN718 had a slightly higher GS.

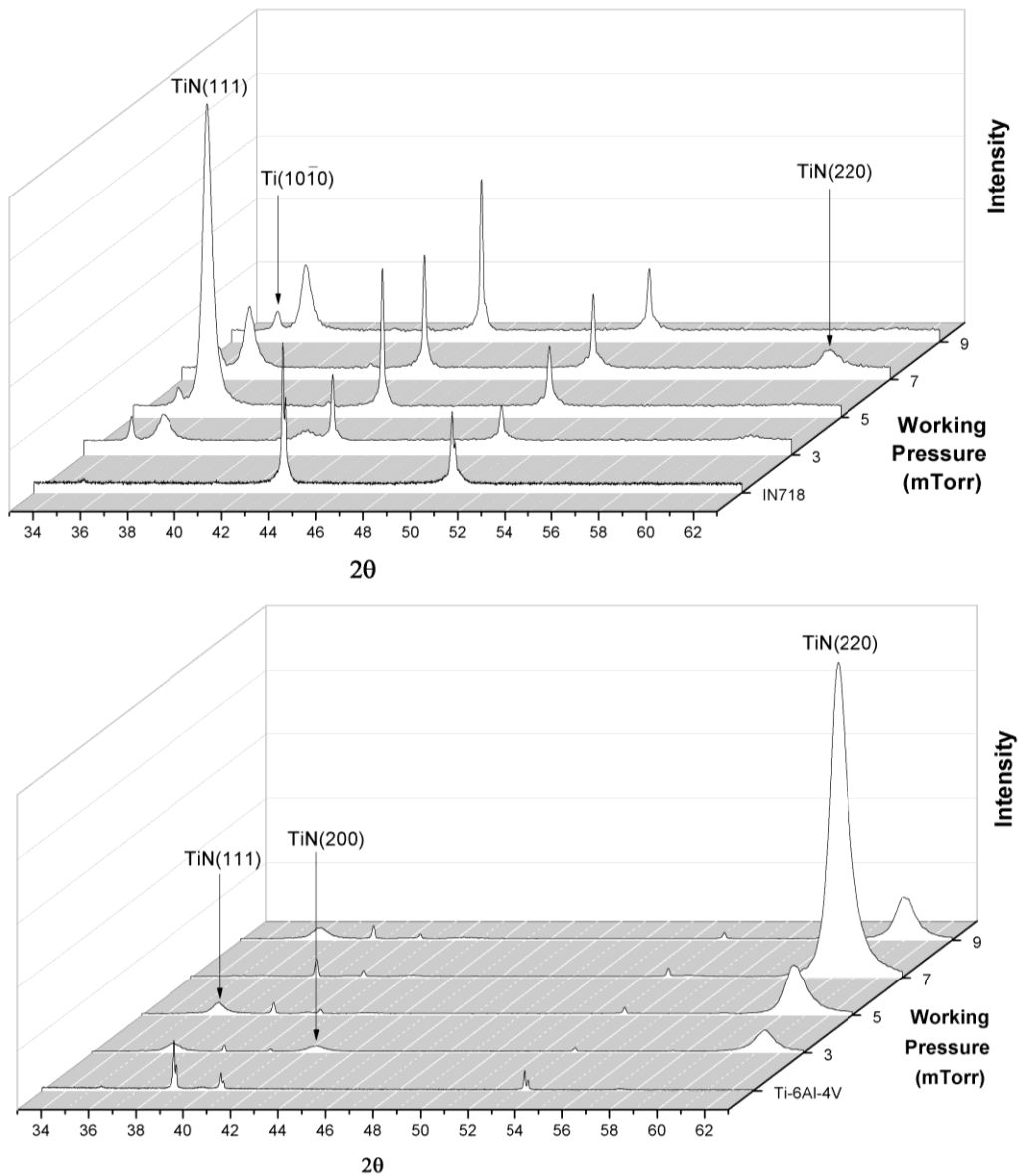


Figure 4.11 XRD patterns for DOMS-deposited TiN coatings with Ti adhesion layers onto IN718 (top) and Ti-6Al-4V (bottom). Variation in peak intensities for crystal planes is shown with respect to working pressure.

PMS Coatings

Depositions using PMS were conducted to compare the effects of deposition method on structure and properties. Two depositions were made using a floating and -90 V substrate bias. The respective microstructures are shown in Figure 4.12. Similar to DOMS-deposited coatings, the PMS-deposited coatings using floating bias had a fibrous Zone I microstructure, whereas the -90 V biased coating had wider, more truncated grains like that of a Zone T structure. XRD patterns in Figure 4.14 revealed both the floating and -90 V biased coatings had a (111) preferred orientation, perhaps stronger than those observed in the DOMS-deposited films since (200) and (220) intensities were not present. GS analysis showed a similar decreasing trend in GS with increasing substrate bias as seen in DOMS-deposited films (Figure 4.10).

Thick TiN coatings were deposited with DOMS and PMS to compare deposition rate and the feasibility of depositing thicker coatings. Coating thicknesses measured from the SEM images in Figure 4.13 were 5.2 μm and 4.2 μm for DOMS and PMS, respectively. These thicknesses correspond to calculated deposition rates of 2.08 $\mu\text{m}/\text{h}$ and 1.68 $\mu\text{m}/\text{h}$ for DOMS and PMS, respectively.

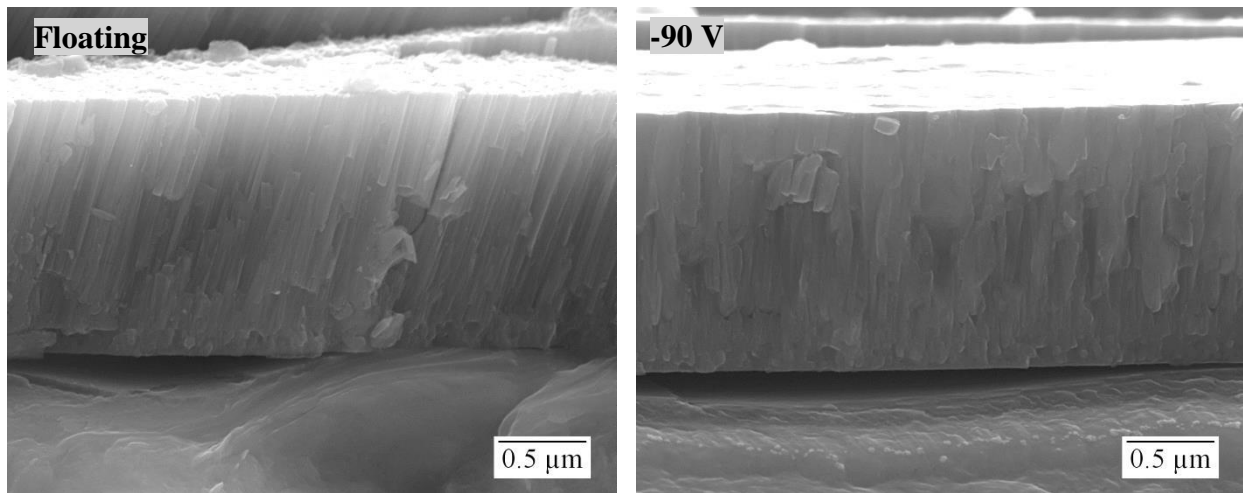


Figure 4.12 SEM images of fractured cross sections of TiN deposited at different substrate biases onto Ti-6Al-4V using PMS.

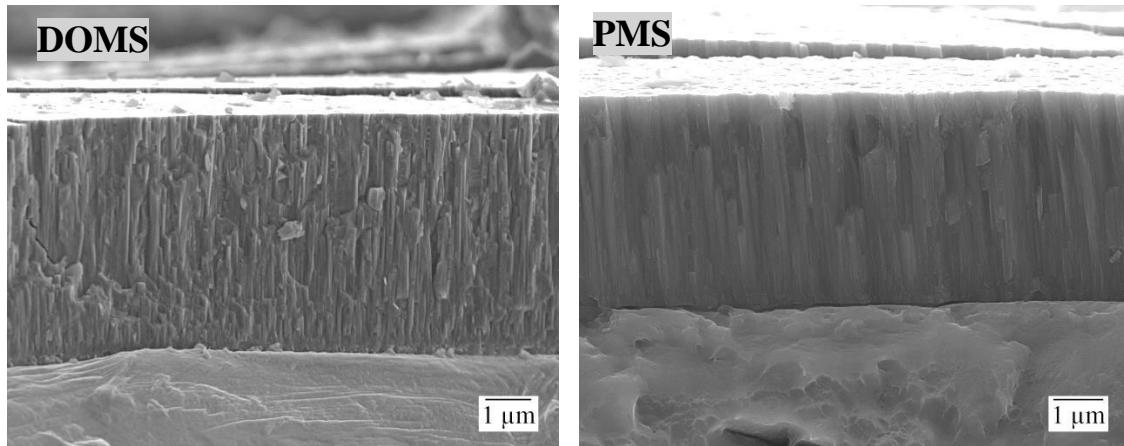


Figure 4.13 Fractured cross sections of TiN coatings deposited on Ti-6Al-4V using DOMS (left) and PMS (right) with similar deposition conditions (-60 V bias, 7 mTorr, 2.5 hrs).

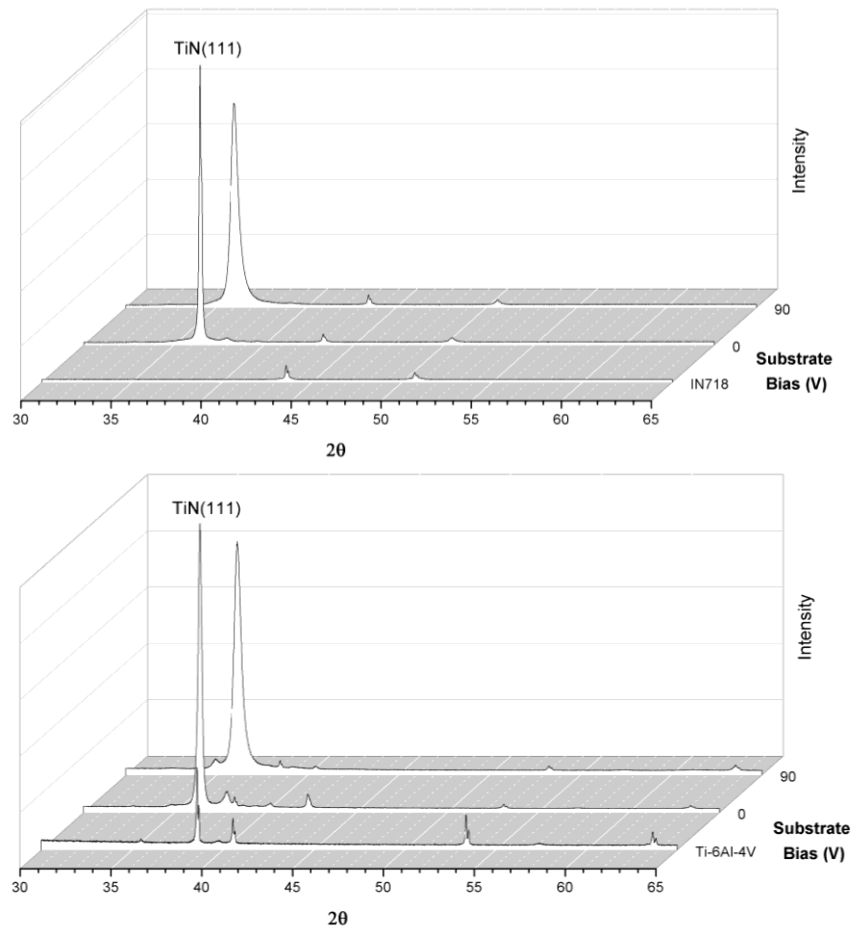


Figure 4.14 XRD patterns for TiN coatings deposited on IN718 (top) and Ti-6Al-4V (bottom) using PMS with -90 V applied substrate bias and without bias. Variations in peak intensities for labeled planes are shown with respect to working pressure.

4.2.2 Residual Stress

Residual stresses were measured for TiN deposited at several substrate biases. Figure 4.15 shows that residual stress becomes more compressive with increasing substrate bias. An apparent maximum compressive stress of about -3.7 GPa and -2.8 GPa was reached at -60 V bias for IN718 and Ti-6Al-4V, respectively.

There are two components that contribute to the total residual stress, namely, intrinsic stresses caused by strains in the lattice from growth defects and thermal stresses caused by mismatch between the coating CTE (α_f) and substrate CTE (α_s) as a result of cooling from the deposition temperature. The substrate temperature (T_s) was measured immediately after the deposition. The highest observed temperature was for DOMS using -60 V substrate bias. This value was used for calculating $\Delta T = T_s - 25^\circ \text{C}$ along with an average modulus for the film, $E_f = 410 \text{ GPa}$, and Poisson's ratio of the film ($\nu_f = 0.25$). Using CTEs in Table 4.1, the thermal stress (σ_{th}) was calculated for several substrates using Equation (4.1) [70].

$$\sigma_{th} = (\alpha_f - \alpha_s) \frac{E_f}{1 - \nu_f} \Delta T \quad (4.1)$$

The results show that σ_{th} is $\sim 1.4 \text{ GPa}$ more compressive for IN718, which agrees well with the total residual stress measurements determined by XRD. Furthermore, a tensile stress is observed for Si, which may explain why most coatings delaminated after depositing on Si.

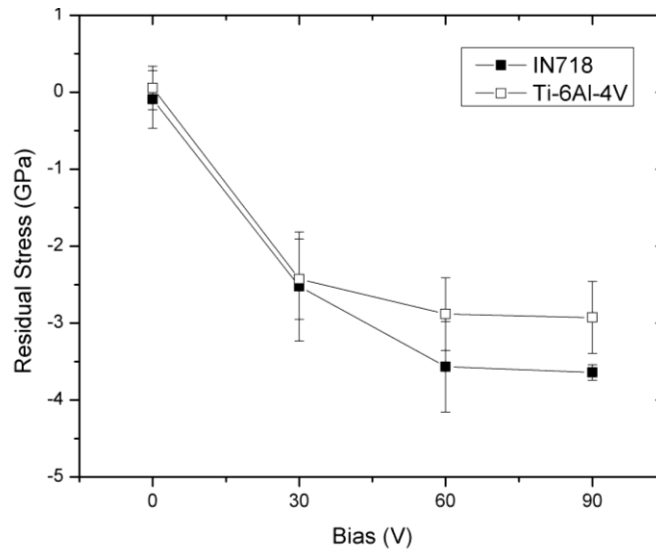


Figure 4.15 Effect of apply negative substrate bias on the residual stress in DOMS-deposited TiN films. Values were calculated from the linear fits of $\sin^2\psi$ graphs produced using measured peak shifts attained from GAXRD at several glancing angles (6° , 10° , and 14°).

Table 4.1 Thermal residual stresses calculated using the CTE* for the substrates and TiN.

Substrate Bias (V)	E (GPa)	ΔT (°C)	σ_{th} (GPa) IN718	σ_{th} (GPa) Ti-6Al-4V	σ_{th} (GPa) SS304	σ_{th} (GPa) Si
-60	410	460	-1.4	-0.03	-2.2	1.6

*CTE's used for calculations [71]: TiN= $9.4 \times 10^{-6} \text{ K}^{-1}$, IN718= $15.3 \times 10^{-6} \text{ K}^{-1}$,
Ti-6Al-4V= $9.54 \times 10^{-6} \text{ K}^{-1}$, 304SS= $18.7 \times 10^{-6} \text{ K}^{-1}$, Si= $2.6 \times 10^{-6} \text{ K}^{-1}$

4.2.3 Hardness and Elastic Modulus

Evaluation of hardness and modulus were done with nanoindentation. Hardness increased gradually with increasing substrate bias, as shown in Figure 4.16. The effective modulus was calculated using $E^* = E/(1-\nu^2)$ from Musil [64] and increased with increasing substrate bias, reaching a maximum of 428 GPa at -60 V then decreased at -90 V. Although modulus decreased at -90 V, the hardness continued to be relatively high. These results coincide with the Hall-Petch relationship as it was observed that GS decreased when substrate bias was increased and hardness increased with decreasing GS. The slight increase in GS for -90 V biased coatings may explain the slight decrease in hardness. Also noted was that there seems to be a relationship between the texture and modulus, which is expected as the TiN modulus is very anisotropic [72].

The H/E^* ratios and resistance to plastic deformation, H^3/E^2 , were plotted for coatings deposited with substrate biases of floating to -90 V. The maximum $H/E^* = 0.09$ was achieved with a -90 V bias with DOMS, however, the maximum $H^3/E^2 = 0.26$ was achieved with PMS and a -90 V bias.

Work pressure had little effect on hardness or modulus. Figure 4.17 shows the hardness and effective modulus for coatings deposited with working pressures of 3-9 mTorr. While there might be a slight decrease in modulus with increasing pressure, but it is difficult to tell due to the overlapping errors in measurement and variation between substrates. A larger range of working pressures would prove valuable for attaining a more defined effect. It is important to note that despite the very different textures, the changes in hardness and GS were negligible.

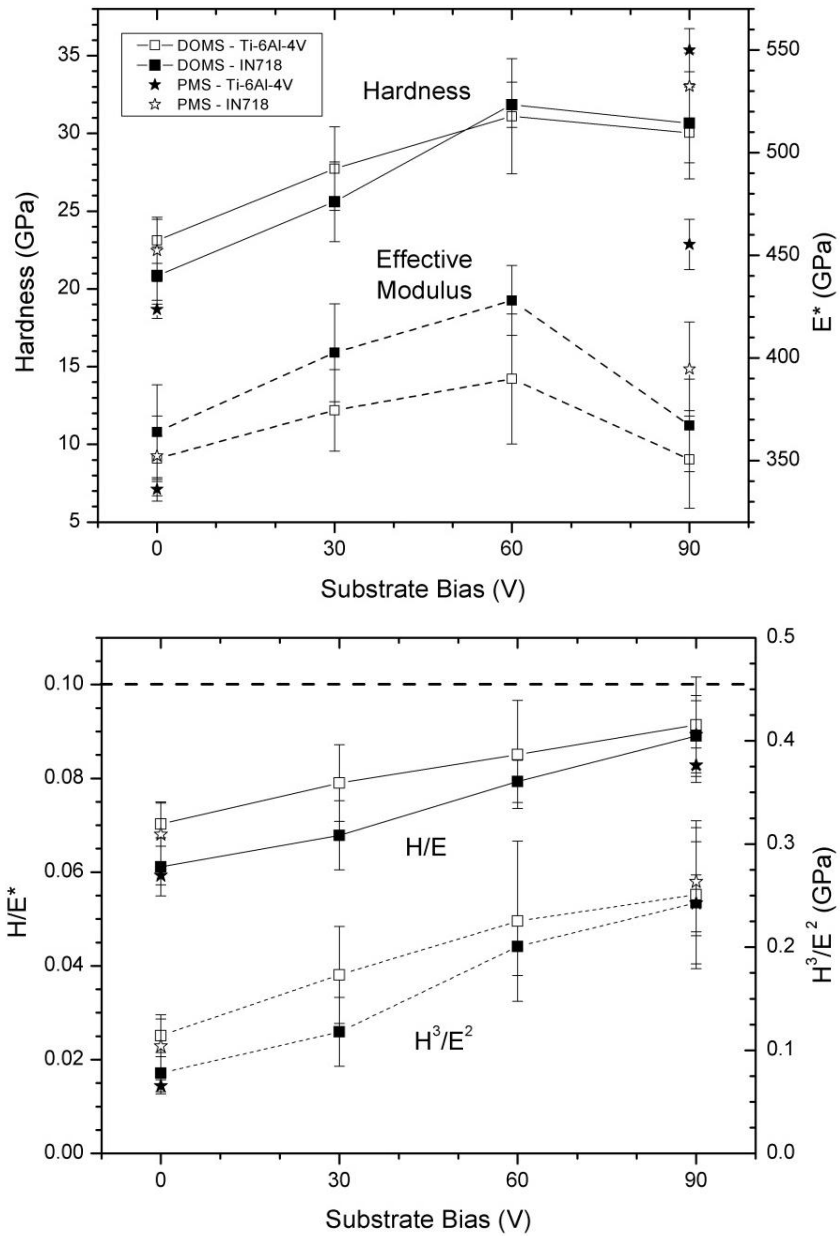


Figure 4.16 Nanoindentation results showing hardness and effective modulus of TiN coatings deposited on Ti-6Al-4V and IN718 (top) and calculated H/E^* and H^3/E^2 ratios (bottom) for several negative substrate biases. The dashed line indicates the desired H/E^* ratio for ultra-high performance coatings.

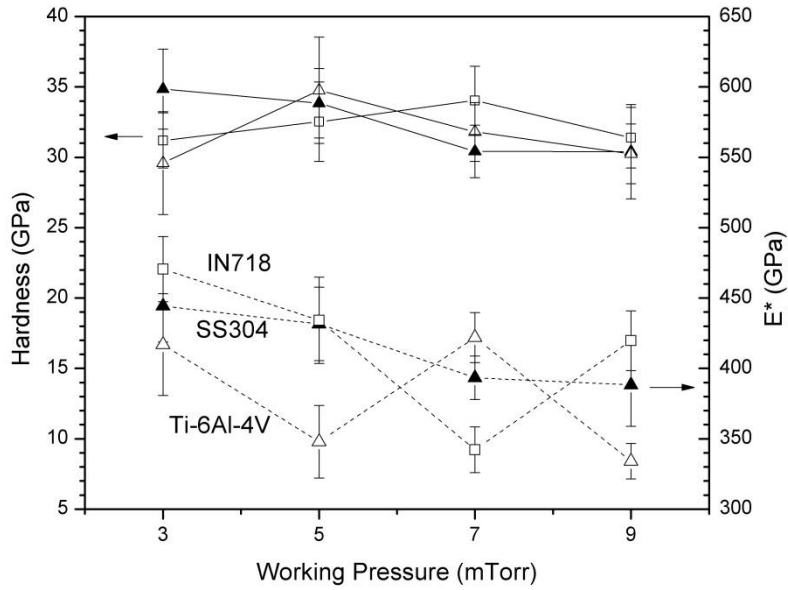


Figure 4.17 Nanohardness of TiN coatings deposited with DOMS on different substrates with various working pressures and using a -60 V substrate bias for all samples.

4.2.4 Adhesion and Wear

Two techniques were used for analyzing the adhesion between deposited TiN coatings and the substrates. Substrate bias, substrate alloy, and deposition method were the three variables studied to see how they affect adhesion.

The first technique used for evaluating adhesion was scratch testing, which showed that adhesion strength was greatly affected by substrate bias for both DOMS and PMS-deposited TiN coatings as well as the substrate material. Table 4.2 shows critical failure loads for several coatings deposited onto IN718 with varying substrate biases. Also included in Table 4.2 are critical loads for TiN coatings deposited with DOMS on SS304, Ti-6Al-4V, and IN718 with a -90 V bias. The critical loads are defined as follows: L_{C1} is the load at first failure, L_{C2} is the load at continuous failure, and L_{C3} is the load at first delamination within the track. The L_{C1} modes of failure were primarily cohesive, meaning that the coating failed by cracking or buckling from the applied load before any failure occurred at the coating-substrate interface. An exception was for coatings deposited with floating bias, where some delamination was observed inside and outside of the track, indicating poor adhesion. Optical images of the scratch tests can be seen in Figure 4.18 and Figure 4.19.

With increasing substrate bias, L_{C2} and L_{C3} increased, while L_{C1} had no distinct trend. The PMS-deposited coatings generally had higher critical loads when compared to DOMS coatings. The highest L_{C1}

of 6.5 N was observed for DOMS deposited TiN onto SS304, which was the only substrate deposited on that did not have an L_{C3} . Coatings deposited on IN718 tended to gradually delaminate after L_{C3} , however delamination was abrupt and complete for coatings deposited on Ti-6Al-4V.

Table 4.2 Critical loads for scratch tested TiN coatings deposited with DOMS and PMS. Tests were conducted using a IN718 substrate for those deposited with different substrate biases.

Bias (V)	Critical Loads (N)			Substrate	Critical Loads (N)		
	L_{C1}	L_{C2}	L_{C3}		L_{C1}	L_{C2}	L_{C3}
Floating	1.8, 3.2*	6.8, 8.2*	2.7, 6.4*	IN718	2.5	10.4	10.9
-30	4.4	8.8	9.4	Ti-6Al-4V	6.0	7.9	9.0
-60	3.0	9.3	11.7	SS304	6.5	11.0	-
-90	2.5, 5.2*	10.4, 12.2*	10.9, 13.2*				

*PMS-deposited TiN

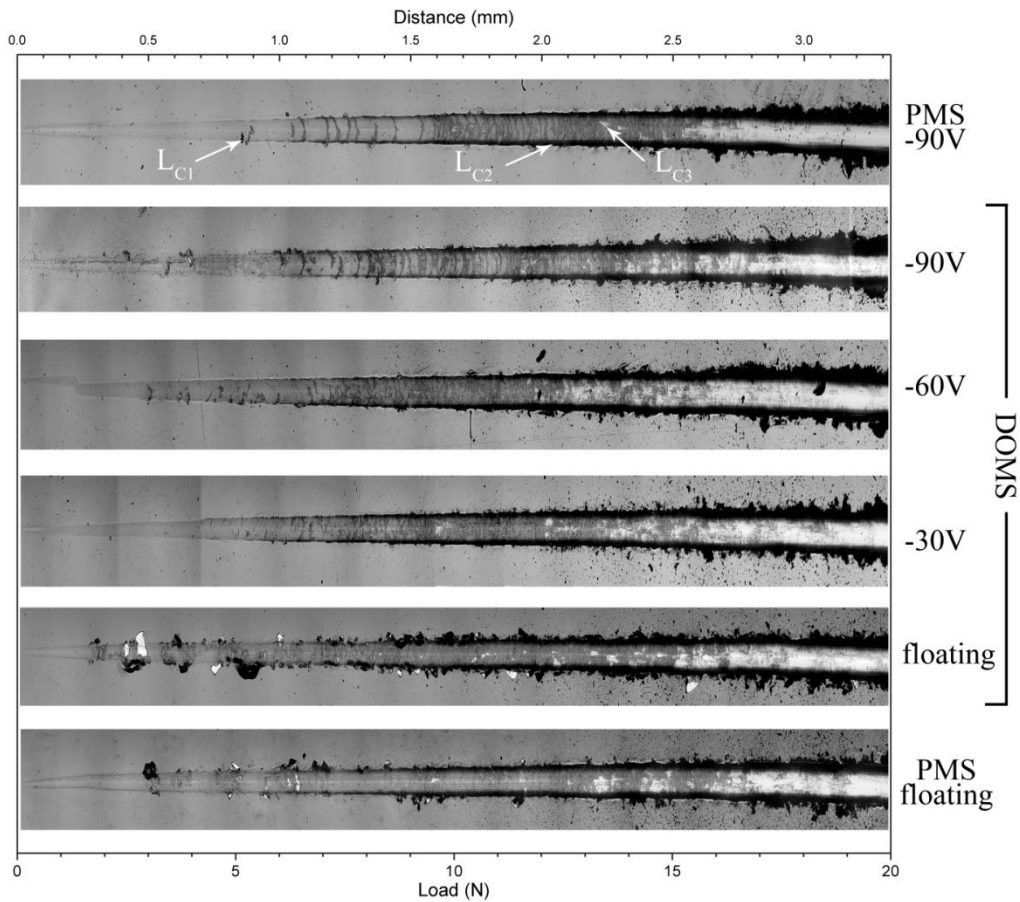


Figure 4.18 Scratch tests of PMS and DOMS-deposited TiN coatings on IN718 with several substrate biases. Examples of three critical loads are shown for the -90 V biased PMS coating.

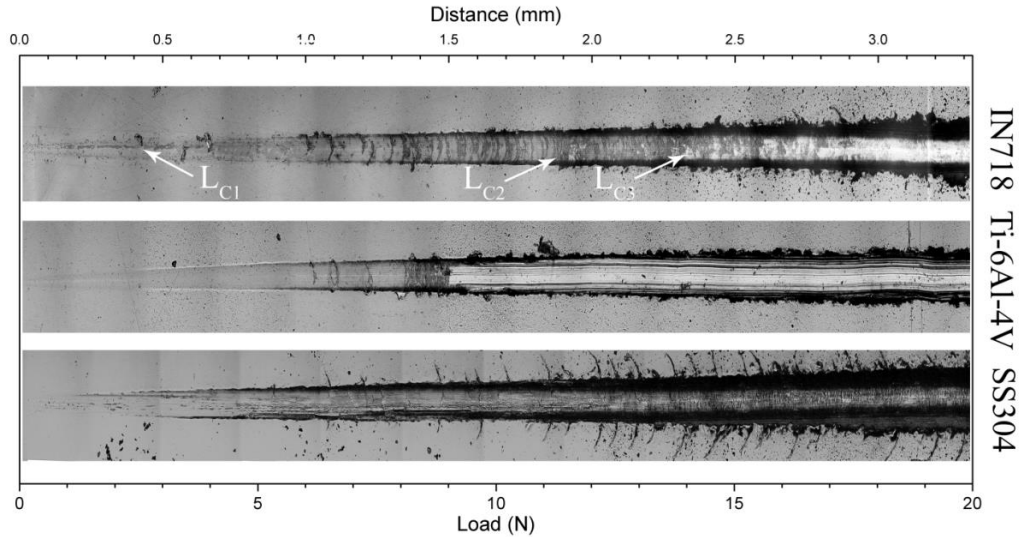


Figure 4.19 Scratch tests of DOMS-deposited TiN coatings showing the effects of substrate on adhesion.

Figure 4.20 shows the indent results for coatings deposited with several deposition techniques onto IN718 and Ti-6Al-4V with floating bias. MPPMS and PMS showed the best adhesion strength with little to no delamination, giving values of HF2 and HF1 for IN718 and Ti-6Al-4V, respectively. The worst adhesion was observed for DOMS-deposited coatings that had much more delamination, though they were still considered to have good adhesion based on values HF4 and HF3 for IN718 and Ti-6Al-4V, respectively. The second method for evaluating adhesion was Rockwell C indentation tests. Figure 4.21 shows SEM images of indents on the surface of coatings deposited using DOMS and several substrate biases. It was observed that delamination is virtually eliminated with applied negative substrate bias ≥ 60 V. There was good agreement between Rockwell C indentation tests and scratch tests showing that adhesion was poorest for coatings deposited with floating bias. The remaining coatings had good adhesion with $HF \leq 4$. The worst adhesion was for TiN deposited on SS304 with DOMS and floating bias. Massive delamination occurred outside and within the indent. However, for the remaining samples deposited on 304SS with the different substrate biases the adhesion strength improved. Adhesion seemed to be greater than coatings deposited on IN718 and Ti-6Al-4V. However, it is more likely this is a mechanical response effect as will be discussed later in this thesis. For coatings deposited with floating bias, coatings deposited on Ti-6Al-4V had the best adhesion, followed by IN718 based on the relative areas of delamination and cracking. Also noted was the fewer number of cracks observed in the -90 V biased PMS samples compared to DOMS. This may also have been a mechanical response effect from the substrate. Additional TiN coatings were deposited with MPPMS and evaluated to compare the three deposition techniques.

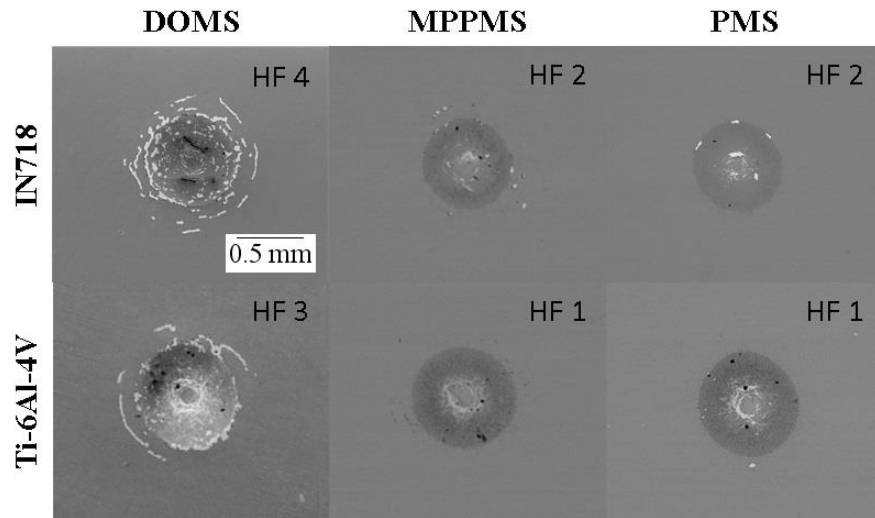


Figure 4.20 SEM images of Rockwell-C adhesion tests of TiN coatings deposited with several deposition methods using floating bias. HF adhesion grade indicated in each image.

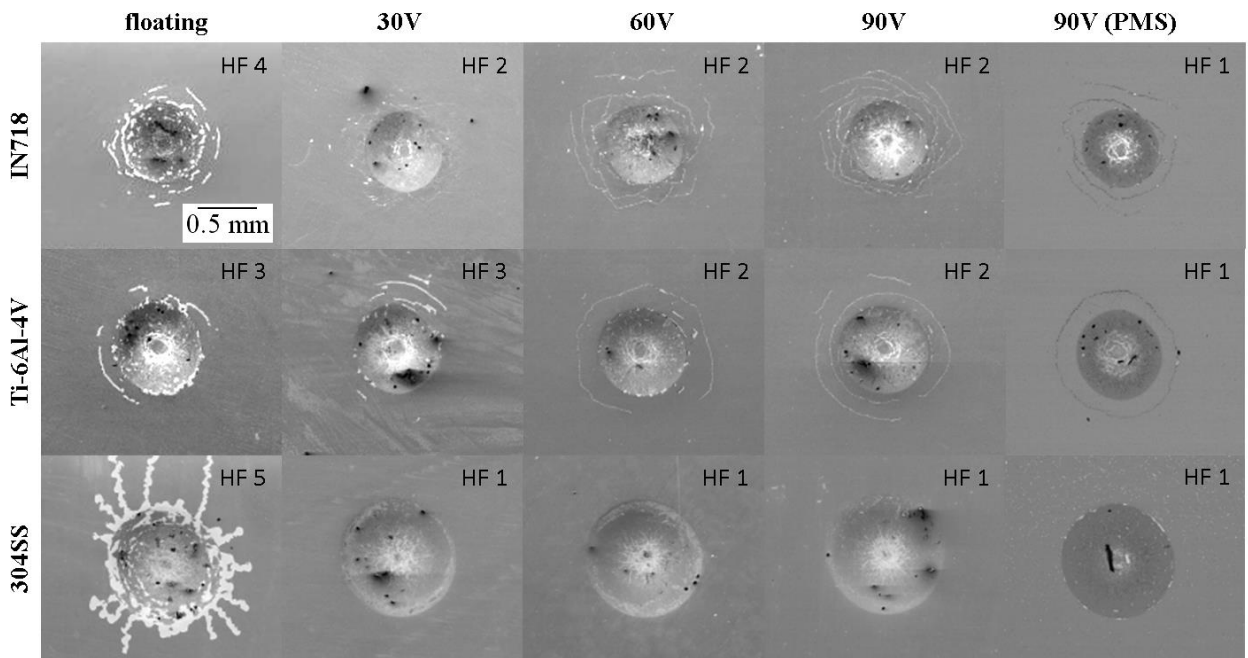


Figure 4.21 Rockwell-C indentation tests for TiN coatings deposited with DOMS and PMS with varying substrate biases (labeled on top) and substrates (labeled on leftside).

Ball-on-disk wear tests were conducted to evaluate the effects of substrate bias and deposition technique, but also in an attempt to correlate H^3/E^2 values with wear rate. Wear rates and coefficients of friction (COF) as functions of substrate bias are summarized in Figure 4.22. Wear rates were shown to decrease with increasing substrate bias to a minimum value of $1.04 \times 10^{-6} \text{ mm}^3/\text{Nm}$ using DOMS, while COF slightly increased. While DOMS-deposited coatings may have a slightly lower wear rate, the COF was lower for those deposited with PMS. Wear rate versus H^3/E^2 (Figure 4.22) shows that wear rate decreases with increasing H^3/E^2 , although there is a substantial amount of error overlap to say it is a linear relationship.

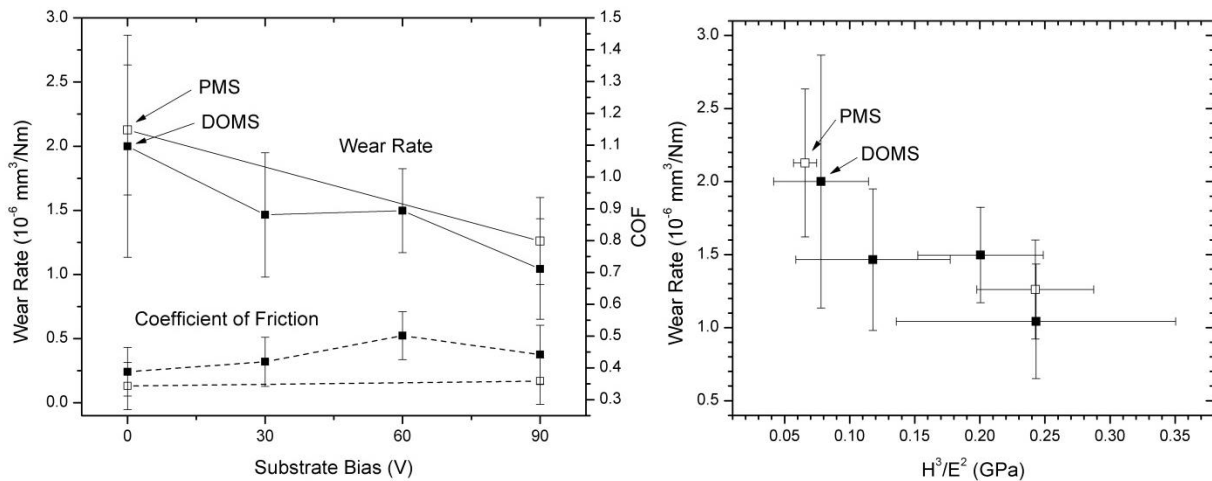


Figure 4.22 Calculated wear rate and COF for TiN coatings deposited on IN718 at several substrate biases with DOMS and PMS (left). Wear rate graphed as a function of H^3/E^2 from hardness results, showing a decreasing trend in wear rate with increasing resistance to plastic deformation.

4.3 $\text{Ti}_{1-x}\text{Al}_x\text{N}$

The following subsections describe the results found through the characterization of $\text{Ti}_{1-x}\text{Al}_x\text{N}$ coatings deposited with MPPMS and PMS using two different target compositions, 50Ti-50Al and 30Ti-70Al. All depositions were done using floating substrate bias.

4.3.1 Microstructure and Crystallographic Texture

The microstructure was first characterized using SEM to examine the differences between MPPMS and PMS-deposited $\text{Ti}_{1-x}\text{Al}_x\text{N}$. Figure 4.23 shows fracture surfaces for cleaved cross-sections of $\text{Ti}_{1-x}\text{Al}_x\text{N}$ deposited on Ti-6Al-4V. Most of the coatings appear to take on a lower Zone T structure. Grains appear to be finer in the MPPMS-deposited coatings. The fracture surface of the MPPMS-deposited coating with the 30Ti-70Al target appears virtually featureless and TEM was needed to determine the true grain structure. Deposition rate for MPPMS-deposited coatings was slower for both

target compositions. The thicknesses for coatings deposited with the 50Ti-50Al target, including the adhesion layer, are 1.38 μm and 1.49 μm for MPPMS and PMS, respectively. The thicknesses for coatings deposited with the 30Ti-70Al target are 1.49 μm and 1.98 μm for MPPMS and PMS, respectively. The Ti-adhesion layer also appeared thinner for MPPMS with a thickness of approximately 50 nm compared to 150 nm for PMS. This is important to note when discussing adhesion results as less buffer is available to accommodate strains produced by stresses at the interface through elastic and plastic deformation in the Ti layer.

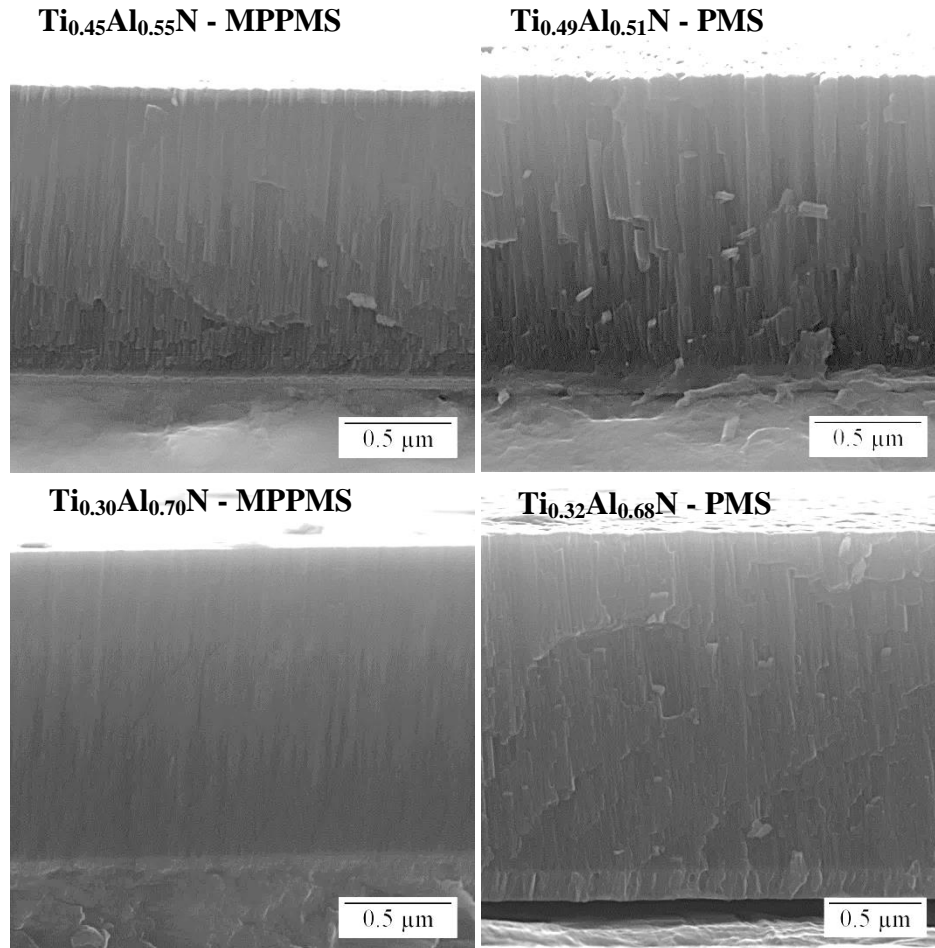


Figure 4.23 SEM images of $\text{Ti}_{1-x}\text{Al}_x\text{N}$ coatings deposited with MPPMS and PMS using 50Ti-50Al (top) and 30Ti-70Al targets (bottom) onto Ti-6Al-4V. Fracture surfaces reveal the 50-100 nm Ti adhesion layer below the $\text{Ti}_{1-x}\text{Al}_x\text{N}$ coating.

Further investigation of microstructure and texture was conducted with TEM for MPPMS-deposited samples. Figure 4.24 shows a cross-sectional view of $\text{Ti}_{0.45}\text{Al}_{0.55}\text{N}$ deposited on IN718. Dark areas of diffraction contrast and bending within the grains can be seen through the thickness of the coating. As mentioned in TEM images for TiN coatings, contrast sources include differently

oriented grains, growth defects, and bending within grains. The diffraction pattern reveals a polycrystalline structure with a slight texture as noted by the concentrated spots normal to the substrate surface, these correspond to planes oriented parallel to the substrate surface. The observed reflections signify a slight (200) and (111) preferred texture. Also noted was intensity found between the (111) and (200) reflections, which most closely match the d-spacing for Ti-(10 $\bar{1}$ 0) planes. The higher magnification image in Figure 4.24 shows neighboring columnar grains that vary between 10 to 40 nm wide. The variation in contrast within one grain shows bending and/or defects within the lattice. Through the thickness, the columnar grains are interrupted by smaller grains or the nucleation and growth of new columnar grains. The lack of voids supports the conclusion that the coating is very dense.

Figure 4.25 shows a BF image for an MPPMS-deposited Ti_{0.30}Al_{0.70}N coating onto IN718. Toward the bottom of the image on the left, bend contours can be seen for IN718. The contours appeared to form around the center of the sample, which is also the thinnest section allowing for more relaxation/bending caused by residual stresses. Substantially less diffraction contrast is observed within the grains compared to the Ti_{0.45}Al_{0.55} coating suggesting fewer defects and larger average grain size. This made grain boundaries less discernable; however, the high magnification image on the right in Figure 4.25 reveals similar columnar grains to those that were observed in the Ti_{0.45}Al_{0.55} coating. The diffraction pattern shows the coating is heavily textured with cubic-(111), hex-(0002), and hex-(1 $\bar{1}$ 00) planes oriented parallel to the substrate surface. Higher magnification images revealed a dense structure without any significant voids.

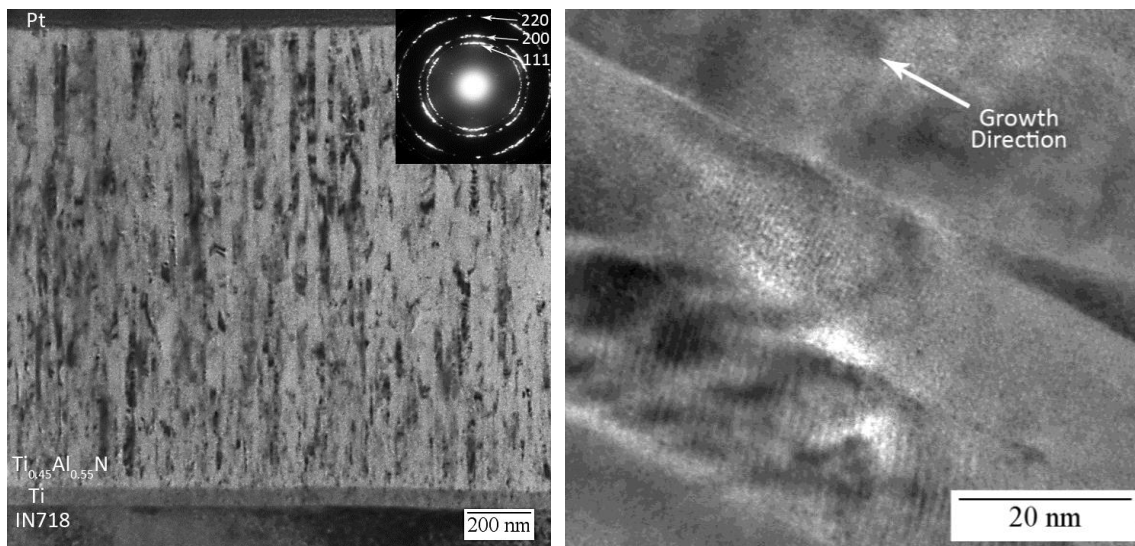


Figure 4.24 BF TEM micrographs showing a cross-section of Ti_{0.45}Al_{0.55}N deposited with MPPMS onto IN718 using floating bias (left). An SADP for the coating is also shown with labeled diffraction rings in regard to the cubic phase. On the right is a high magnification image from the middle portion of the coating.

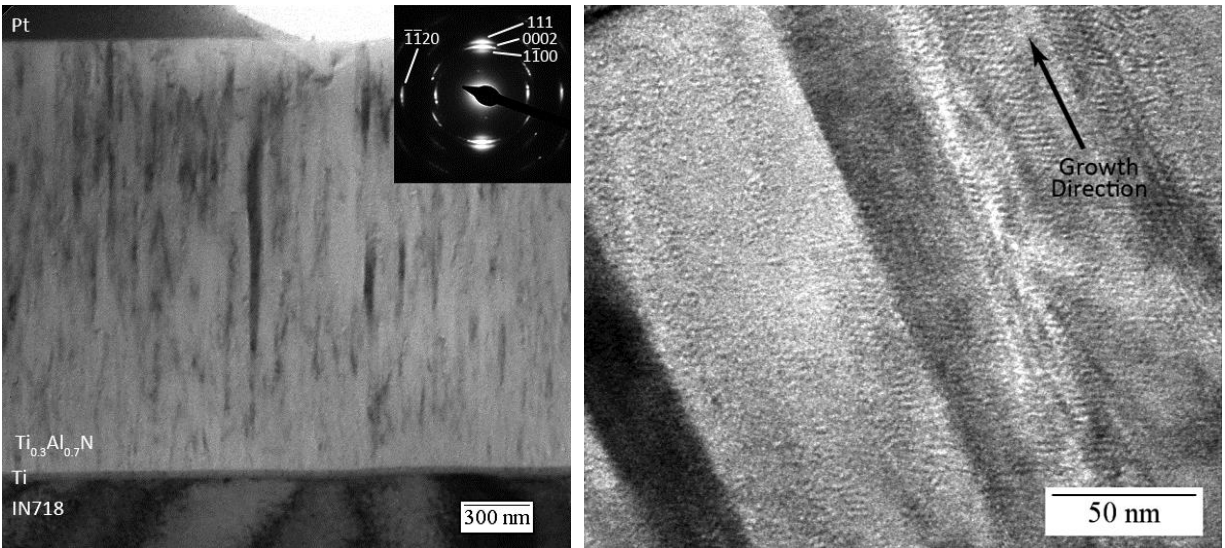


Figure 4.25 BF TEM micrographs showing a cross-section of $\text{Ti}_{0.45}\text{Al}_{0.55}\text{N}$ deposited with MPPMS onto IN718 using floating bias (left). An SADP for the coating is also shown with labeled diffraction rings for the cubic phase. On the right is a high magnification image from the top of the coating.

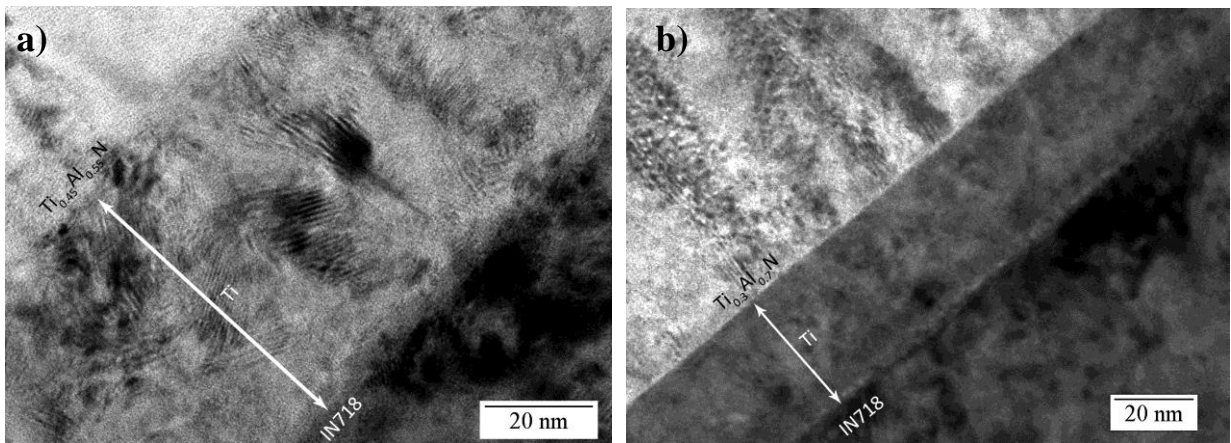


Figure 4.26 BF TEM image of Ti adhesion layer at the coating-substrate interface for MPPMS-deposited coatings using targets with compositions (a) 50Ti-50Al and (b) 30Ti-70Al.

Additional phase and grain size analysis for $Ti_{1-x}Al_xN$ coatings were conducted with XRD. The XRD patterns in Figure 4.27 show that for coatings deposited with the 50Ti-50Al target, the cubic phase is dominant. The PMS-deposited coating is mostly (111) oriented, while the MPPMS-deposited coating has intensity from both (111) and (200) planes. Figure 4.27 also shows that, for higher Al fraction coatings, the intensity from the hexagonal wurtzite phase (AlN) is more predominant compared to intensity from the cubic phase (TiN). For both MPPMS and PMS, the wurtzite phase is mostly (0002) oriented, and the only intensity observed from the cubic phase was in the MPPMS coating with a (111) orientation. Also noted, the Ti peaks from the adhesion layer were only observed with XRD for the PMS-deposited coatings, likely due to higher thickness in PMS samples. Figure 4.28 shows calculated GS for all $Ti_{1-x}Al_xN$ coatings using the XRD patterns in Figure 4.27. PMS-deposited coatings using the 50Ti-50Al target had a substantially higher average GS (~180 nm) when compared to the MPPMS-deposited coatings (~40 nm). Coatings deposited with the 30Ti-70Al target had a lower GS than coatings deposited with the 50Ti-50Al target, but did not vary significantly between MPPMS and PMS-deposited coatings.

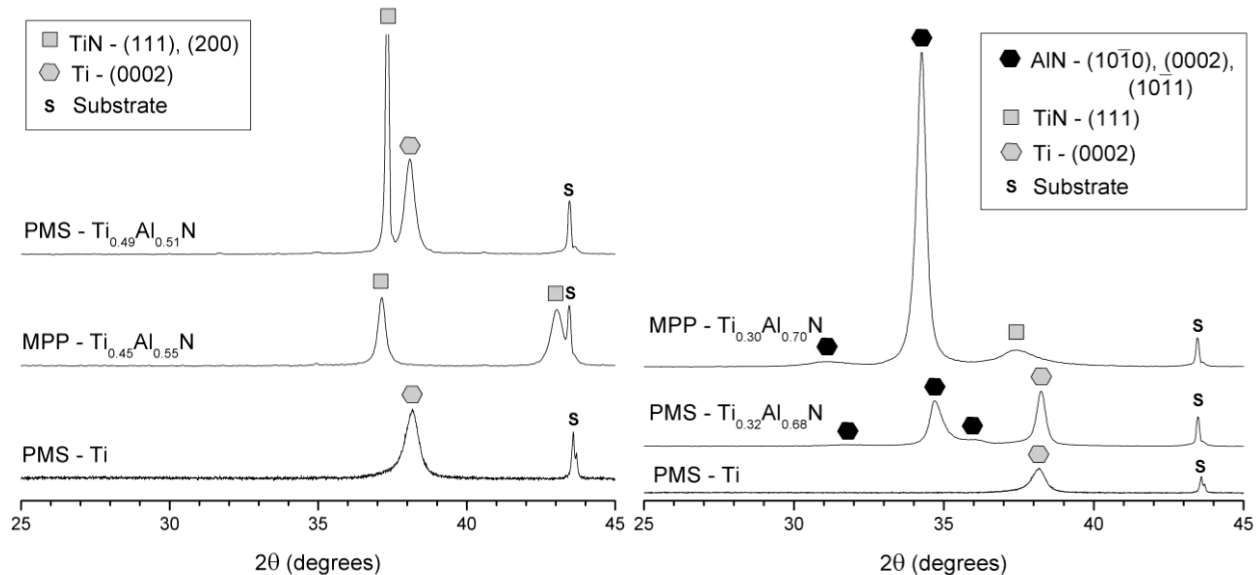


Figure 4.27 XRD patterns for $Ti_{1-x}Al_xN$ coatings deposited with MPPMS and PMS on SS304 using a 50Ti-50Al target (left) and a 30Ti-70Al target (right). Also included is the spectrum gathered for a pure Ti coating deposited with PMS for identifying the adhesion layer.

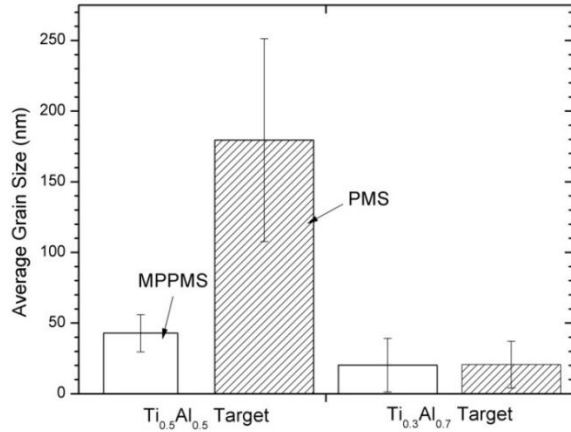


Figure 4.28 Calculated GS from XRD patterns of MPPMS and PMS-deposited $Ti_{1-x}Al_xN$ coatings.

4.3.2 Hardness and Composition

The compositions of the deposited coatings were analyzed by EDS to determine the Al concentration, x , in the $Ti_{1-x}Al_xN$ coatings deposited with two different target compositions, 50Ti-50Al and 30Ti-70Al. Figure 4.29 shows the MPPMS-deposited coatings tended to have higher Al/Ti ratios than PMS for both target compositions. It is important to note that the order in which MPPMS and PMS coatings were deposited was reversed to avoid target compositional changes that may arise from preferential sputtering during the previous deposition.

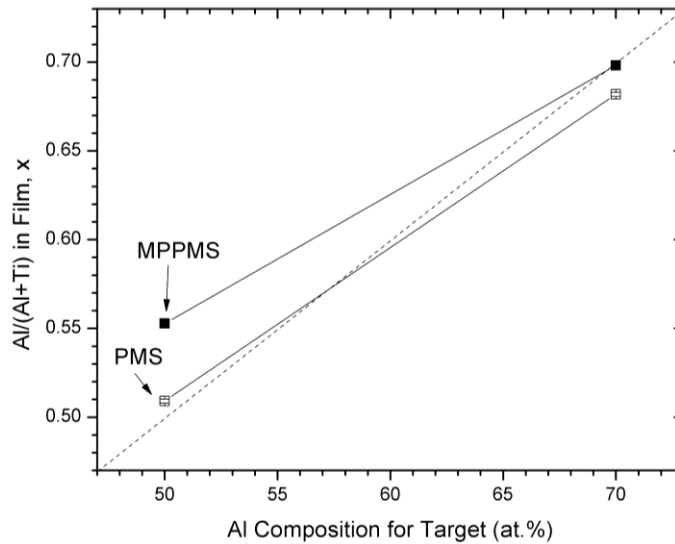


Figure 4.29 Compositional measurements using EDS for $Ti_{1-x}Al_xN$ coatings deposited with MPPMS and PMS using 50Ti-50Al and 30Ti-70Al targets. Nitrogen has been excluded due to limitations of EDS for accurately measuring light elements. A dashed line represents equal target/coating Al ratios.

Nanoindentation hardness appears to be strongly affected by composition and the type of power supply used to deposit the coatings. Unlike TiN, which produces a gold color at a nitrogen composition close to 50 at.%, $Ti_{1-x}Al_xN$ is more of an eggplant purple. However, it is difficult to discern it from off-compositional colors, like grayish purple and dark gray. Thus, the nitrogen composition was optimized using hardness. Figure 4.30 shows the hardness beginning to plateau at around 25% $N_2/(N_2+Ar)$. It also shows that film hardness decreases with increasing N flow percentage. Eventually, target poisoning will become an issue at higher N flow without any substantial benefits in hardness. Therefore, a 25% $N_2/(N_2+Ar)$ was chosen for all subsequent depositions.

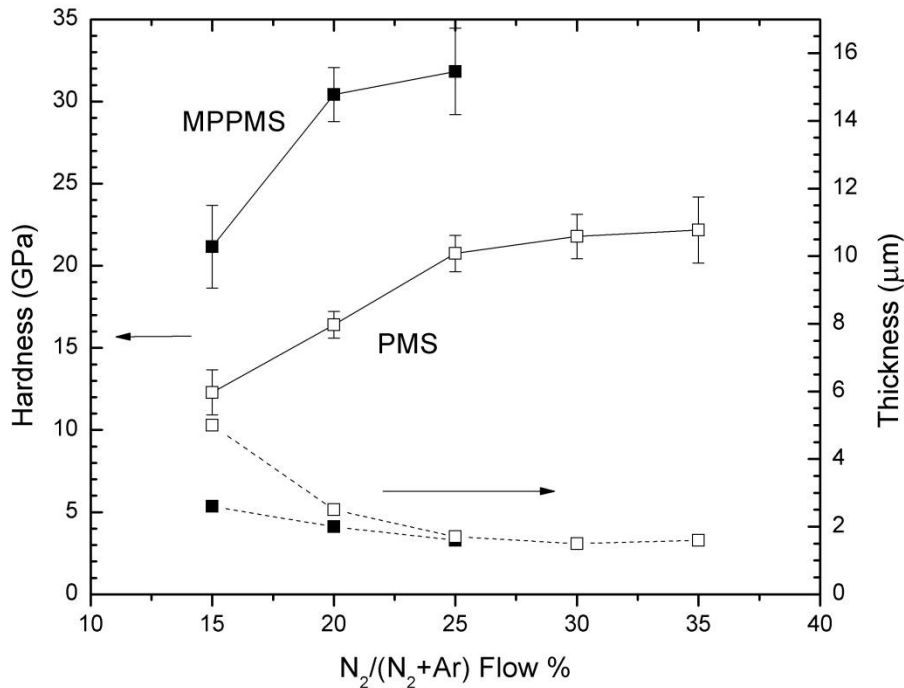


Figure 4.30 Hardness and thickness of $Ti_{1-x}Al_xN$ coatings deposited with MPPMS and PMS on SS304 using the 50Ti-50Al target with several different nitrogen flow rates. Coatings were deposited for 30 minutes.

The hardnesses and moduli for coatings deposited with MPPMS and PMS using two different target compositions are shown in Figure 4.31. The MPPMS-deposited coatings displayed significantly higher hardness, especially for the 50Ti-50Al target with mean values of 35.4 GPa and 20.7 GPa for MPPMS and PMS respectively. GS results from XRD showed that GS was much lower for the MPPMS-deposited coatings (~40 nm) compared to PMS-deposited coatings (~180 nm), which may explain the increase in hardness. Using values in Figure 4.31, H/E^* and H^3/E^2 were calculated and are shown Figure 4.32. The highest values were recorded for MPPMS-deposited coatings, with H/E^* values exceeding 0.1 for both compositions.

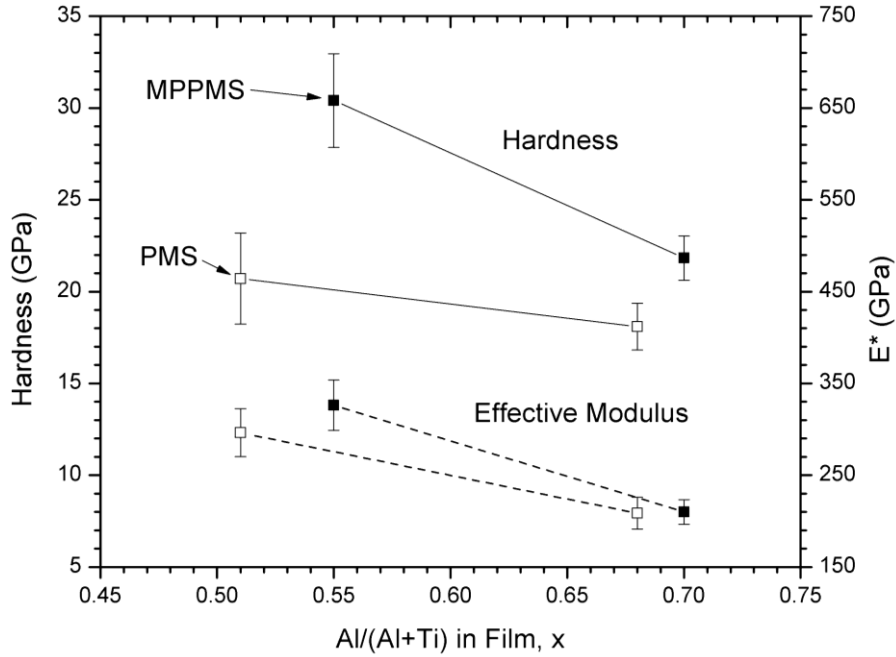


Figure 4.31 Hardness and modulus of $Ti_{1-x}Al_xN$ coatings deposited with MPPMS and PMS on Ti-6Al-4V using 50Ti-50Al and 30Ti-70Al targets.

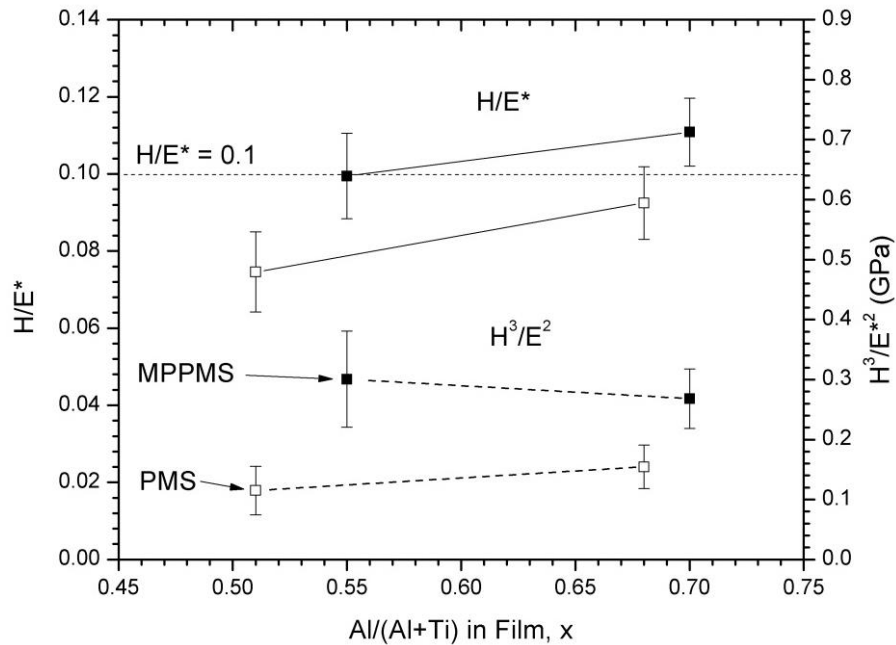


Figure 4.32 Hardness and effective modulus ratios of $Ti_{1-x}Al_xN$ coatings deposited with MPPMS and PMS onto Ti-6Al-4V using 50Ti-50Al and 30Ti-70Al targets.

4.3.3 Wear and Adhesion

Adhesion was evaluated with scratch tests and Rockwell C indent tests for coatings deposited with MPPMS and PMS, using the two target compositions, 50Ti-50Al and 30Ti-70Al. Scratch test results showing the effects of power supply, target composition, and substrate are tabulated in Table 4.3. Optical images of the scratch tests can be viewed in Figure 4.33 and Figure 4.34. MPPMS-deposited coatings showed much poorer adhesion compared to PMS coatings, with immediate chipping and spallation inside and outside the track. PMS-deposited coatings exhibited more cohesive failure by chevron and conformal cracking within the track. All of the critical loads were higher for PMS-deposited coatings using the 30Ti-70Al target compared to the 50Ti-50Al target. The only noticeable difference between MPPMS-deposited coatings with different target compositions was the slightly higher loads at which continuous spallation occurred for the 30Ti-70Al target sample.

Substrate effects on adhesion are seen in Figure 4.34 for MPPMS-deposited coatings using the 50Ti-50Al target. Massive delamination and low critical loads were observed for coatings deposited on SS304. On the other hand, the coating deposited on Ti-6Al-4V exhibited good adhesion with cohesion failure before continuous spallation occurred. IN718 appeared to be intermediate in adhesion strength. Note that these results are similar to those attained by TiN coatings deposited with floating bias through indent testing.

Images and HF grades for indent tests of several $Ti_{1-x}Al_xN$ coatings deposited with MPPMS and PMS at floating biases are shown in Figure 4.35. The MPPMS-deposited coatings exhibited relatively low adhesion compared to PMS with the $Ti_{0.55}Al_{0.45}N$ coating performing slightly worse than the $Ti_{0.30}Al_{0.70}N$ coating. The PMS coatings had the best adhesion with both compositions having an HF 1 grade. These results agree well with the scratch tests.

Wear rates and COF's for coatings deposited with both target compositions and power supplies are shown in Figure 4.36. Wear rate was approximately one order of magnitude higher in $Ti_{1-x}Al_xN$ coatings compared to TiN. COFs were also higher, ranging from 0.5 to 0.95, whereas TiN coatings demonstrated COF's around 0.35 to 0.5. MPPMS-deposited coatings had a lower COF for both target compositions. Substantial overlap in error for wear rate made it difficult to determine whether it changed substantially between power supplies and target compositions. The only improvement observed was for MPPMS-deposited coatings using the 50Ti-50Al target, which exhibited a ~25% reduction in average wear rate and ~45% reduction in COF.

Table 4.3 Critical loads for scratch tested $Ti_{1-x}Al_xN$ coatings deposited with MPPMS and PMS using different target compositions and floating bias.

Target-Power Supply	Critical Loads (N)			Substrate	Critical Loads (N)		
	L_{C1}	L_{C2}	L_{C3}		L_{C1}	L_{C2}	L_{C3}
50Ti-50Al-MPPMS	1.82	3.9	2.7	IN718	1.82	3.9	2.7
50Ti-50Al-PMS	2.8	9.8	14.5	Ti-6Al-4V	3.8	7.0	11.1
30Ti-70Al-PMS	4.7	10.3	14.8	SS304	0.3	1.5	0.6
30Ti-70Al-MPPMS	1.7	3.2	1.9				

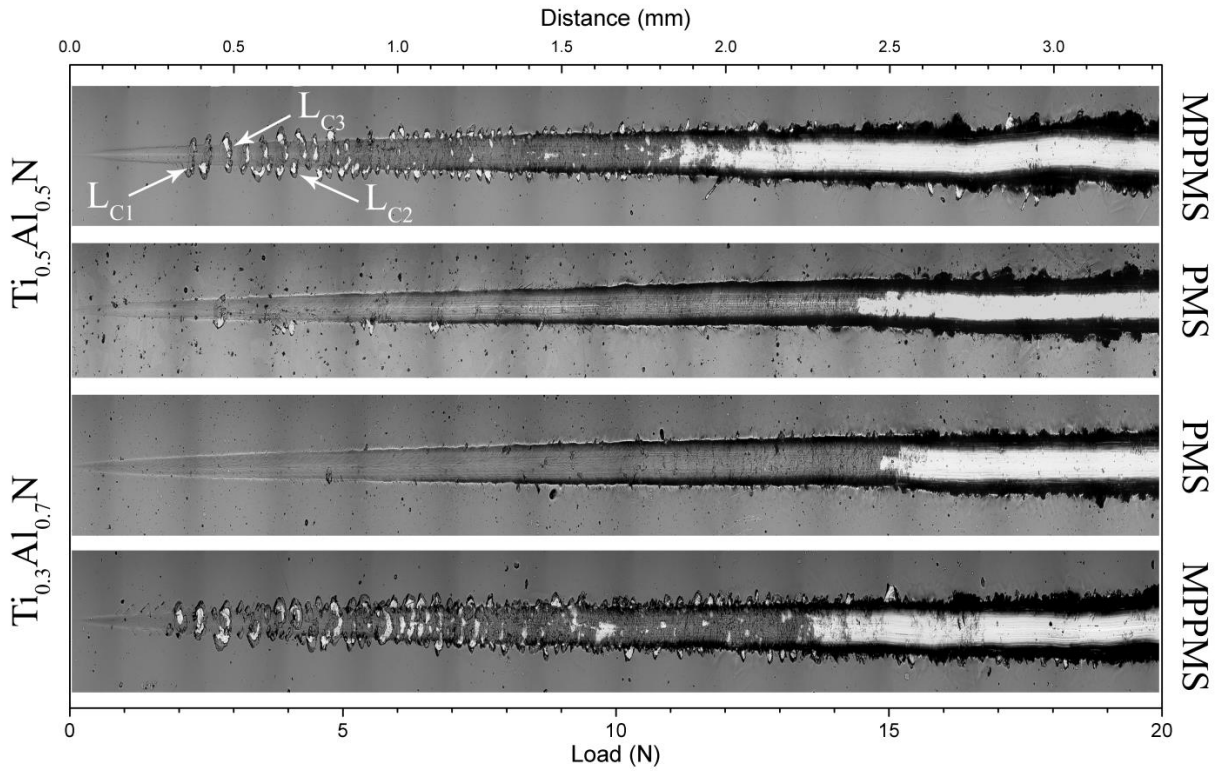


Figure 4.33 Scratch tests of MPPMS and PMS-deposited $Ti_{1-x}Al_xN$ coatings using two target compositions with floating bias.

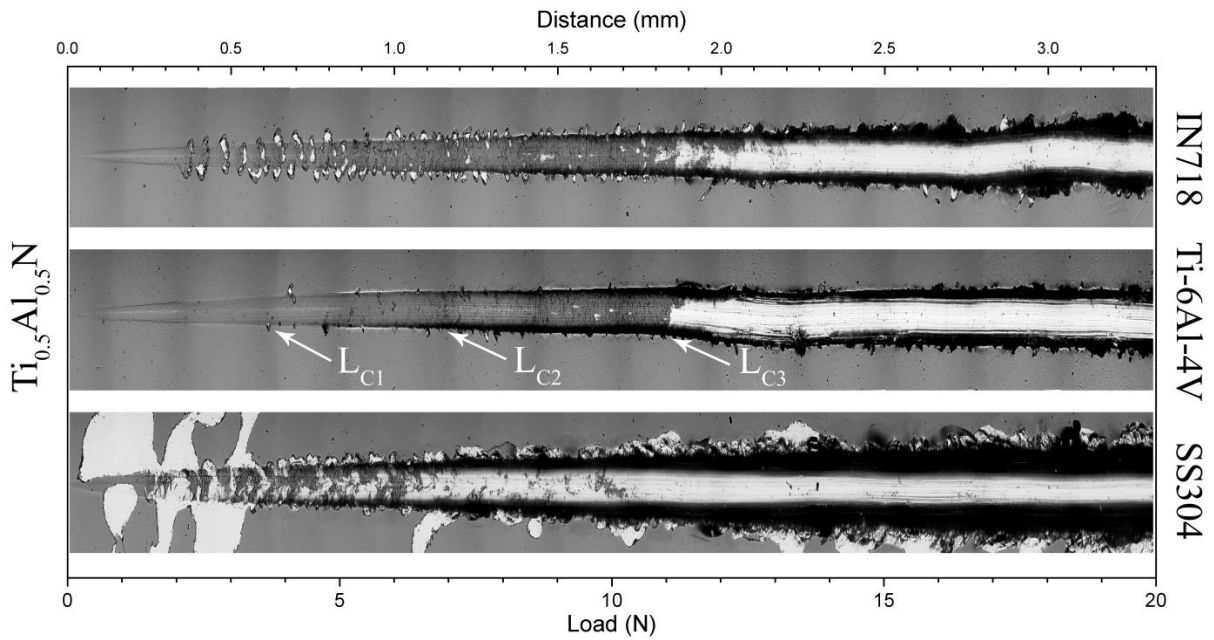


Figure 4.34 Scratch tests comparing substrate effects on MPPMS-deposited coatings using a 50Ti-50Al target with floating bias.

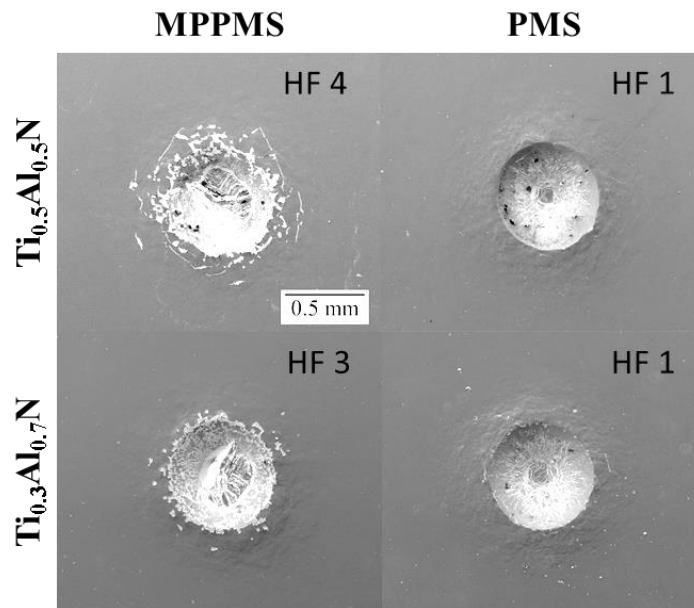


Figure 4.35 SEM images of Rockwell C indents performed on $Ti_{1-x}Al_xN$ coatings deposited on IN718. The deposition technique indicated on top and approximate coating composition indicated on the left. The HF grade is indicated in the corner of each image.

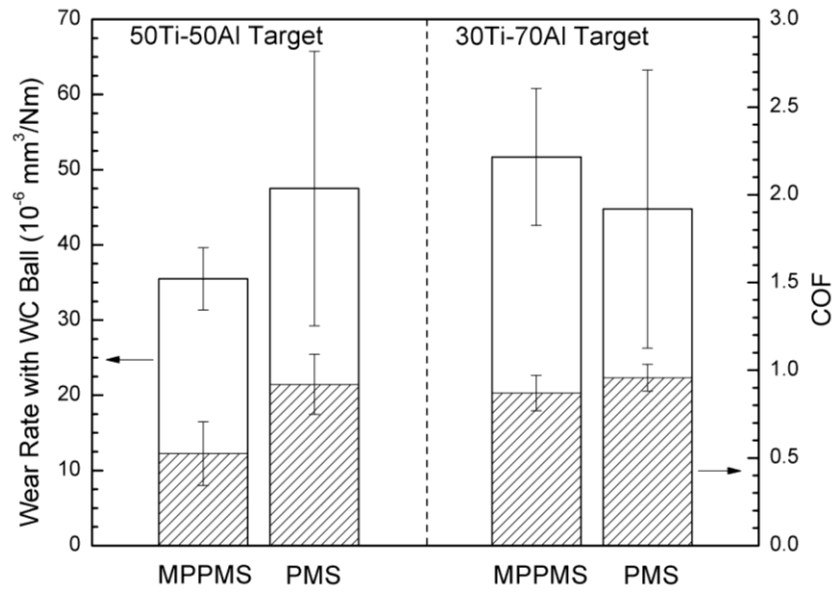


Figure 4.36 Wear rates and COF's for $Ti_{1-x}Al_xN$ coatings deposited with MPPMS and PMS using different target compositions.

CHAPTER 5: DISCUSSION

The results have shown that DOMS and MPPMS are capable of producing very dense coatings with desirable properties. In the following sections, the effects of deposition parameters like pulse pattern, substrate bias, working pressure, and film composition will be discussed. The results will be compared with the background and other literature to help explain the behavior and properties observed.

5.1 TiN

Substrate bias had a significant impact on microstructure, texture, adhesion, and wear. Microstructure analysis through SEM and TEM revealed gradual refinement in grain size with increasing substrate bias due to the nucleation of new grains through the thickness of the coating. It is likely that the additional energy supplied by substrate bias gave incident adatoms sufficient energy to form new grains with more favorable orientations and ample surface diffusion allowing for lateral grain growth, which is why grain width increased with increasing bias. The long fibrous grains and texture observed in coatings deposited with floating bias indicate limited surface diffusion. In this case, adatoms can diffuse on high diffusivity planes until they reach a grain of lower diffusivity where they are then confined. An *ab initio* density functional theory study investigating the absorption and binding energies of atoms and molecules on TiN planes calculated diffusion activation energies for Ti atoms of 0.35 eV and 1.74 eV for (001) and (111), respectively [73]. Therefore, (111) orientations are more likely to occur. Additionally, limited adatom mobility limits the amount of lateral grain growth that can occur. As a result, fibrous grains are formed and shadowing effects from neighboring grains, especially at initial stages of growth, can cause the formation of grain boundary voids. Such voids are associated with lower hardness and adhesion. Additional defects that may form and cannot be accommodated due to limited diffusion such as stacking faults, vacancies, and entrapped gases.

The theory in the previous paragraph explains why a (111) orientation may occur in coatings with a fibrous, Zone I structure. Increasing the adatom mobility through bias may enable atoms to rearrange and reduce defects or form other textures to reduce competing energies. Energies often considered are surface energy, strain energy, and channeling energy, though channeling energy is only significant for substrate biases greater than -100 V [35]. As explained in Section 2.3, the surface energy varies for certain preferred orientations following the relationship, $S_{200} < S_{220} < S_{111}$, and for elastic strain energy, $u_{111} < u_{220} < u_{200}$. Surface planes with a larger number of dangling bonds tend to have higher surface energies associated with them, (111) having the most. Elastic strain energy can be described by the simple relationship in Equation (5.1).

$$u_{[hkl]} = \frac{1}{2} E_{[hkl]} \varepsilon^2 \quad (5.1)$$

The term $E_{[hkl]}$ represents the elastic modulus for the $[hkl]$ direction and ε is strain parallel to $[hkl]$. Antonov conducted a density-functional study to calculate elastic moduli for low index directions in TiN and found that $E_{[111]} < E_{[220]} < E_{[200]}$ (see Table 5.1) [72]. In the case of an equibiaxial stress state, it would be expected that the highest values of u would be in the case where the highest number of stiff directions, $[200]$, lie parallel with the in-plane stresses. A diagram showing (100) , (110) , and (111) atomic planes of TiN oriented parallel to the substrate are shown in Figure 5.1. The highest number of $[200]$ directions that are parallel with the in-plane stresses occur when the (200) plane is oriented parallel to the plane-stresses, which coincides with the substrate surface. The (200) plane also has two (110) directions. The lowest number of $[200]$ directions occur when (111) planes are oriented parallel to the surface, in which case there are three $[220]$ directions. The (220) plane has only one $[200]$ direction, one $[110]$ direction, and two $[111]$ directions. By multiplying the number of directions with their respective average moduli from Antonov, then summing the products, we find that the highest total is for (200) , followed by (110) , then (111) . This explains why u_{hkl} follows the aforementioned order described by Cheng. McKenzie came to the same conclusion using a formula that can determine preferred orientations based on using stiffness constants for any cubic material [74]. Thus, at low residual stresses and high adatom mobilities, (200) texture is expected. The highest (200) intensity was observed for coatings deposited with floating and -30 V bias. An intermediate texture of (220) for -60 V bias was produced followed by a (111) texture using -90 V bias in which residual stresses were higher.

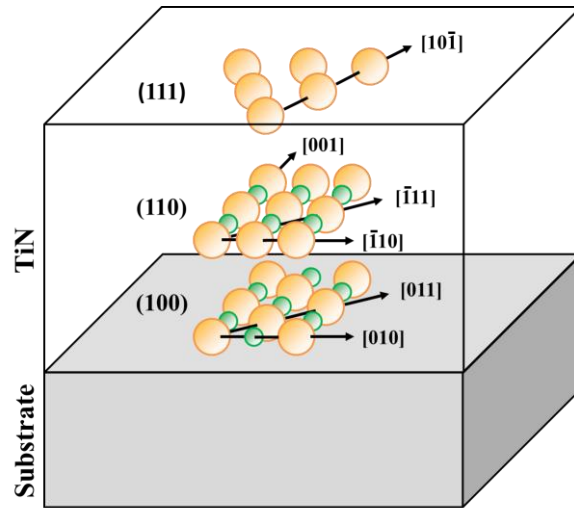


Figure 5.1 Diagram showing (100) , (110) , and (111) single atomic layers of TiN oriented parallel to the substrate surface with low index directions that lie within each plane labeled and indicated by arrows.

Table 5.1 Simulated elastic moduli for TiN thin films (GPa) [72].

Direction	GGA-PBE	LDA-PW	LDA-HGH	LDA-TM	Averaged
[100] thin film	307	484	301	385	369
[110] thin film	227	352	296	271	287
[111] thin film	231	256	236	236	240

Nanoindentation showed that hardness increased with increasing substrate bias, while modulus increased up to -60 V then decreased for -90 V. For both DOMS and PMS-deposited coatings, the hardness showed a strong correlation with GS calculations from XRD, signifying a Hall-Petch relationship where hardness increases with decreasing GS. Despite having a smaller average GS, DOMS-deposited coatings had a slightly lower hardness for -90 V bias. Compressive residual stress and film density may have also contributed to the difference in hardness. The change in modulus seems to correlate with the texture transition, (111)/(200)>(220)>(111), seen in DOMS-deposited coatings. The results also agree with the moduli trends for different crystal directions observed by Antonov [72], where $E_{[100]} > E_{[110]} > E_{[111]}$. However, it has also been found that porosity and grain size can also affect modulus in nanocrystalline materials [33]. It was shown that the -90 V bias sample had the highest H/E* ratio of 0.091. This value approaches 0.1, which is considered the value for which coatings with H/E*>0.1 have excellent adhesion and wear properties due to enhanced deflection of applied stresses [32].

Adhesion strength varied greatly between substrates and deposition conditions. One of the most influential factors was substrate bias. Scratch tests and Rockwell-C indent tests showed that samples deposited with substrate bias had significantly improved adhesion compared to floating bias samples. Furthermore, adhesion strength improved with increasing substrate bias voltage. The degree of adhesion is determined by the nature of atomic intermixing and stresses at the interface between the deposited coating and substrate. A Ti adhesion layer improves adhesion in two ways: titanium's oxygen gettering properties enable the dissolution of detrimental oxides on the substrate surface and the ductility of Ti helps create a buffer zone to accommodate stresses at the interface [28, 75]. By applying substrate bias, kinetic energy is supplied to ions that bombard the substrate surface. Some of that energy is converted to thermal energy, which was observed by noting the increasing substrate temperatures with increasing substrate bias. Thermal energy assists in adatom mobility which assists in diffusion, but may also help in reducing voids and defects produced during coating growth that can also impact adhesion. Additionally,

ion bombardment may produce lattice defects in the substrate, which may provide additional driving force for diffusion. Conversely, if the substrate bias is too great, then bombardment may create too many defects and can damage atomic bonds at the interface, which can degrade adhesion.

Deposition technique and substrate material were two additional factors that impacted coating adhesion. Both can impact residual stresses in the coatings, either from intrinsic stresses gained by growth defects or thermal stresses from CTE mismatch. Deposition technique may also affect the concentration of defects at the interface due to differences in incident ion energies, in addition to varying the amount of adatom mobility available for intermixing. For TiN coatings deposited with floating bias, MPPMS and PMS had better adhesion according to Rockwell C indentation test, although at higher substrate biases, the deposition technique was not as influential as the substrate material. For coatings deposited with floating bias, indent tests showed that coatings deposited on SS304 had the lowest adhesion strength, followed by IN718, then Ti-6Al-4V. SS304 was shown to have the most compressive calculated σ_{th} , followed by IN718, and Ti-6Al-4V with the lowest. One possible explanation is that the larger thermal residual stresses due to CTE mismatch for the SS304 substrate may have contributed to its higher adhesion strength. However, this behavior was not observed for higher substrate biases. Limited adatom mobility in floating biased coatings may have resulted in increased defects near the interface making those coatings more susceptible to adhesive failure. Increased contrast within grains observed in TEM for coatings deposited with floating bias may indicate a higher concentration of growth defects to support this. Additionally, there was no contrast near the interface like that seen for the -90 V biased samples that could have suggested strain within the Ti layer. If the contrast was strain contrast, then it may suggest that adhesion was insufficient for there to be any strain transfer from the substrate to the Ti layer for coatings deposited with floating bias. This would mean poor bonding between the Ti adhesion layer and the substrate making delamination more likely for coatings deposited with floating bias.

Scratch tests revealed that, for TiN coatings deposited with -90 V bias, adhesive failure occurred at lower loads for Ti-6Al-4V followed by IN718 and was not observed for SS304. One explanation is that the mechanical response of the substrates may affect the nature of the applied stresses the coating and interface are subjected to during the scratch and indent tests. Drory and Hutchinson showed that the effective area in which the indented material experienced strain depended on the ratio σ_{yield}/E and N of the substrate, where σ_{yield} , E , and N are the yield stress, elastic modulus, and work hardening exponent, respectfully [76]. With increasing σ_{yield}/E and N the area of combined elastic and plastic strain also increased. The relatively high σ_{yield}/E ratio for Ti-6Al-4V may be conducive of a larger distributed area of strain, thus reducing tensile stresses created by bending in the coating. This may explain the higher L_{C1} loads and less frequent cracking in indent tests for Ti-6Al-4V. However, the larger area may be conducive

of larger shear stresses at, or close to, the interface. This would explain the lower load at continuous spallation for Ti-6Al-4V observed in scratch tests. Meanwhile, the lower σ_{yield}/E for SS304 may create a very small affected strain area. This may induce a plowing effect where pile-up occurs ahead of the indenter. This would increase the amount of compressive stress normal to the surface and reduce the shear stresses responsible for spallation. Another factor may involve the substrate's native oxides and their reactivity with the Ti adhesion layer. The increased Cr content in SS304 oxides have been shown to improve adhesion when a Ti adhesion layer is used, suggesting that the type of native oxide present may have an effect on adhesion [28].

Wear rates in TiN coatings were strongly influenced by substrate bias. This was expected due to the fact that the H^3/E^2 values were shown to increase with increasing substrate bias up to -90 V. According to Musil [64] and others [77–80], wear rates should decrease with increasing H^3/E^2 . A plot of wear rate vs H^3/E^2 values showed a nearly linear decreasing trend. However, Guruvenket *et. al.* [79] tested coatings with a wider range of H^3/E^2 values and showed that the trend exhibits an exponential decay. Of course, wear rate can vary depending on other variables such as the material system, substrate hardness, coating thickness, and instrumental parameters. Nevertheless, H^3/E^2 has shown to be a useful predictor for wear behavior in TiN coatings.

5.2 $\text{Ti}_{1-x}\text{Al}_x\text{N}$

Composition is an important factor when it comes to the mechanical properties, thermal stability, and corrosion resistance of $\text{Ti}_{1-x}\text{Al}_x\text{N}$ coatings. The results have shown that both target composition and power supply have an effect on the coating composition. For $\text{Ti}_{1-x}\text{Al}_x\text{N}$ coatings deposited with a 50Ti-50Al target, x increased by 0.04 for MPPMS compared to PMS. For $\text{Ti}_{1-x}\text{Al}_x\text{N}$ coatings deposited with a 50Ti-50Al target, x increased by 0.02 for MPPMS compared to PMS. Preferred sputtering of Al for MPPMS-deposited $\text{Ti}_x\text{Al}_{1-x}\text{N}$ has previously been reported by Papa *et. al.*, who deposited $\text{Ti}_{1-x}\text{Al}_x\text{N}$ coatings with MPPMS using several target compositions (see Figure 5.2) [81]. For coatings deposited with targets that had ≤ 60 at.% Al, the Al/(Al+Ti) ratio in the coating was higher than that for the target. For coatings deposited with a $\text{Ti}_{0.33}\text{Al}_{0.67}$ target, the Al/(Al+Ti) ratio in the coating changed to being less than that for the target. Substrate bias voltage and current did not seem to have a significant effect on the coating composition. A recent review of HPPMS by Sarakinos discussed the effects of high ionization, generally observed by HPPMS techniques like MPPMS and DOMS, on the sputtering behavior of metal ion species [5]. High degrees of ionization increase the likelihood for metal ion species to be attracted back to the target surface, due to the large negative target voltage. Metal ions collide with atoms on the target surface producing newly sputtered metal ions. This phenomenon is known as “self-sputtering”. The sputter yield, Y, may vary according to the incident ion and atom to be sputtered. Using the same

software and ion energy used by Sarakinos [5], several sputter yields were calculated and are presented in Table 5.2. One of the main occurrences to note is the higher self-sputter yield for Al, while $Y_{Ti/Ti}$ is relatively close to $Y_{Ti/Ar}$ and $Y_{Ti/N}$. This could explain the higher concentration of Al in $Ti_{1-x}Al_xN$ coatings deposited with MPPMS compared with the PMS coatings. The higher $Y_{Al/N}$ compared to $Y_{Ti/N}$ may partially explain why Al composition is initially higher for both power supplies. However, at higher Al target compositions, the Al/(Al+Ti) ratio in the coatings falls below that of the target, contradicting the previously suggested theory. Several other factors can influence the coating/plasma composition, such as relative amounts of higher order ion species, different levels of ion re-attraction to the target, pulse parameters, and ion interactions between the target and substrate. The many plasma dynamics that occur in HPPMS techniques are still not fully understood, so it is difficult to make any clear explanations for this behavior.

Table 5.2 Calculated sputter yields using TRIM with 500 eV incident ions [82].

Calculated Sputtering Yields, $Y_{atom/ion}$ (sputtered atoms/incident ion)					
$Y_{Ti/Ar}$	$Y_{Al/Ar}$	$Y_{Ti/N}$	$Y_{Al/N}$	$Y_{Ti/Ti}$	$Y_{Al/Al}$
0.649	0.658	0.574	1.18	0.525	1.05

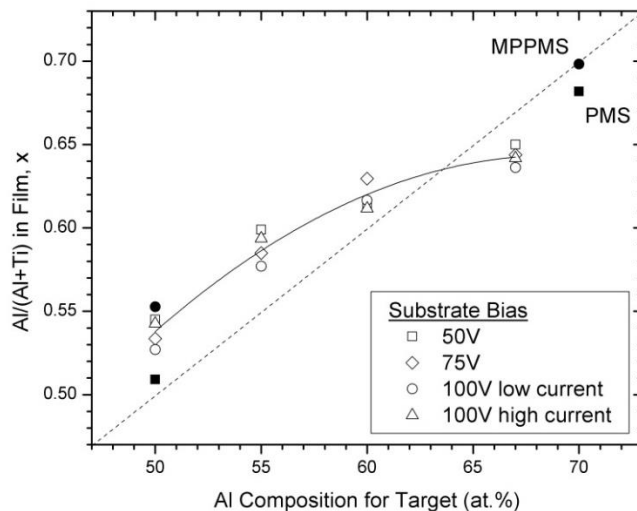


Figure 5.2 Al/(Al+Ti) ratios derived from electron probe micro-analysis (EPMA) measurements for $Ti_{1-x}Al_xN$ coatings deposited with several target compositions using MPPMS. Adapted from [81].

There was a substantial difference in hardness between MPPMS-deposited coatings and those deposited with PMS, especially when the 50Ti-50Al target was used. XRD revealed that, for coatings deposited with the 50Ti-50Al target, the structures appear to be cubic with slightly different textures. The

increased (200) texture for MPPMS may be the cause for an increase in modulus. SEM analysis revealed a refinement in grain structure for MPPMS-deposited coatings, which was supported by the XRD measurements. Similar gains in hardness for similar reductions in GS were found in PMS-deposited TiN coatings using floating and -90 V bias. It is important to note that without substrate bias, significant reduction in GS was accomplished only by using MPPMS. The observed correlations between hardness and GS have shown that the Hall-Petch relationship is likely one of the main contributors strengthening TiN and $Ti_{1-x}Al_xN$ coatings, although compressive residual stresses may have also contributed. Grain refinement has shown to be one of the main contributors by which DOMS and MPPMS help improve coating properties.

For coatings deposited with the 30Ti-70Al target, there was a slight increase in hardness for the MPPMS-deposited coatings. GS calculated from XRD showed that the difference between PMS and MPPMS was insignificant. While some grain refinement may have occurred, previous investigations of $Ti_{1-x}Al_xN$ mechanical properties [43–46, 50, 51, 83] suggest that the composition and the phases present are perhaps the most influential factors that determine hardness. The PMS-deposited coatings were primarily composed of the wurtzite phase, whereas the MPPMS samples contained a mixture of the cubic and wurtzite phases. Since the cubic phase has a higher hardness compared to wurtzite, which may explain why the MPPMS-deposited coating had a higher hardness. Another possibility is that compressive residual stress in the MPPMS-deposited sample may have contributed. XRD results show a significant shift to lower 2θ for the (10 $\bar{1}$ 0) and (0002) peaks which indicates an increase in d-spacing normal to the surface. Tensile strains resulting from compressive biaxial residual stresses are one likely explanation for this observation. Due to scattered results in $\sin^2\psi$ analysis, no conclusive residual stress measurements were made. Despite coatings deposited with the 30Ti-70Al target having lower hardness, the high Al content samples achieved highest H/E* values compared to coatings deposited with the 50Ti-50Al target and all the TiN coatings. Both MPPMS-deposited samples exhibited values of H/E*>0.1; classifying them as ultra-high performance coatings according to Musil et al. [64].

Although MPPMS-deposited samples seemed to have better hardness properties, adhesion appeared to be worse compared to PMS coatings. All three critical loads were lower for MPPMS-deposited coatings onto IN718, and the failures were mostly adhesive in nature. Early spallation and chipping outside the track revealing the underlying substrate were signs that the MPPMS coatings had poor adhesion. Indent tests showed that MPPMS coatings performed worse for both targets compared to PMS coatings, which agrees with scratch tests. High residual stresses may be one explanation; however, it is more likely due to the adhesion layer thickness. As seen in SEM and TEM results, the deposition rate was lower for both the $Ti_{1-x}Al_xN$ layer and the Ti adhesion layer in MPPMS-deposited coatings. The

result was a Ti adhesion layer no thicker than 50 nm, while PMS-deposited coatings had almost three times that thickness. The lower deposition rate is likely due to the low peak power density of the MPPMS pulse pattern equal to 0.068 kW/cm^2 , which is less than the average $0.1\text{-}0.5 \text{ kW/cm}^2$ typically used for MPPMS. High peak powers could not be attained without heavy arcing at the target surface. The thinner overall coating is less supportive of loads created by a scratch indenter and wear indenter. Additionally, the thinner adhesion layer may not be able to accommodate as much deformation at the interface caused by applied loads or thermal stresses. Comparing adhesion between the different substrates revealed even worse adhesion for SS304, with massive delamination inside and outside the track. Meanwhile, Ti-6Al-4V performed similarly to the PMS-deposited coatings on IN718. This order of poor to good adhesion between substrates was seen before in DOMS-deposited TiN coatings with floating bias. This would suggest that thermal stresses from CTE mismatch concentrated near the interface play an important role with regard to adhesion, especially for coatings deposited with floating bias.

Despite having higher H/E^* and H^3/E^2 values, all the $\text{Ti}_{1-x}\text{Al}_x\text{N}$ coatings had wear rates an entire magnitude higher than those of TiN coatings. Reasoning behind this result is not yet clear, however the result shows that wear rate is not purely dependent on hardness values. Many other variables may influence wear behavior such as crystal structure, reactivity between the coating and sliding material, generation of abrasive particles, sample thickness, humidity, temperature, and possibly other operating conditions.

CHAPTER 6: CONCLUSIONS

The development of “smart” coatings using the novel PVD techniques, DOMS and MPPMS, has been investigated in an effort to extend the application regime of commercial non-ferrous alloys. The structures and tribological properties of DOMS and MPPMS-deposited TiN and $Ti_{1-x}Al_xN$ coatings were investigated and compared with PMS and other techniques through literature. The following conclusions for this thesis work have been divided into two sections, TiN and $Ti_{1-x}Al_xN$.

6.1 TiN coatings

A comparison between PMS and DOMS-deposited coatings revealed that DOMS produced comparable hardness and wear properties to PMS coatings. Coatings deposited with PMS slightly outperformed DOMS in mechanical response, adhesion, and wear resistance. However, when grown to greater thicknesses ($>3 \mu m$), DOMS showed a 24% higher deposition rate. This indicates that DOMS is potentially advantageous for producing dense thick coatings without the added drawback of low deposition rates typically observed with HPPMS systems. Due to the flexibility in pulse parameters, it is also likely that DOMS can be optimized to eventually match or exceed the properties gained by PMS.

Substrate bias and working pressure were two variables targeted for optimizing DOMS-deposited TiN coatings. Substrate bias can have a strong effect on the incident ion energies, which translates to the adatom mobilities and often the generation or repair of growth defects. In addition to grain refinement produced by DOMS relative to PMS, substrate bias was shown to help refine grain structure by encouraging nucleation of new grains through the thickness of the coating. Optimum hardness and modulus properties were achieved with a -90 V substrate bias; although these results warrant more investigation of higher substrate bias voltages to further optimize the mechanical response. Working pressures of 3-9 mTorr showed to have little effect on hardness under the deposition conditions used, however it was found that sample location relative to the sputter track may result in different plasma conditions. This showed to have an effect on coating texture and deposition rate, thus careful consideration must be had when positioning substrates with respect to the target sputter track.

Adhesion was also improved by substrate bias, which has shown to improve adatom mobility which can encourage better intermixing and atomic bonding between the substrate. Large CTE mismatch between the substrate and coating decreased adhesion for coatings deposited with floating bias. This was also observed for $Ti_{1-x}Al_xN$ coatings. While evaluating adhesion, it was found that the mechanical properties of the substrate are important to consider. Depending on the mechanical interaction between the indenter and surface, coatings may show to have varying performance.

Nanoindentation and wear testing revealed a convincing trend between H^3/E^2 and wear rate as found by others [64, 77–80]. Critical loads in scratch tests also seemed to show a relationship to H^3/E^2 . As found later on in $Ti_{1-x}Al_xN$ coatings, wear rate did not follow the same trends as TiN. Thus, H^3/E^2 may be useful as a guide in predicting relative wear rates of coatings, but care should be given when trying to compare different coating material systems.

6.2 $Ti_{1-x}Al_xN$

MPPMS was found to substantially improve hardness and H^3/E^2 over PMS-deposited coatings, especially when deposited with a 50Ti-50Al target. Grain refinement, also seen in TiN coatings, was one of the main mechanisms proposed. For higher Al, compressive residual stress and the retaining of cubic $Ti_{1-x}Al_xN$ were used as possible explanations for improved hardness over PMS-deposited coatings.

Poor adhesion was attributed to the slow deposition rate and subsequently low thickness the Ti adhesion layer in MPPMS-deposited coatings. Limitations in target peak power created by heavy arcing forced the used of lower peak powers, which are often attributed to HPPMS's performance enhancing characteristics. DOMS may be a better alternative as it has shown improvements in arc suppression over MPPMS.

The used of MPPMS versus PMS showed to have an effect on the coating composition when using a composite target. This was attributed to preferential sputtering magnified by the self-sputtering mechanism unique to HPPMS methods. This is very important to consider in $Ti_{1-x}Al_xN$ coatings, where formation of wurtzite can degrade hardness properties.

REFERENCES

- [1] P. M. Martin, *Handbook of Deposition Technologies for Films and Coatings: Science, Applications and Technology*. Elsevier Science, 2009.
- [2] D. Rosello and E. Bergmann, "Corrosion protection with 'perfect' atomic layers," *Publié dans Oberflächen POLYSURFACES*, 2012. [Online]. Available: <http://www.polymedia.ch/OpArticles/view/57>. [Accessed: 23-Apr-2014].
- [3] B. N. Chapman, *Glow Discharge Processes: Sputtering and Plasma Etching*. Wiley, 1980, p. 406.
- [4] V. Kouznetsov, K. Macák, J. M. Schneider, U. Helmersson, and I. Petrov, "A novel pulsed magnetron sputter technique utilizing very high target power densities," *Surf. Coat. Technol.*, vol. 122, pp. 290–293.
- [5] K. Sarakinos, J. Alami, and S. Konstantinidis, "High power pulsed magnetron sputtering: A review on scientific and engineering state of the art," *Surf. Coatings Technol.*, vol. 204, no. 11, pp. 1661–1684, Feb. 2010.
- [6] G. Greczynski, J. Jensen, and L. Hultman, "CrN_x Films Prepared by DC Magnetron Sputtering and High-Power Pulsed Magnetron Sputtering: A Comparative Study," *IEEE Trans. PLASMA Sci.*, vol. 38, no. 11, pp. 3046–3056, 2010.
- [7] J. T. Gudmundsson, J. Alami, and U. Helmersson, "Spatial and temporal behavior of the plasma parameters in a pulsed magnetron discharge," *Surf. Coatings Technol.*, vol. 161, no. 2–3, pp. 249–256, Dec. 2002.
- [8] A. P. Ehiasarian and R. Bugyi, "Industrial Size High Power Impulse Magnetron Sputtering," in *Society of Vacuum Coaters 47th Annual Technical Conference Proceedings*, 2004, vol. 47th Annua.
- [9] J. T. Gudmundsson, "The high power impulse magnetron sputtering discharge as an ionized physical vapor deposition tool," *Vacuum*, vol. 84, no. 12, pp. 1360–1364, Jun. 2010.
- [10] A. Anders, "Discharge physics of high power impulse magnetron sputtering," *Surf. Coatings Technol.*, vol. 205, Suppl, no. 0, pp. S1–S9, Jul. 2011.
- [11] J. Bohlmark, M. Lattemann, J. T. Gudmundsson, A. P. Ehiasarian, Y. Aranda Gonzalvo, N. Brenning, and U. Helmersson, "The ion energy distributions and ion flux composition from a high power impulse magnetron sputtering discharge," *Thin Solid Films*, vol. 515, no. 4, pp. 1522–1526, Dec. 2006.
- [12] J. Lin, J. J. Moore, W. D. Sproul, B. Mishra, Z. Wu, and J. Wang, "The structure and properties of chromium nitride coatings deposited using dc, pulsed dc and modulated pulse power magnetron sputtering," *Surf. Coatings Technol.*, vol. 204, no. 14, pp. 2230–2239, Apr. 2010.
- [13] M. Hasheminasari, "Aluminium nitride piezoelectric thin films reactively deposited in closed field unbalanced magnetron sputtering for elevated temperature 'smart' tribological applications," Colorado School of Mines, 2013.

- [14] J. Lin, J. J. Moore, W. D. Sproul, B. Mishra, J. A. Rees, Z. Wu, R. Chistyakov, and B. Abraham, "Ion energy and mass distributions of the plasma during modulated pulse power magnetron sputtering," *Surf. Coat. Technol.*, vol. 203, pp. 3676–3685.
- [15] N. Bagcivan, K. Bobzin, and S. Theiß, "(Cr_{1-x}Al_x)N: A comparison of direct current, middle frequency pulsed and high power pulsed magnetron sputtering for injection molding components," *Thin Solid Films*, vol. 528, no. 0, pp. 180–186, Jan. 2013.
- [16] Y.-C. Hsiao, J.-W. Lee, Y.-C. Yang, and B.-S. Lou, "Effects of duty cycle and pulse frequency on the fabrication of AlCrN thin films deposited by high power impulse magnetron sputtering," *Thin Solid Films*, vol. 549, no. 0, pp. 281–291, Dec. 2013.
- [17] K. Ait Aissa, A. Achour, J. Camus, L. Le Brizoual, P.-Y. Jouan, and M.-A. Djouadi, "Comparison of the structural properties and residual stress of AlN films deposited by dc magnetron sputtering and high power impulse magnetron sputtering at different working pressures," *Thin Solid Films*, vol. 550, no. 0, pp. 264–267, Jan. 2014.
- [18] M. Huang, X. Zhang, P. Ke, and A. Wang, "Graphite-like carbon films by high power impulse magnetron sputtering," *Appl. Surf. Sci.*, vol. 283, no. 0, pp. 321–326, Oct. 2013.
- [19] M. Lattemann, U. Helmersson, and J. E. Greene, "Fully dense, non-faceted 111-textured high power impulse magnetron sputtering TiN films grown in the absence of substrate heating and bias," *Thin Solid Films*, vol. 518, no. 21, pp. 5978–5980, Aug. 2010.
- [20] F. Magnus, A. S. Ingason, O. B. Sveinsson, S. Olafsson, and J. T. Gudmundsson, "Morphology of TiN thin films grown on SiO₂ by reactive high power impulse magnetron sputtering," *Thin Solid Films*, vol. 520, no. 5, pp. 1621–1624, Dec. 2011.
- [21] J. Paulitsch, M. Schenkel, T. Zufraß, P. H. Mayrhofer, and W.-D. Münz, "Structure and properties of high power impulse magnetron sputtering and DC magnetron sputtering CrN and TiN films deposited in an industrial scale unit," *Thin Solid Films*, vol. 518, no. 19, pp. 5558–5564, Jul. 2010.
- [22] S. Shayestehaminzadeh, T. K. Tryggvason, L. Karlsson, S. Olafsson, and J. T. Gudmundsson, "The properties of TiN ultra-thin films grown on SiO₂ substrate by reactive high power impulse magnetron sputtering under various growth angles," *Thin Solid Films*, vol. 548, no. 0, pp. 354–357, Dec. 2013.
- [23] Q. Luo, S. Yang, and K. E. Cooke, "Hybrid HIPIMS and DC magnetron sputtering deposition of TiN coatings: Deposition rate, structure and tribological properties," *Surf. Coatings Technol.*, vol. 236, no. 0, pp. 13–21, Dec. 2013.
- [24] G. Greczynski, J. Lu, M. Johansson, J. Jensen, I. Petrov, J. E. Greene, and L. Hultman, "Selection of metal ion irradiation for controlling Ti_{1-x}Al_xN alloy growth via hybrid HIPIMS/magnetron co-sputtering," *Vacuum*, vol. 86, no. 8, pp. 1036–1040, Feb. 2012.
- [25] J. Alami, Z. Maric, H. Busch, F. Klein, U. Grabowy, and M. Kopnarski, "Enhanced ionization sputtering: A concept for superior industrial coatings," *Surf. Coatings Technol.*, no. 0.

- [26] J. Lin, W. Sproul, D. Moore, J. Wu, J. Lee, Z. Chistyakov, S. Abraham, R. Abraham, and B. Abraham, "Recent advances in modulated pulsed power magnetron sputtering for surface engineering," *J. Miner. Met. Mater. Soc.*, vol. 63, pp. 48–58.
- [27] J. L. and B. W. and W. D. S. and Y. O. and I. Dahan, "Anatase and rutile TiO₂ films deposited by arc-free deep oscillation magnetron sputtering," *J. Phys. D. Appl. Phys.*, vol. 46, no. 8, p. 84008, 2013.
- [28] U. Helmersson, B. O. Johansson, J. Sundgren, x, E, H. T. G. Hentzell, and P. Billgren, "Adhesion of titanium nitride coatings on high-speed steels," *J. Vac. Sci. Technol. A Vacuum, Surfaces, Film.*, vol. 3, pp. 308–315, 1985.
- [29] F. Cverna and A. S. M. I. M. P. D. Committee, Eds., *ASM ready reference. Thermal properties of metals*. Materials Park, Ohio: Materials Park, Ohio : ASM International, 2002.
- [30] B. A. Movchan and A. V Demchishin, "Study of the structure and properties of thick vacuum condensates of nickel, titanium, tungsten, aluminium oxide and zirconium dioxide," *Phys. Met. Metall.*, vol. 28, pp. 83–90, 1969.
- [31] J. A. Thornton, "Influence of apparatus geometry and deposition conditions on the structure and topography of thick sputtered coatings," *J. Vac. Sci. Technol.*, vol. 11, pp. 666–670, 1974.
- [32] P. J. Kelly and R. D. Arnell, "Development of a novel structure zone model relating to the closed-field unbalanced magnetron sputtering system," *J. Vac. Sci. Technol. A Vacuum, Surfaces, Film.*, vol. 16, pp. 2858–2869, 1998.
- [33] S. Mahieu, P. Ghekiere, G. De Winter, R. De Gryse, D. Depla, G. Van Tendeloo, and O. I. Lebedev, "Biaxially aligned titanium nitride thin films deposited by reactive unbalanced magnetron sputtering," *Surf. Coatings Technol.*, vol. 200, pp. 2764–2768, 2006.
- [34] W. Yongqiang, C. Xiaoxia, T. Xiubo, G. Chunzhi, Y. Shiqin, J. Zhiqiang, and C. Liangji, "Effects of pulsed bias duty ratio on microstructure and surface properties of TiN films," *Vacuum*, vol. 89, pp. 185–189, 2013.
- [35] Y. H. Cheng and B. K. Tay, "Development of texture in TiN films deposited by filtered cathodic vacuum arc," *J. Cryst. Growth*, vol. 252, pp. 257–264, 2003.
- [36] J. P. Zhao, X. Wang, T. S. Shi, and X. H. Liu, "Evolution of the texture of TiN films prepared by filtered arc deposition," *J. Appl. Phys.*, vol. 79, no. 12, p. 9399, Jun. 1996.
- [37] H. O. Pierson, *Handbook of refractory carbides and nitrides: Properties, characteristics, processing and applications*. Noyes Publication, New York, NY (United States), 1997.
- [38] Y. Y. Guu and J. F. Lin, "The tribological characteristics of titanium nitride coatings. Part II. Comparisons of two deposition processes," *Wear*, vol. 194, pp. 22–29.
- [39] L. C. Hernández, L. Ponce, A. Fundora, E. López, and E. Pérez, "Nanohardness and Residual Stress in TiN Coatings," *Materials (Basel)*, vol. 4, pp. 929–940, 2011.

- [40] D. Bhaduri, A. Ghosh, S. Gangopadhyay, and S. Paul, "Effect of target frequency, bias voltage and bias frequency on microstructure and mechanical properties of pulsed DC CFUBM sputtered TiN coating," *Surf. Coatings Technol.*, vol. 204, pp. 3684–3697, 2010.
- [41] P. J. Kelly, T. vom Braucke, Z. Liu, R. D. Arnell, and E. D. Doyle, "Pulsed DC titanium nitride coatings for improved tribological performance and tool life," *Surf. Coatings Technol.*, vol. 202, pp. 774–780, 2007.
- [42] T.-S. Yeh, J.-M. Wu, and L.-J. Hu, "The properties of TiN thin films deposited by pulsed direct current magnetron sputtering," *Thin Solid Films*, vol. 516, pp. 7294–7298, 2008.
- [43] C.-C. Lai, "Growth and Phase Stability of Titanium Aluminum Nitride Deposited by High Power Impulse Magnetron Sputtering," Linköping University Institute of Technology, 2011.
- [44] I. A. Abrikosov, A. Knutsson, B. Alling, F. Tasnádi, H. Lind, L. Hultman, and M. Odén, "Phase Stability and Elasticity of TiAlN," *Materials (Basel)*, vol. 4, no. 9, pp. 1599–1618, 2011.
- [45] A. Knutsson, M. P. Johansson, L. Karlsson, and M. Odén, "Thermally enhanced mechanical properties of arc evaporated Ti_{0.34}Al_{0.66}N/TiN multilayer coatings," *J. Appl. Phys.*, vol. 108, no. 4, p. 044312, Aug. 2010.
- [46] A. Hörling, L. Hultman, M. Odén, J. Sjöln, and L. Karlsson, "Thermal stability of arc evaporated high aluminum-content Ti_{1-x}Al_xN thin films," *J. Vac. Sci. Technol. A Vacuum, Surfaces, Film.*, vol. 20, no. 5, p. 1815, Sep. 2002.
- [47] S. PalDey and S. C. Deevi, "Single layer and multilayer wear resistant coatings of (Ti,Al)N: a review," *Mater. Sci. Eng. A*, vol. 342, no. 1–2, pp. 58–79, Feb. 2003.
- [48] V. Podgursky, B. Torp, and R. Traksmá, "Investigation of (Ti, Al) N Based Coatings Grown by Physical Vapor Deposition," *Mater. ...*, 2005.
- [49] A. C. Vlasveld, S. G. Harris, E. D. Doyle, D. B. Lewis, and W. D. Munz, "Characterisation and performance of partially filtered arc TiAlN coatings," *Surf. Coatings Technol.*, vol. 149, no. 2–3, pp. 217–223, Jan. 2002.
- [50] W.-D. Münz, "Titanium aluminum nitride films: A new alternative to TiN coatings," *J. Vac. Sci. Technol. A Vacuum, Surfaces, Film.*, vol. 4, no. 6, p. 2717, Nov. 1986.
- [51] P. W. Shum, W. C. Tam, K. Y. Li, Z. F. Zhou, and Y. G. Shen, "Mechanical and tribological properties of titanium–aluminium–nitride films deposited by reactive close-field unbalanced magnetron sputtering," *Wear*, vol. 257, no. 9–10, pp. 1030–1040, Nov. 2004.
- [52] H. C. Barshilia, K. Yogesh, and K. S. Rajam, "Deposition of TiAlN coatings using reactive bipolar-pulsed direct current unbalanced magnetron sputtering," *Vacuum*, vol. 83, no. 2, pp. 427–434, Sep. 2008.
- [53] A. S. M. A. S. M. Inc., "Titanium Ti-6Al-4V (Grade 5), STA," vol. 2012. Matweb, LLC.

- [54] T. Scharf, "Metals," in *Handbook of Lubrication and Tribology, Volume II*, CRC Press, 2012, pp. 1–18.
- [55] A. S. M. A. S. M. Inc., "Special Metals INCONEL® Alloy 718," vol. 2012. Matweb, LLC.
- [56] F. C. Campbell, *Elements of Metallurgy and Engineering Alloys*. Materials Park, OH: ASM International.
- [57] A. Houghton, R. Lewis, U. Olofsson, and J. Sundh, "Characterising and reducing seizure wear of inconel and incoloy superalloys in a sliding contact," *Wear*, vol. 271, no. 9–10. pp. 1671–1680, 2011.
- [58] Z. Li, S. Qian, and W. Wang, "Influence of superalloy substrate roughness on adhesion and oxidation behavior of magnetron-sputtered NiCoCrAlY coatings," *Appl. Surf. Sci.*, vol. 257, no. 24, pp. 10414–10420, 2011.
- [59] S.-C. Lee, W.-Y. Ho, and F. D. Lai, "Effect of substrate surface roughness on the characteristics of CrN hard film," *Mater. Chem. Phys.*, vol. 43, no. 3, pp. 266–273, 1996.
- [60] J. Li, W. . Zheng, Z. Jin, X. Lu, G. Gu, X. Mei, and C. Dong, "Influence of substrate dc bias on chemical bonding, adhesion and roughness of carbon nitride films," *Appl. Surf. Sci.*, vol. 191, no. 1–4, pp. 273–279, May 2002.
- [61] K. Vasu, M. Kiran, M. Krishna, and K. Padmanabhan, "Effect of substrate on the crystallographic texture and microstructure evolution in Titanium Nitride (TiN) thin films," 2008.
- [62] K. L. Johnson and K. L. Johnson, *Contact Mechanics*. Cambridge University Press, 1987, p. 452.
- [63] D. Tabor, *The Hardness of Metals*. ClarendonP, 1951, p. 175.
- [64] J. Musil, F. Kunc, H. Zeman, and H. Poláková, "Relationships between hardness, Young's modulus and elastic recovery in hard nanocomposite coatings," *Surf. Coatings Technol.*, vol. 154, pp. 304–313, 2002.
- [65] "Test Method for Adhesion Strength and Mechanical Failure Modes of Ceramic Coatings by Quantitative Single Point Scratch Testing." ASTM International, 2005.
- [66] W. Heinke, A. Leyland, A. Matthews, G. Berg, C. Friedrich, and E. Broszeit, "Evaluation of PVD nitride coatings, using impact, scratch and Rockwell C adhesion tests," *Thin Solid Films*, vol. 270, pp. 431–438.
- [67] A. J. Perry, J. A. Sue, and P. J. Martin, "Practical measurement of the residual stress in coatings," *Surf. Coatings Technol.*, vol. 81, no. 1, pp. 17–28, May 1996.
- [68] I. U. of Crystallography, *International Tables for X-ray Crystallography: Physical and chemical tables*. Kynoch Press, 1972.
- [69] M. A. Z. Vasconcellos, S. C. Lima, and R. Hinrichs, "Hardness evaluation, stoichiometry and grain size of titanium nitride obtained with plasma nitriding on Ti-6Al-4V samples." 2010.

- [70] R. Machunze, A. P. Ehasarian, F. D. Tichelaar, and G. C. A. M. Janssen, "Stress and texture in HIPIMS TiN thin films," *Thin Solid Films*, vol. 518, no. 5, pp. 1561–1565, Dec. 2009.
- [71] J. A. Sue, "X-ray elastic constants and residual stress of textured titanium nitride coating," *Surf. Coatings Technol.*, vol. 54–55, pp. 154–159, Nov. 1992.
- [72] A. V. and I. I., "Density-functional study of the elastic properties of titanium nitride layers," *J. Optoelectronics Adv. Mater.*, vol. 11, pp. 1475–1478, 2009.
- [73] D. Gall, S. Kodambaka, M. A. Wall, I. Petrov, and J. E. Greene, "Pathways of atomistic processes on TiN(001) and (111) surfaces during film growth: an ab initio study," *J. Appl. Phys.*, vol. 93, no. 11, p. 9086, 2003.
- [74] D. R. McKenzie, Y. Yin, W. D. McFall, and N. H. Hoang, "The orientation dependence of elastic strain energy in cubic crystals and its application to the preferred orientation in titanium nitride thin films," *J. Phys. Condens. Matter*, vol. 8, no. 32, pp. 5883–5890, Aug. 1996.
- [75] S. J. Bull, P. R. Chalker, C. F. Ayres, and D. S. Rickerby, "The influence of titanium interlayers on the adhesion of titanium nitride coatings obtained by plasma-assisted chemical vapour deposition," *Mater. Sci. Eng. A*, vol. 139, pp. 71–78, Jul. 1991.
- [76] M. D. Drory and J. W. Hutchinson, "Measurement of the adhesion of a brittle film on a ductile substrate by indentation," in *Proceedings of the Royal Society of London Series A-Mathematical Physical and Engineering Sciences*, 1996, pp. 2319–2341.
- [77] A. Leyland and A. Matthews, "On the significance of the H/E ratio in wear control: a nanocomposite coating approach to optimised tribological behaviour," *Wear*, vol. 246, no. 1–2, pp. 1–11, Nov. 2000.
- [78] T. Y. Tsui, G. M. Pharr, W. C. Oliver, C. S. Bhatia, R. L. White, S. Anders, A. Anders, and I. G. Brown, "Nanoindentation and Nanoscratching of Hard Carbon Coatings for Magnetic Disks," *MRS Proc.*, vol. 383, p. 447, Feb. 2011.
- [79] S. Guruvenket, D. Li, J. E. Klemberg-Sapieha, L. Martinu, and J. Szpunar, "Mechanical and tribological properties of duplex treated TiN, nc-TiN/a-SiN_x and nc-TiCN/a-SiCN coatings deposited on 410 low alloy stainless steel," *Surf. Coatings Technol.*, vol. 203, no. 19, pp. 2905–2911, Jun. 2009.
- [80] S. Hassani, M. Bielawski, W. Beres, L. Martinu, M. Balazinski, and J. E. Klemberg-Sapieha, "Predictive tools for the design of erosion resistant coatings," *Surf. Coatings Technol.*, vol. 203, no. 3–4, pp. 204–210, Nov. 2008.
- [81] F. Papa, T. Sasaki, T. Ishikawa, A. Campiche, R. Tietema, and T. Krug, "Material properties of Aluminum Metal (Titanium/Chromium) Nitride coatings deposited by High Power Impulse Magnetron Sputtering (HIPIMS) technology," in *International Conference on Metallurgical Coatings and Thin Films*, 2012.
- [82] J. F. Ziegler, "SRIM & TRIM." 2013.

- [83] A. Flink, J. M. Andersson, B. Alling, R. Daniel, J. Sjöln, L. Karlsson, and L. Hultman, "Structure and thermal stability of arc evaporated $(\text{Ti}_{0.33}\text{Al}_{0.67})_{1-x}\text{Si}_x\text{N}$ thin films," *Thin Solid Films*, vol. 517, no. 2, pp. 714–721, 2008.